Compressive magnetohydrodynamic waves

in the solar atmosphere

by

Ding Yuan

Thesis

Submitted to the University of Warwick

for the degree of

Doctor of Philosophy

Department of Physics

March 2013

THE UNIVERSITY OF

WARWICK

Contents

List of Figures

vii

List of Tables

Acknowledgments

I would like to acknowledge Prof. Valery Nakariakov for his support and supervision during my PhD course, and also thank him for the fund support of several visits to the main collaborators in China and Russia.

I thank the useful discussions and advices from Dr. Erwin Verwichte and Dr. Claire Foullon.

I would like to express thanks to my main collaborators: Dr. R. Sych (Irkutsk, Russia), Dr. V. E. Reznikova (Leuven, Belgium), Dr. Yuandeng Shen (Yunnan, China), and Dr. Baolin Tan (Beijing, China).

I acknowledge the hosts to my visits to the Solar Radio Research Group, NAOC (Dr. Baolin Tan and Dr. Yihua Yan), to the Huairou Solar Observatory, NAOC (Dr. Jiangtao Su, Dr. Hongqi Zhang and Dr. Yuanyong Deng), to the Institute of Solar-Terrestrial Physics, Russian Academy of Sciences (Dr. R. Sych and Dr. S. A. Anfinogentov), to the Department of Astronomy, University of Nanjing (Prof. Pengfei Chen) and to the Yunnan Astronomical Observatory (Dr. Yuandeng Shen and Dr. Yu Liu).

This thesis was typeset by the author using the LaTeX[1] typesetting system originally developed by Leslie Lamport, based on TeX created by Donald Knuth.

---

[1] LaTeX 2_ε is the current version and an extension of LaTeX. LaTeX is a collection of macros of TeX. TeX is a trademark of the American Mathematical Society.

Declarations

This thesis is submitted to the University of Warwick in support of my application for the degree of Doctor of Philosophy. It has been composed by myself and has not been submitted in any previous application for any degree or other university.

The work presented (including data generated and data analysis) was carried out by the author except in the cases outlined below: Fig. 3.14 and the magnetic field extrapolation data in Sec. 3.3.2 were provided by Dr. V. E. Reznikova. Fig. 5.1 was made by Dr. Yuandeng Shen. The NRH radio data in Chapter 5 was prepared by Dr. Baolin Tan and Dr. Jing Huang. The NoRH radio data in Chapter 6 was sythesized by Dr. N. Chorley.

The work presented in this thesis are based on the following peer-reviewed journal articles, two published and three submitted:

- Ding Yuan, V. M. Nakariakov, N. Chorley and C. Foullon, Leakage of long period oscillation from the chromosphere to the corona, Astron. Astro. 553 (2011) A116.

- Ding Yuan, V. M. Nakariakov, Measuring the apparent phase speed of propagating EUV disturbances, Astron. Astro. 543 (2012) A9

- Ding Yuan, R. Sych, V. E. Reznikova, V. M. Nakariakov, Field line reconstruction with magneto-acoustic cut-off frequency above sunspots, Astron. Astro. 2012 (submitted)

- Ding Yuan, V. M. Nakariakov, R. Sych, Detection of high-azimuthal body modes in sunspot atmosphere, Astron. Astro. Letter 2013 (submitted)

- Ding Yuan, Yuandeng Shen, Yu Liu, V.M. Nakariakov, Baolin Tan, Jing Huang, Distinct propagating fast wave trains associated with flaring energy releases, Astron. Astro. Letter 2013 (submitted)

Abstract

For last decades, magnetohydrodynamic (MHD) waves arise to a hot topic of solar physics. With modern instruments, MHD wave modes are reliably detected, not only for their potential to heat the solar corona, but also as a new tool to diagnose the plasma parameters remotely (MHD seismology).

In this thesis, we use space-borne EUV/UV imagers and ground-based observatories to study compressive MHD waves in coronal loops and sunspots. We identify several instrumental artifacts and formulate the scheme to estimate the imager data noise. The diagnostic potential of MHD waves in various plasma structures are also investigated.

The orbit-related long periodicities (30-96 min) in the TRACE images and the derotation-induced short periodicy (3-9 min) in the SDO/AIA images are studied and quantified. The methods are proposed to mitigate the effects of such artificial periodicities. The noise level of AIA images is formulated.

In sunspots, the 5–min oscillation power usually forms a ring structure enclosing the sunspot umbra. The phase variation was found to display high-order MHD azimuthal body modes. The mode numbers were measured and justified by significance tests.

A multi-level observation of magnetoacoustic waves in sunspot was performed. The variation of the magnetoacoustic cut-off frequency over sunspot cross-sectional geometry and sunspot atmosphere was quantified and exploited to diagnose the inclination angle of the magnetic field.

To automatically measure the propagating speed of compressive MHD waves, we designed cross-fitting technique (CFT), 2D coupled fitting (DCF) and best similarity measure (BSM). Parametric studies were performed to confirm the validity and robustness of these methods.

Distinct propagating fast wave trains were found to be associated with radio bursts that were generated by the flare-accelerated non-thermal electrons. The stretching wavelength along the waveguide implies that the wave trains were impulsively triggered. The wave parameters are measured to probe the properties of guided fast waves.

The connectivity between different levels of sunspots and the associated active regions were studied. The long period oscillations were found in both the chromosphere and the corona. The periodicity was close to typical solar interior g-modes.

Chapter 1

Introduction

1.1 Solar observation

1.1.1 Solar structure

The Sun is a typical dwarf star formed about 4.57 billion years ago. It is about halfway through its main-sequence state, according to astronomical classification. It has a diameter of approximately $1,392,584\,\mathrm{km}$ and a mass of approximately 2×10^{30} kilograms. No physical surface is well-defined on the Sun, rather than a conventionally-identifiable border in visible light. The magnetic field and the released particles permeate the whole solar system, therefore the solar activities and dynamics affect the heliosphere and the planets. The Sun's structure, by convention, is divided into four domains: the solar interior, the solar atmosphere, the inner corona and the outer corona (cf. Fig. 1.1).

The solar interior is divided into distinct layers according to the recurring physical processes (cf. Fig. 1.1). The core is subject to tremendous gravitational contraction. The hydrogen nuclei become extremely dense and energetic, thus the kinetic energy is sufficient to overcome the electromagnetic repulsion. Therefore nuclear fusion is maintained constantly in the core. The plasma is heated up to around $16\,\mathrm{MK}$. Outside the dynamic core that is the energy and particle source, a thick radiative zone is formed to transport the energy radially outwards by radiative diffusion. The gamma rays, X-ray, neutrons and protons are radiated and scattered throughout this zone. It takes an average time of about 171,000 years for a gamma ray to escape from the radiative zone. The temperature of the radiative zone decreases steadily with the increasing radius and drops to about $1.5\,\mathrm{MK}$ at the boundary of the convective zone. In the convective zone, the energy transportation is dominated by convection: bulk motions of the plasma form circular convection

1

currents and transfer the energy from the interior upwards. The convective zone occupies the outer part of the solar interior above about 0.7 solar radii. It is followed by the base of the photosphere. Further up, it is the solar atmosphere.

The solar atmosphere comprises the photosphere, the chromosphere and the corona. The photosphere is the Sun's visible surface. It is a layer of gas with a thickness of about a few hundreds of kilometres. The solar material transits from opaque (to the optical emission) in the interior to transparent in the upper atmosphere. The photosphere has a temperature ranging from 4500 to 6000 K, and a density of about 2×10^{-4} kg/m^3. The Sun's photosphere is networked by several millions of granules that are caused by the bulk plasma convection (cf. Fig. 1.2). The typical size of a granule is at the order of 10^3 km. Its lifetime is about 8-20 minutes. The photosphere is a host of sunspots (cf. Sec. 1.1.3 and Fig. 1.2). The sunspots are strong magnetic concentrations, and are relatively cool because the magnetic field suppresses the convection motion.

The chromosphere is the second layer of the solar atmosphere. It is siting above the photosphere and below the transition region, with a thickness of about $2,000$ km. The density of the chromosphere is only 10^{-4} times that of the photosphere. The temperature of the chromosphere rises from about $4,400$ K to about $25,000$ K. The physics of chromospheric heating is still not well understood. Cool plasmas at the chromospheric temperature are also seen well above the chromospheric heights, e.g. in filaments (prominences). Above the chromosphere, the plasma temperature grows rapidly with height. It is penetrated by spicules, short-living jets of cool gas. They are ejected from the photosphere, rise to the top of the chromosphere and even above, and then occasionally sink back over the course of about 10 minutes.

The transition region lies in-between the chromosphere and the corona. This thin and irregular layer is not well-defined at the current stage, but it exhibits a wealth of physical processes. Within the transition region, the temperature rises rapidly from about 10^4 K to 10^6 K. Below this layer, it is a cool and dense region, partly ionised, dominated by the absorption lines (e.g. C IV, O IV and Si IV). Above it, the plasma becomes very hot, fully ionised, structured by the magnetic field and is optically thin. The plasma emission in this region is mainly from emission lines in the UV/EUV bandpasses.

The outer layer of the solar atmosphere is the corona. The coronal density drops to 10^{-12} times that of the photosphere, and the plasma gets heated up to $1,000,000$ K and higher. It is the host region of the main objects of our study, and its detailed description is given in Sec. 1.1.2.

1.1.2   Solar corona

The corona is the upper part of the Sun's atmosphere. According to the light sources, it is categorised into three types: K-corona, F-corona and E-corona. The K-corona (*kontinuierlich*, 'continuous' in German) is the component featured by continuous spectra from the scattered light of free electrons and the Doppler broadening of the reflected absorption lines from the photosphere. The F-corona is the part that mainly emits Fraunhofer scattering rays from the dust particles. The E-corona is characterised by the presence of emission lines. The corona has a typical particle density of $10^{15-16}\,\mathrm{m}^{-3}$ and an average temperature of 1-2 MK. Within the current knowledge, no single theory is capable of explaining the coronal heating dilemma. The main mechanisms considered for coronal heating are magnetic reconnection, MHD wave dissipation and high energy particles.

The structure of the solar corona changes significantly with the solar cycle. Near the solar minima, the coronal material is mostly confined to the equatorial regions, the coronal holes cover the polar regions. Close to solar maxima, the corona spreads over both the equatorial and polar regions. The corona exhibits a number of phenomena, e.g. active regions, coronal loops, solar plumes, prominences.

Active Region

Active regions are ensembles of plasma loop structures connecting the opposite magnetic polarities in the photosphere, where strong magnetic unipoles usually cluster in form of sunspot groups or other magnetic elements. The emissions from the active regions in X-rays are mainly caused by solar flares. The active regions are also the source of coronal mass ejections. Individual active regions are allocated numbers in the form of AR+ four digits, by the National Oceanic and Atmospheric Administration (NOAA), USA.

Coronal Loop

Coronal loops are spectacular structures of the lower corona and transition region of the Sun. They mainly emerge from the chromosphere and end up with foot points at opposite magnetic polarities. Coronal loops are closed magnetic flux tubes filled with dense plasma. The plasma β in coronal loops usually has a very small value, around 0.1 or less, while it may approach 0.5 in hot dense flaring loops. These plasma structures are known to be the hosts of wave and oscillatory phenomena.

Polar Plume

Polar plumes are cool, dense open magnetic structures that extend to up to 10 solar radii. They arise predominantly from the unipolar magnetic footpoints in coronal holes. They are usually observable in EUV and visible light bandpasses. This kind of structure is very quiescent and remain steady for days. There are hot, high-speed streams of plasma erupting from the plumes. These stable plumes are very simple in geometry and magnetic morphology, they are ideal test grounds for MHD wave studies (see review by, e.g., Nakariakov 2006).

Prominence

Prominences are cool dense plasma structures observed off the solar limb, suspended over the solar surface. The temperatures of prominences are much lower than the surrounding corona. Prominences extend outwardly in the ambient corona over large spatial scales. Their typical lifetime is of the order of several days or even months. Some prominences break apart and induce coronal mass ejections. Prominences observed on the solar disk are called solar filaments.

1.1.3 Solar activity

In the solar corona, the particle density drops dramatically to a very low level ($\sim 10^{15-16}\,\mathrm{m}^{-3}$). The magnetic field dominates the solar atmosphere and structures the main morphology. The majority of solar activities are associated directly or indirectly with the dynamics of the magnetic field. These include the formation of sunspot groups, solar flares, coronal mass ejections and the solar winds.

Sunspot

A sunspot is a strong magnetic concentration on the photosphere of the Sun (cf. Fig. 1.1, 1.2 and 1.3, and the reviews of sunspot physics by Solanki 2003; Borrero & Ichimoto 2011). The existence of a strong magnetic field in sunspots suppresses the convection. Therefore, the temperature inside the sunspots is typically 3000-4500 K, lower than the surrounding plasma (about 5780 K). The temperature contrast with the surrounding photosphere renders sunspots as dark spots in the visible light emission. The sizes of sunspots can reach about 80,000 km in diameter. A sunspot evolves over a lifetime of about a few days or weeks. It is subject to expansion, contraction, rotation and differential motion relative to the surrounding plasma. Given their strong concentration of a single magnetic polarity, sunspots are

hosts of coronal loops, prominences, reconnection events, solar flares, and coronal mass ejections etc..

A sufficiently large sunspot is usually divided into two parts (cf. Fig. 1.2). The umbra (the central part) is the darkest region of a sunspot. The magnetic field in the umbra is approximately vertical (normal to the solar surface). The enclosing penumbra is slightly more illuminant, but still darker than the rest parts of the Sun's visible surface. Above a sunspot, magnetic field lines are inclined slightly in the umbra-penumbra border, and become even more tilted up to 90°, as they approach the penumbra-plage region. The plage region is filled with hot dense plasma and structured mainly by horizontal magnetic field lines (cf. Fig. 1.3).

The sunspot population rises and falls on a cycle of about 11 years. A peak in sunspot number is called a solar maximum, while a valley is a solar minimum. The sunspot number is a good indicator of the solar dynamics and the variation of the solar magnetic field, see Sec. 1.1.4 for more details.

Solar flares

A solar flare is a sudden energy release event observable over all layers of the solar atmosphere (the photosphere, chromosphere and corona). A huge amount of energy, up to 6×10^{25} J, is released in a time scale of hours (see reviews by Benz 2008; Shibata & Magara 2011). Flares are observable in all wavelengths from decametre radio waves, EUV/UV, X-rays to gamma-rays at 100 MeV. The mechanisms of flaring emission are still debated, but flares are known to be associated with plasma heating, magnetic reconnection, particle acceleration, mass ejection etc..

Solar flares are classified as A, B, C, M and X class, according to the peak flux in the X-ray band from 100 to 800 picometer measured near the Earth. Solar irradiation flux is constantly monitored, e.g., by the GOES spacecraft. Within each class, a linear scale is defined from 1 to 9. Say, if the flare peak flux is recorded at between 24.5% and 25.4 % of the flux difference between a M and X flare, a M2.5 flare is reported.

A flare can trigger several different kinds of transient events in the hosting active region and even further up, e.g. transverse oscillation of coronal loops (see review by Nakariakov & Verwichte 2005) and propagating fast waves (e.g. Liu et al. 2012; Yuan et al. 2013b). If a flare is directed towards the Earth, it takes 2–3 days for accelerated particles to reach the Earth. The particle flux may damage satellites, distort the ionosphere and affect radio communication. Predicting occurrence rate of solar flares is a key part of space weather forecasting.

Table 1.1: Estimation of coronal energy source for moderately large CMEs (Source: Chen 2011; Forbes 2000)

Form of energy	Energy density (Jm^{-3})	Observed average value
Kinetic ($\frac{1}{2}m_p n V^2$)	8×10^{-4}	$n = 10^{15}\,m^{-3}$, $V = 1\,kms^{-1}$
Thermal (nkT)	1×10^{-2}	$T = 10^6\,K$
Potential ($nm_p g h$)	5×10^{-2}	$h = 10^5\,km$
Magnetic ($B^2/2\mu_0$)	40	$B = 10^{-2}\,T$

Coronal mass ejection

A coronal mass ejection (CME) is a large burst of plasma out off the solar atmosphere, induced by the rearrangement of the complex magnetic field in the corona. It is notably associated with flares. The main difference is that solar flares affect all layers of the solar atmosphere, while most CMEs originate from the active regions that are believed to be the storage places of the coronal magnetic energy. A breakthrough of the equilibrium leads to the conversion of the magnetic energy into the kinetic energy of bulk plasma motions. The resulted mass ejection drags with itself the frozen-in magnetic field (see observational review by Webb & Howard 2012). It is a common idea that the free magnetic energy accumulated in the active region is the energy source of CMEs, see Table (1.1). The proposed mechanism includes flux cancellation, tether-cutting, breakout model, reconnection etc. (Chen 2011). CMEs are often associated with other large-scale transient activities, e.g. solar flares, coronal dimmings, global coronal (EIT) waves, erupting prominences, radio bursts. The physics of this association is not fully understood.

The Sun produces several CMEs per day near solar maxima, whereas near solar minima, it produces one every a few days. The CME speed, acceleration, mass and energy span 2–3 orders of magnitude (Vourlidas et al. 2002; Gopalswamy et al. 2006). The angular width is 3–10 times the size of the hosting active region (Yashiro et al. 2004). The above measurements were performed in the plane of sky. Using the STEREO satellites, 3D reconstruction enables measuring the real geometry of CMEs (e.g. Mierla et al. 2010, and references therein).

If a CME is oriented towards the Earth, it may cause major damages to satellites and affect the communication systems. It is a vital part of space weather prediction to estimate the probability of CME occurrence and its arrival time at the Earth.

Solar wind

The solar wind is a stream of charged particles released from the solar atmosphere, primarily electrons and protons. The solar wind consists of two components: the slow and fast solar wind. The slow solar wind has a characteristic speed of $\sim$400 km/s and a temperature of $1.4 - 1.6 \times 10^6$ K. Its chemical composition closely matches the solar corona. The fast solar wind has a typical speed at about 750 km/s, a temperature of 8×10^5 and a composition similar to the solar photosphere. This indicates that the slow and fast solar wind originate from different sources. The slow solar wind is more likely sourced from the streamer belt, while the fast solar wind dominates in the polar regions, in coronal holes (Marsch 2006). The coronal structure determines the solar wind properties. The open field structures yield steady fast solar wind. The transient open field regions generate unsteady slow solar wind. The active regions release fast energetic particles and magnetic flux, e.g. flares, CMEs. The solar wind carries the remnants from its origin, therefore it is also a medium for remote sensing (Marsch 2006). The Ulysses mission measured the speed dependence on the Sun's latitude (McComas et al. 2003). The latitudinal speed distribution reflects the morphology of the corona (see Fig. 1.4).

The heating and acceleration of solar wind is poorly understood. A combination of observations and simulations is required to explore the basic physics. It involves single fluid magnetohydrodynamic (MHD) simulations, multi-fluid models, or hybrid models (see review by Ofman 2010). Low-frequency waves (MHD) in the solar corona is a good candidate to explain the heating and acceleration of the solar wind, based on modern observations. In-situ measurements reveal a complex structure of the solar wind, and require to include the high-frequency waves (ion-cyclotron waves and beams).

1.1.4 Solar cycle

It was early in 1844 that the sunspot number was found to vary in a 11-year cycle (Schwabe 1844). Continuous observations and recordings of the sunspot number and areas solidly confirm that the solar activity is subject to a variation of a 11-years period (see Fig. 1.5). The Sun becomes less active (dormant) at solar minima and appears very dynamic at solar maxima, generating frequent flares, CMEs etc.. Besides the sunspot number, the sunspot area, location, total solar irradiance (and the components in different bands), magnetic field, and other transient phenomena are subject to solar activity cycles in a direct or indirect way. The solar cycle is widely believed to be associated with the solar dynamo (see review by Hathaway

2010). The gaseous Sun experiences differential rotation: the equatorial parts rotate faster than the higher latitude regions. The differential motion tears and twists the magnetic field, and hence causes amplification and filamentation. The toroidal magnetic field is generated, and in return, it re-generates the poloidal magnetic field. This process varies with the solar cycle (see Fig. 1.5, top panel). The total reversion of the solar magnetic poles occurs approximately every 22 years (see Fig. 1.5, bottom panel).

The 11-year solar activity cycle also modulates the p-mode helioseismic frequencies (see Broomhall et al. 2009). Recent findings show that, after removing the 11-year periodicity, the residual of frequency drift displays quasi-biennial variation (Broomhall et al. 2012). The source of this periodicity remains unrevealed.

1.1.5 Solar emission

The intensity $I(\lambda_{ij})$, emitted by an optically thin plasma at a wavelength λ_{ij} (or frequency ν_{ij}) via spontaneous transition from an energy level ϵ_j to a lower level ϵ_i, is defined as (the derivation follows Aschwanden 2005, Sec.2.8),

$$I(\lambda_{ij}) = \frac{h\nu_{ij}}{4\pi} \int N_j(X^{+m})A_{ji}dz, \qquad (1.1)$$

where A_{ji} is the Einstein coefficient of the spontaneous transition probability, $N_j(X^{+m})$ is the number density of the upper energy level j of the emitting ion X^{+m}, and z is the line-of-sight (LOS) through the emitting plasma. In the coronal approximation, the plasma is considered as of low density and optically thin. The collisional excitation rate of a lower energy state to the excitation state is balanced by the spontaneous emission rate. The population of the energy level j is expressed as,

$$N_j(X^{+m}) = \frac{N_j(X^{+m})}{N(X^{+m})} \frac{N(X^{+m})}{N(X)} \frac{N(X)}{n(H)} \frac{n(H)}{n_e} n_e \qquad (1.2)$$

where $N(X^{+m})/N(X)$ is the ionisation ratio of ion X^{+m} over the total number density of the element X, $A_X = N(X)/n(H)$ is the elemental abundance relative to hydrogen, $n(H)/n_e \approx 0.83$ is the ratio of hydrogen to free electron density. Normally an ion ratio of H : He = 10 : 1 is assumed for complete ionisation in the corona. The level population $N_j(X^{+m})/N(X^{+m})$ can be calculated with the CHIANTI code (Dere et al. 1997).

In practical solar applications, a contribution function $C(T, \lambda_{ij}, n_e)$ is intro-

duced to incorporate all the atomic physics related parameters

$$C(T, \lambda_{ij}, n_e) = \frac{h\nu_{ij}}{4\pi} \frac{A_{ji}}{n_e} \frac{N_j(X^{+m})}{N(X^{+m})} \frac{N(X^{+m})}{N(X)}. \tag{1.3}$$

Alternatively the abundance factor $A_X = N(X)/n(H)$ is included as well as a general contribution factor

$$G(T, \lambda_{ij}, A_X, n_e) = A_X C(T, \lambda_{ij}, n_e). \tag{1.4}$$

Then the line intensity is formulated as,

$$I(\lambda_{ij}) = A_X \int C(T, \lambda_{ij}, n_e) n_e n_H dz = \int G(T, \lambda_{ij}, A_X, n_e) n_e n_H dz. \tag{1.5}$$

Another convenient quantity widely used in the literature is the differential emission measure DEM(T). It is a measure of the amount of plasma along the line-of-sight that contributes to the emission of a plasma within the temperature interval $[T, T + dT]$ (Aschwanden 2005),

$$\frac{\text{DEM}(T)}{dT} = n_e n_H \frac{dz}{dT}. \tag{1.6}$$

Then the line emission intensity can be further simplified as (note that DEM(T) is also a differential operator),

$$I(\lambda_{ij}) = \int G(T, \lambda_{ij}, A_X, n_e) \frac{\text{DEM}(T)}{dT} dT \tag{1.7}$$

For a specific detector, an incident photon flux $I(\lambda, \vec{\theta})$ is a function of the wavelength and the incident angle to the detector. The value obtained by a pixel at a certain bandpass of the telescope is expressed as (Boerner et al. 2012),

$$p_l(\vec{x}) = \int_0^\infty \eta_l(\lambda) d\lambda \int_{\text{pixel } \vec{x}} I(\lambda, \vec{\theta}) d\vec{\theta}. \tag{1.8}$$

It is a combination of the integration of the incident photon flux $I(\lambda, \vec{\theta})$ over the solid angle occupied by the detector and the detector response over all wavelengths, where $\eta_l(\lambda)$ is the efficiency function of a certain channel of the telescope. It is a function of the flat-field function, camera gain, and a combination of the geometry, reflectance and transmission efficiencies of the mirrors, quantum effects and correction for the CCD degradation. The index l indicates the lth channel of the telescope. All these are combined into a wavelength-dependent instrument response function,

$$K_l(T) = \int_0^\infty G(\lambda, T) R_l(\lambda) d\lambda. \tag{1.9}$$

Then the value obtained by a pixel in the CCD detector is formulated simply as,

$$p_l(\vec{x}) = \int_0^\infty K_l(T)\mathrm{DEM}(T, \vec{x})\mathrm{d}T. \tag{1.10}$$

The value p_l is now partitioned into an instrumental response term K_l and a plasma-related term DEM. This equation can be inverted to obtain the differential emission measure DEM for a given set of observations p_l and the instrument calibration K_l. The examples can be found in Aschwanden & Boerner (2011) using forward modelling and Hannah & Kontar (2012) with the matrix inversion method.

1.1.6 Instruments

Coronal waves are confidently observed with space-borne and ground-based observatories in radio emission, visible light, UV/EUV and X-ray bandpasses. In particular, modern EUV imaging telescopes retain high temporal and spatial resolutions to detect wave and oscillatory activities, i.e. Transitional Region And Coronal Explorer (TRACE), Solar TErrestrial RElation Observatory (STEREO) /Extreme UltraViolet Imager (EUVI), Solar Dynamic Observatory (SDO)/Atmospheric Imaging Assembly (AIA). In this section, I introduce the key instruments used in this thesis.

Transition Region and Coronal Explorer (TRACE)

The Transition Region and Coronal Explorer (TRACE, see Fig. 1.6 and Handy et al. 1999) was a small satellite explorer program to investigate the dynamics of the magnetised plasma at the transition region and corona with high temporal and spatial resolution. TRACE was launched in April 1998. It was scheduled to perform joint observation programmes with the Solar and Heliospheric Observatory (SOHO) during the rising phase of solar cycle 23 to the solar maximum. It roughly ridged in a solar-synchronous polar orbit, approximately followed the solar terminator. It obtained precisely coaligned image sequences of the photosphere, transition region and corona with uninterrupted observations for up to 8 months. In the optical system, the visible light was excluded by three thin film aluminium filters. The primary and secondary mirrors were coated and optimised for one of the EUV wavelengths. After passing the mirrors, the EUV lights hit the fluorescent lumogen coating of the CCD camera. The $1k \times 1k$ CCD detector collected images over an $8.5' \times 8.5'$ field-of-view (FOV), filtered by one of the four normal-incidence coatings optimised for EUV and UV wavelengths. TRACE provided continuous observations over three EUV channels at 171 Å, 195 Å and 284 Å and four UV channels at 1,216 Å, 1,550 Å, 1,600 Å and 1,700 Å. It covered a temperature range from 6,000 K to 10 MK. The resolution

was $0.5''$ per pixel, and the cadence time could be as short as 10 s. The TRACE mission captured its last science image at 24:56 UT 21 June 2010 and was superseded by its successor SDO/AIA, which provides continuous full-disk observation at 9 channels and a white light channel for coalignment purpose.

Atmospheric Imaging Assembly (AIA)

The Solar Dynamics Observatory (SDO, see Fig. 1.7, Pesnell et al. 2012) is a part of NASA's *Living With a Star* program. It was launched on 11 Feb 2010. It orbits in a circular geosynchronous orbit inclined by 28 degrees. SDO mainly investigates the generation and structuring of the Sun's magnetic fields, the energy storage mechanism, their release to the heliosphere and geospace as solar wind and energetic particles, and the variations in the solar irradiance (Pesnell et al. 2012). The SDO mission includes three observational instruments (see Fig. 1.7): the Atmospheric Imaging Assembly (AIA), the Helioseismic and Magnetic Imager (HMI) and the Extreme Ultraviolet Variability Experiment (EVE).

The Atmospheric Imaging Assembly (AIA, Lemen et al. 2012; Boerner et al. 2012) onboard SDO provides simultaneous observations of the Sun in multiple bandpasses since 29 March 2010. It images the full solar disk up to 1.5 solar radii with $4k \times 4k$ CCD detectors at a resolution of 0.6 arcsec/pixel. A high cadence (~12 s) can be sustained during most of the mission. The Sun is imaged in 10 different narrowband channels, seven of them are EUV bandpasses: Fe XVIII (94 Å), Fe VIII,XXI (131 Å), Fe IX (171 Å), Fe XII,XXIV (193 Å), Fe XIV (211 Å), He II (304 Å), Fe XVI (335 Å), see Table (1.2). The observed temperature in the EUV bands ranges from about 0.6 MK to about 16 MK. AIA observations cover the upper transition region, quiet corona, active-region corona, and flaring regions quite well. There are also two UV channels: C IV line (1,600 Å) and the continuum (1,700 Å). These two channels image the transition region, upper photosphere and temperature minimum, see Table (1.2). A white light channel in 4,500 Å records the visible surface of the Sun hourly, it mainly provides a reference for co-alignment purpose.

The AIA images are stored as level 0 images, 16–bit integer $4k \times 4k$ arrays. They are Rice-compressed (Rice & Plaunt 1971) before they are sent to the ground storage facility. The over-scan rows and columns are removed on-orbit, occasionally these parts are retained for CCD engineering purpose (Lemen et al. 2012). The second step of the image processing is to remove the digital offset, CCD read noise and dark current. Then in step 3, the AIA images are corrected with a flat-field. This is to account for the non-uniformity of the CCD detector. In step 4, the bad pixels (Their number is much less than 0.1% of the total pixel number, Lemen

Table 1.2: AIA observational channels, the primary ions causing the emission, targeted levels in the solar atmosphere, and the characteristic responsive temperature (Source: Lemen et al. 2012)

Channel	Primary ion(s)	Region of atmosphere	Char. $\log(T)$
4500 Å	continuum	photosphere	3.7
1700 Å	continuum	temperature minimum, photosphere	3.7
304 Å	He II	chromosphere, transition region	4.7
1600 Å	C IV+cont.	transition region, upper photosphere	5.0
171 Å	Fe IX	quiet corona, upper transition region	5.8
193 Å	Fe XII, XXIV	corona and hot flare plasma	6.2, 7.3
211 Å	Fe XIV	active-region corona	6.3
335 Å	Fe XVI	active-region corona	6.4
94 Å	Fe XVIII	flaring corona	6.8
131 Å	Fe VIII, XXI	transition region, flaring corona	5.6, 7.0

et al. 2012) are identified and replaced by interpolated values from neighbouring pixels. A special algorithm is implemented to remove the spikes caused by the energetic particles from cosmic rays or the Sun itself. The AIA despike algorithm was adopted from the TRACE program. The values of the spikes were replaced by the median value of its neighbouring pixels. The spike values and their locations are stored separately and are easily reversible (Lemen et al. 2012). In the final step, the AIA images are flipped by 180° to upright the solar north in the image array. After implementing the above steps, the level 1 data are obtained. The level 1 data are available and ready for exportation from the Joint Science Operations Center (JSOC, Stanford) as FITS files in 32-bit floating numbers. The only thing that is not calibrated is the deconvolution of the instrument point spread function and the diffraction patterns, these are wavelength-dependent features.

The level 1.5 data processing starts with the level 1 data. The four AIA telescopes aligned prior to the launch are further adjusted to align the small residual roll angle. The AIA images have slightly different plate scale sizes, all the images are interpolated into a uniform 0.6″ plate scale. The telescope pointings are slightly offset, so the boresight is co-aligned by adjusting in-orbit the secondary mirror offsets. The residual differences are removed by interpolating the images into a new global pixel coordinate centred at the solar disk. After these processing steps, the images are rounded off as 16-bit integer values.

The AIA data sets are publicly available in a number of formats and at several data centres, see Hurlburt et al. (2012).

Michelson Doppler Imager (MDI)

The Michelson Doppler Imager (MDI, see Fig. 1.8, Scherrer et al. 1995) is an instrument package onboard the SOlar and Heliosphere Observatory (SOHO), which was launched in December 1995. MDI is an international collaboration of the Solar Oscillation Investigation program. It is aimed to study the interior structure and the dynamics of the Sun. It continuously measures the line-of-sight velocity, line core intensity and magnetic field at the photospheric level. The MDI's main target is the helioseismical study of the solar interior. The strong magnetic field was found to modify the spectra of the solar oscillations, so it is also MDI's primary measurements. In our study, we only used the LOS magnetic field measured by MDI to perform the magnetic field extrapolation. Therefore we only briefly introduce the technique details on the LOS magnetic field.

MDI is a refracting telescope. The incident photon flux undergoes a cascade of filters and then impinges on the CCD camera (Scherrer et al. 1995). Two tuneable Michelson interferometers scan across the Ni I 6,768 Å solar absorption line with a 94 mÅ linewidth. The velocity, continuum intensity and LOS magnetic field are computed with the assistance of a set of filtergrams. The MDI's camera records images of 1024×1024 pixels. It can operate in full disk mode with a FOV of $34' \times 34'$ and a resolution of 4 arcsec/pixel. Or alternatively, it performs in high-resolution mode with a FOV of $10.5' \times 10.5'$ and a resolution of 1.25 arcsec/pixel. MDI has a structure observation mode, the full-disk data are re-binned into a 192×192 pixels onboard and transmitted to the ground station every minute. The cadence time for all the observation modes are 1 min, this defines the Nyqvist frequency of 8.33 mHz.

MDI instrument operations were terminated on 12 April 2012 and were been superseded by SDO/HMI, which will be presented as follows.

Helioseismic and Magnetic Imager (HMI)

The Helioseismic and Magnetic Imager (HMI, Schou et al. 2012) onboard the SDO satellite is a new and improved version of its predecessor MDI. It continues the helioseismic and magnetic field observations of the Sun for solar cycle 24. HMI detects the motions of the solar photosphere to study the solar oscillations through Doppler shift measurements, and computes three components of magnetic field vectors at the photosphere.

HMI observes the full-disk in the Fe I absorption line at 6,173 Å with a 76 mÅ linewidth. HMI records a set of 12 images of the Sun, each image ($4k \times 4k$ pixels) is tuned by a set of filter in a range of ± 680 mÅ centred at $6,173.1\,\text{Å} \pm 0.1\,\text{Å}$ (Schou

et al. 2012). A map of Dopplergrams (surface velocity) is computed on the ground with this image set. The resolution is about 0.50 arcsec/pixel, the cadence time is 45 s, and the velocity precision is as good as 13 m/s (Schou et al. 2012).

For the magnetic field measurement, a polarisation selector is required to measure the Stokes parameters (I, Q, U, V). This comprises a set of wave plates that can be rotated to different orientations and detect different polarisation parameters. The LOS magnetic field is provided at an accuracy of 10 G every 45 s. The vector magnetic field is computed every 90 s at an accuracy of 18 G for sunspots and 220 G for the quiet Sun (Schou et al. 2012).

Nobeyama Radioheliograph (NoRH)

The Nobeyama Radioheliograph (NoRH, see Fig. 1.9 and Nakajima et al. 1994) is a ground-based radio-interferometer, dedicated to observe the Sun at high spatial and temporal resolution. It consists of 84 parabolic antennas, 80 cm each in diameter. It is a T-shaped construction, 490 m long in the East/West direction and 220 m in the North/South direction. It started providing 8-hour daily observation of the Sun since April 1992. The observation frequency is 17 GHz in both intensity and right/left circular polarisation. A second observation band was added in 34 GHz but only in intensity measure. The spatial resolution is $10''$ at 17 GHz and $5''$ at 34 GHz, the cadence is 1 sec at normal operation, while at event mode, it can be as good as 0.1 sec.

The free-free emission from the thermal plasma (thermal bremsstrahlung) is within the frequency range at $\nu \geq 1$ GHz, well within the NoRH's detection range. The gyroresonance emissions at frequencies $\nu = 2\pi s \Omega_e$ are generated by the electrons gyrating around the magnetic field, where Ω_e is the electron gyrofrequency, s is the harmonic number. $s = 1, 2, 3, 4$ are usually observed for thermal electrons. For the mildly relativistic electrons, $s \approx 10 - 100$ are commonly detected, it is called gyrosynchrotron emission. During a flare, non-thermal electrons are accelerated, if they are trapped by the strong magnetic field lines, gyrosynchrotron emission are usually observed.

1.2 Magnetohydrodynamic waves and oscillations

1.2.1 MHD wave theory

Magnetohydrodynamics (MHD) describe the dynamics of a conducting fluid. It incorporates the basic processes resulted from the interactions between the charged

particles, and induced/external electromagnetic fields, as well as the basic fluid effects. Mathematically, it is a combination of the Navies-Stokes equations of fluid dynamics and a reduced version of Maxwell's equations.

The ideal MHD assumes an adiabatic plasma moving at a non-relativistic speed. The collisional time scale is required to be much shorter than the MHD time scale so that the particle distribution follows approximately the Maxwellian distribution (Aschwanden 2005). The ideal MHD equations include the continuity equation, the momentum (Euler) equation, the adiabatic energy equation, Maxwell's equations and Ohm's law (the derivations were done in S.I. units following the context in Aschwanden 2005),

$$\frac{D\rho}{Dt} + \rho\nabla\vec{v} = 0 \tag{1.11}$$

$$\rho\frac{D\vec{v}}{Dt} = -\nabla p - \rho\vec{g} + \vec{j} \times \vec{B} \tag{1.12}$$

$$\frac{D}{Dt}(p\rho^{-\gamma}) = 0 \tag{1.13}$$

$$\nabla \times \vec{B} = \mu_0\vec{j} \tag{1.14}$$

$$\nabla \times \vec{E} = -\frac{\partial\vec{B}}{\partial t} \tag{1.15}$$

$$\nabla \cdot \vec{B} = 0 \tag{1.16}$$

$$\vec{E} = -\vec{v} \times \vec{B} \tag{1.17}$$

The quantity ρ is the total plasma density ($\rho = n_p m_p + n_e m_e \simeq n_p m_p = n_e m_p$, where n_p and n_e are proton and electron number densities, $n_e = n_p$ is assumed in a quasi-neutral plasma, m_p and m_e are proton and electron masses), $\vec{v}$ is the bulk velocity of the plasma, $D/Dt = \partial/\partial t + \vec{v}\cdot\nabla$ is the operator of the total derivative, p is the isotropic plasma pressure, $\vec{g}$ is the solar gravitational acceleration, $\vec{j}$ represents the induction current density vector, $\vec{B}$ and $\vec{E}$ are the magnetic and electric fields, γ denotes the adiabatic index.

Considering a static isothermal uniform plasma with an equilibrium gas pressure p_0 and density ρ_0, the MHD equations (Eq.1.11-1.17) can be re-written in a more traditional form, with only the observable variables ρ, $\vec{v}$, and $\vec{B}$:

$$\frac{D\rho}{Dt} + \rho\nabla\vec{v} = 0 \tag{1.18}$$

$$\rho\frac{D\vec{v}}{Dt} = -c_s^2\nabla\rho - \rho\vec{g} + \frac{1}{\mu_0}[-\frac{1}{2}\nabla B^2 + (\vec{B}\cdot\nabla)\vec{B}] \tag{1.19}$$

$$\frac{\partial\vec{B}}{\partial t} = -\vec{B}(\nabla\cdot\vec{v}) + (\vec{B}\cdot\nabla)\vec{v} - (\vec{v}\cdot\nabla)\vec{B}, \tag{1.20}$$

where $c_s^2 = \gamma p_0/\rho_0$ is the square of the sound speed, and the ideal gas law gives $\nabla \cdot p = c_s^2 \nabla \cdot \rho$.

We assume that the homogeneous magnetic field is in the z-direction, $\vec{B}_0 = (0, 0, B_0)$. The associated Alfvén speed is $v_A = B_0/\sqrt{\mu_0 \rho_0}$. Assume the observables (plasma density, velocity and magnetic field) consist of an equilibrium value and a small perturbation term,

$$\rho(\vec{x}, t) = \rho_0 + \rho_1(\vec{x}, t) \tag{1.21}$$

$$\vec{v}(\vec{x}, t) = \vec{v}_1(\vec{x}, t) \tag{1.22}$$

$$\vec{B}(\vec{x}, t) = \vec{B}_0 + \vec{B}_1(\vec{x}, t), \tag{1.23}$$

where the subscript 1 denotes the first order perturbations. The velocity has to fullfil the condition $|\vec{v}_1| \ll \min\{c_s, v_A\}$ in order to be considered as first order perturbation variable. Substitute the perturbations in Eq.(1.21-1.23) into in Eq.(1.18-1.20) and neglect the gravitational term $(-\rho_0 \vec{g})$ and the nonlinear terms. After some re-arrangements, we obtain

$$\left[\frac{\partial^2}{\partial t^2} - \left(v_A \frac{\partial}{\partial z^2} \right)^2 \right] j_z = 0 \tag{1.24}$$

$$\frac{\partial^4 \nabla \cdot \vec{v}}{\partial t^4} - (c_s^2 + v_A^2) \frac{\partial^2}{\partial t^2} \nabla^2 \nabla \cdot \vec{v} + c_s^2 v_A^2 \frac{\partial^2}{\partial z^2} \nabla^2 \nabla \cdot \vec{v} = 0, \tag{1.25}$$

where j_z is the field-aligned component of the electric current density.

In order to obtain the dispersion relation, the perturbations in Eq.(1.21-1.23) are decomposed into Fourier components. They are expressed in form of a harmonic spatio-temporal function, $\exp[i(\vec{k}\vec{x} - \omega t)]$. The dispersion relations for the MHD waves in a static uniform equilibrium are

$$\omega^2 - v_A^2 k_z^2 = 0, \tag{1.26}$$

$$\omega^4 - k^2(c_s^2 + v_A^2)\omega^2 + k_z^2 k^2 c_s^2 v_A^2 = 0. \tag{1.27}$$

Eq. (1.26) describes the essentially incompressible Alfvén wave. Eq. (1.27) represents the fast and slow magnetoacoustic wave. The Alfvén wave is strictly confined to the magnetic field lines. It does not perturb the plasma density, therefore it is not observable as intensity emission perturbation. The slow magnetoacoustic wave, in the typical corona regime ($c_s^2 \ll v_A^2$) is also almost constrained along the direction of the magnetic field. The slow-mode wave is essentially compressive, the density and pressure are modulated at the first order disturbances. In the limiting case of

parallel propagation, the slow magnetoacoustic wave degenerate into a usual sound wave and propagate at the local sound speed. Therefore it is observable with imaging instruments, if the perturbations integrated along the line-of-sight are significant (see e.g. Gruszecki et al. 2012). The fast magnetoacoustic wave is also compressive. In contrast to the Alfvén and slow waves, it can propagate across magnetic field lines or obliquely. In the solar corona, the propagation speed of a fast wave is at about the Alfvén speed v_A in all directions. In the case of parallel propagation, a fast wave degenerate into an Alfvén wave and become incompressible.

1.2.2 MHD waves in structured plasmas

In the coronal conditions, the plasma is dominated by the magnetic field. Due to very complex plasma dynamics, evident structuring of the solar corona by the magnetic field is very significant. Various forms of plasma morphology are structured, e.g., coronal loops, coronal holes, prominences, polar plumes, the plasma density and temperature respond self-consistently to the magnetic field structuring. In coronal MHD seismology, a plasma cylinder is used to model coronal loops. In the next section, I give the MHD theory in detail.

MHD modes of a plasma cylinder

A plasma cylinder stretched along magnetic field lines is believed to model well coronal loops, sunspots, filaments and polar plumes. The standard model is a simple straight cylinder filled with hot plasma (see Fig. 1.10 and Edwin & Roberts 1983a). The cylinder interior is filled with a uniform plasma of density ρ_0 and pressure p_0. It is permeated in a magnetic field of $B_0\hat{z}$, parallel to the axis of the cylinder. The associated sound speed and Alfvén speed are defined as $C_{s0}^2 = \gamma p_0/\rho_0$, $C_{A0}^2 = B_0^2/(\mu_0\rho_0)$, respectively. One can also define a useful tube speed, $C_{T0}^2 = C_{s0}^2 C_{A0}^2/(C_{s0}^2 + C_{A0}^2)$. The exterior is the ambient plasma of density ρ_e and pressure p_e in a magnetic field $B_e\hat{z}$. The corresponding sound speed, Alfvén speed and tube speed are $C_{se}^2 = \gamma p_e/\rho_e$, $C_{Ae}^2 = B_e^2/(\mu_0\rho_e)$ and $C_{Te}^2 = C_{se}^2 C_{Ae}^2/(C_{se}^2 + C_{Ae}^2)$.

The existence of such a system in an equilibrium state requires that the total internal and external pressure (i.e. gas pressure and magnetic pressure) are balanced at the boundary. It is stated as,

$$p_0 + \frac{B_0^2}{2\mu_0} = p_e + \frac{B_e^2}{2\mu_0} \tag{1.28}$$

Using the relationship between the pre-defined characteristic speeds, we obtain a

condition on the characteristic speeds,

$$\rho_0\left(\frac{C_{s0}^2}{\gamma} + \frac{C_{A0}^2}{2}\right) = \rho_e\left(\frac{C_{se}^2}{\gamma} + \frac{C_{Ae}^2}{2}\right). \tag{1.29}$$

Another frequently-used characteristic speed is the so-called kink speed,

$$C_k = \left(\frac{B_0^2 + B_e^2}{\mu_0(\rho_0 + \rho_e)}\right)^{1/2} = \left(\frac{\rho_0 C_{A0}^2 + \rho_e C_{Ae}^2}{\rho_0 + \rho_e}\right)^{1/2} \tag{1.30}$$

It can be understood as the density-weighted average Alfvén speed. In the long wavelength limit, the phase speed of all but fast sausage modes approaches this value.

The derivation of MHD wave dispersion relations is based on the linearisation of the MHD equations with respect to the equilibrium state. The Fourier decompositions of the perturbed physical quantities are expressed in the form $\exp[i(k_z z + m\phi - \omega t)]$, where k_z is the z-component of the wave vector, m is an integer azimuthal wave number, ϕ is the azimuthal angle, ω is the angular frequency. A coupled first-order ordinary differential equation describes the radial structure of the perturbations (Sakurai et al. 1991; Nakariakov & Verwichte 2005),

$$D\frac{d}{dr}(r\xi_r) = (C_s^2 + C_A^2)(\omega^2 - C_T^2 k_z^2)\left(\kappa^2 + \frac{m^2}{r^2}\right)r\delta P_{tot} \tag{1.31}$$

$$\frac{d}{dr}(\delta P_{tot}) = \rho_0(\omega^2 - C_A^2 k_z^2)\xi_r \tag{1.32}$$

$$-\frac{im}{r}\delta P_{tot} = \rho_0(\omega^2 - C_A^2 k_z^2)\xi_\phi \tag{1.33}$$

where ξ_r and ξ_ϕ are the perturbations displacement in the radial and azimuthal directions, and δP_{tot} is the perturbation to the total pressure. The parameters D and κ are defined as,

$$D = \rho_0(C_s^2 + C_A^2)(\omega^2 - C_A^2 k_z^2)(\omega^2 - C_T^2 k_z^2), \tag{1.34}$$

$$\kappa^2(\omega) = -\frac{(\omega^2 - C_s^2 k_z^2)(\omega^2 - C_A^2 k_z^2)}{(C_s^2 + C_A^2)(\omega^2 - C_T^2 k_z^2)}. \tag{1.35}$$

Eq. (1.31) and Eq. (1.32) can be rewritten as

$$(\omega^2 - C_{A\alpha}^2 k_z^2)\left[\frac{d^2}{dr^2} + \frac{1}{r}\frac{d}{dr} - \left(\kappa_\alpha^2 + \frac{m^2}{r^2}\right)\right]\delta P_{tot} = 0. \tag{1.36}$$

The subscript $\alpha = 0, e$ corresponds to the internal and external media, respectively. The first term in Eq. (1.36) describes the torsional Alfvén wave. The second term

gives the solution of the fast and slow magnetoacoustic wave. Solving Eq. (1.36) by applying the boundary conditions, namely balancing the perturbations of the total pressures and the radial displacements at the cylinder boundary, we obtain,

$$\rho_e(\omega^2 - C_{Ae}^2 k_z^2)\kappa_0 \frac{I_m'(\kappa_0 a)}{I_m(\kappa_0 a)} - \rho_0(\omega^2 - C_{A0}^2 k_z^2)\kappa_e \frac{K_m'(\kappa_e a)}{K_m(\kappa_e a)} = 0 \qquad (1.37)$$

where I_m and K_m are the modified Bessel functions of order m, the parameters κ_e and κ_0 are the transverse wave numbers in the external and internal media:

$$\kappa_\alpha^2(\omega) = -\frac{(\omega^2 - C_{s\alpha}^2 k_z^2)(\omega^2 - C_{A\alpha}^2 k_z^2)}{(C_{s\alpha}^2 + C_{A\alpha}^2)(\omega^2 - C_{T\alpha}^2 k_z^2)}, \; \alpha = 0, e. \qquad (1.38)$$

For the body modes that oscillate inside the tube and are evanescent outside, the conditions $\kappa_0^2 < 0$ and $\kappa_e^2 > 0$ have to be fulfilled. The choice of the modified Bessel function of the second kind, K_m instead of the Hankel function excludes the leaky solutions.

The azimuthal number m defines the symmetry of the wave mode of the plasma cylinder. MHD wave modes with $m = 0$ are the *sausage* modes that are axisymmetric wave modes inside the cylinder's cross-section, accompanied by the perturbations of the plasma density and magnetic field. Solutions with $m = 1$ are the *kink* modes. These modes displace the cylinder axis, and cause relatively weak perturbations of its cross-section and density. Wave modes with higher m are usually referred to as *flute*, *ballooning* or *whispering* modes.

Theoretical modelling of the MHD waves and oscillations detected in various regions of the solar atmosphere requires accounting for additional effects, such as nonlinearity, gravitational stratification, various mechanisms for dissipations (viscosity, thermal conduction, radiation, resistivity, see e.g. Stepanov et al. 2012). In the following we shall concentrate on several theoretical results, directly relevant to the interpretation of wave phenomena described in the thesis.

Slow magnetoacoustic waves in coronal loops

Propagating slow magnetoacoustic (or longitudinal) waves are commonly observed in active region loops and polar plumes (see e.g., Yuan & Nakariakov 2012; Ofman et al. 1999). An adequate description of the wave feature requires to account for the effects of gravitational stratification, magnetic field curvature, nonlinearity and dissipation. The evolutionary equation for slow waves in a semi-circular coronal loop

filled with a dissipative plasma was derived by Nakariakov et al. (2000):

$$\frac{\partial \rho}{\partial t} + \frac{\partial}{\partial s}(\rho v) = 0 \tag{1.39}$$

$$\rho \left(\frac{\partial v}{\partial t} + v \frac{\partial v}{\partial s} \right) = -\frac{\partial p}{\partial s} - g\rho + \frac{4}{3}\eta_0 \frac{\partial^2 v}{\partial s^2} \tag{1.40}$$

$$\frac{1}{\gamma - 1} \left(\frac{\partial p}{\partial t} - \frac{\gamma p}{\rho} \frac{\partial \rho}{\partial t} \right) = \frac{\partial}{\partial s} \left(\kappa_{\shortparallel} \frac{\partial T}{\partial s} \right), \tag{1.41}$$

where s is the curve length along the magnetic field line, $\rho(s)$, $v(s)$, $p(s)$ and $T(s)$ are the plasma density, longitudinal speed, plasma pressure, and plasma temperature, respectively, and $\kappa_{\shortparallel} = \kappa T^{5/2}$ is the thermal conductivity along the magnetic field, η_0 is the compressive viscosity coefficient, and $g(s)$ is the gravitational acceleration along the loop coordinate s,

$$g(s) = g_\odot \cos \left(\frac{s}{r} \right) \left(1 + \frac{r}{R_\odot \sin(\frac{s}{r})} \right)^{-2}. \tag{1.42}$$

where r is the distance from the geometric center of the semi-circle to the axis of the tube.

Considering weak perturbations affected by a weak dissipation, Eq.(1.39 to 1.41) lead to the modified Burgers equation, which can be solved by introducing the Fourier components,

$$\frac{\partial v}{\partial s} - \frac{v}{2\lambda_n} + \frac{\gamma + 1}{2c_s} v \frac{\partial v}{\partial \xi} - \frac{R_\odot \rho_0(0)\bar{\eta}}{2\rho_0(s)} \frac{\partial^2 v}{\partial \xi^2} = 0 \tag{1.43}$$

$$v(s) = v(0) \exp \left[\int_0^s \left(\frac{1}{2\lambda_n(x)} \right) - \frac{R_\odot \rho_0(0)\bar{\eta} k^2}{2\rho_0(x)} dx \right], \tag{1.44}$$

where $\xi = s - c_s t$ is the co-moving coordinate in the sound speed frame, $\lambda_n(s) = c_s^2/(\gamma g)$ is the local density scale height, $k = \omega/c_s$ is the wave number, and $\bar{\eta}$ is defined as

$$\bar{\eta} = \frac{1}{\rho_0(0)c_s R_\odot} \left[\frac{4\eta_0}{3} + \frac{\kappa_{\shortparallel}(\gamma - 1)^2}{R_{\mathrm{gas}}\gamma} \right].$$

where R_{gas} is gas constant.

Solution in Eq. (1.44) shows that the wave amplitude initially grows with height, reaches maximum before approaching the loop top. The slow waves with amplitudes higher than several percents of the background values are subject to non-linear steepening. The non-linear effect resulted in enhanced dissipation (Nakariakov et al. 2000).

Whispering modes

The magnetoacoustic wave with higher-order azimuthal mode ($m > 1$) is rather rarely detected in observations, however they may be responsible for some observed phenomena, e.g., the 5-min oscillations in the umbra-penumbra boundary of sunspots. The theory of the whispering modes inside a plasma cylinder was developed by Zhugzhda et al. (2000). Below we summarise the key points.

The MHD wave model of a plasma cylinder (Edwin & Roberts 1983b) was extended to describe sunspot oscillations (Zhugzhda et al. 2000) with the main physics unchanged. The azimuthal modes with $m = 0, 1$ (sausage and kink modes) are well studied theoretically and observationally in the coronal loops, polar plumes, spicules etc. The high-order azimuthal modes with $m > 1$ are usually not resolved in spatial scale with modern instruments, however, such whispering modes are detectable in sunspots.

Let us introduce the dimensionless parameters:

$$l = \frac{C_s}{C_A}, \ \delta = \frac{C_{se}^2}{C_{s0}^2}, \ \Delta = \frac{\rho_e}{\rho_0} = \frac{2l^2 + \gamma}{2\delta l^2}, \tag{1.45}$$

and the dimensionless variables:

$$h = kr, \ \Omega = \frac{\omega}{kC_{T0}}, \ j = \kappa_0 r. \tag{1.46}$$

The dispersion relation of Eq. (1.37) are expressed in the dimensionless variables as

$$(1 + l^2 - l^2 \Omega_b) m_b h \frac{K_{m+1}(m_b h)}{K_m(m_b h)} + l^2 \Omega_b^2 \frac{J_{m+1}(j)}{J_m(j)} = 0, \tag{1.47}$$

where

$$m_b = \sqrt{\frac{\delta(1 + l^2) - \Omega_b^2}{\delta(1 + l^2)}}, \Omega_b^2 = \frac{2}{1 \pm \sqrt{1 - 4l^2 h^2 d^{-1}}}, \tag{1.48}$$

and

$$d = (1 + l^2)^2 (h^2 + j^2). \tag{1.49}$$

The plus and minus signs in Eq. (1.48) correspond to the slow and fast modes, respectively. For a given value of h and a set of plasma dimensionless parameters, l, Δ, and δ, the solutions for j can be solved numerically. The frequency can be found by inserting j into Eq. (1.47).

For the linear running MHD waves guided by a vertical flux tube, the relative perturbations of the velocity and magnetic field are expressed as functions of the

radial distance from the cylinder centre r and the azimuthal angle θ:

$$\frac{v_z}{C_s} = -\frac{iA_0 k_z C_s}{\omega^2} J_m(\frac{jr}{a}) \exp i(k_z z + m\theta + \omega t), \tag{1.50}$$

$$\frac{\delta B_z}{B_z} = \frac{iA_0(\omega^2 - k_z^2 C_s^2)}{\omega^3} J_m(\frac{jr}{a}) \exp i(k_z z + m\theta + \omega t), \tag{1.51}$$

$$\frac{v_r}{C_s} = \frac{A_0(\omega^2 - k_z^2 C_s^2)a}{j\omega^2 C_s} J_{m+1}(\frac{jr}{a}) \exp i(k_z z + m\theta + \omega t), \tag{1.52}$$

$$\frac{\delta B_r}{B_z} = \frac{A_0(\omega^2 - k_z^2 C_s^2)k_z a}{j\omega^3} J_{m+1}(\frac{jr}{a}) \exp i(k_z z + m\theta + \omega t), \tag{1.53}$$

where A_0 is an arbitrary constant, and j is a root of the dispersion relation in Eq. (1.37). In case of the standing waves, the phase components are replaced with $\cos \omega t \sin k_z z \sin m\theta$ for v_z and δB_r and $\sin \omega t \cos k_z z \cos m\theta$ for v_r and δB_z. These expressions provide observational basis to detect the whispering modes.

The amplitude ratio of the magnetic field and the longitudinal velocity for the body wave modes gives a simple observation basis (Zhugzhda et al. 2000),

$$BV = \frac{\delta B_z}{B_z} / \frac{V_z}{C_s} = \frac{k_z^2 C_s^2 - \omega^2}{\omega k_z C_s} = \frac{1 + l^2 - \Omega_b^2}{\Omega_b \sqrt{1 + l^2}}. \tag{1.54}$$

Eq. (1.54) provide a direct observation basis for running body wave modes inside sunspots. For the standing body wave, the above expression is slightly modified,

$$BV = \frac{\delta B_z}{B_z} / \frac{V_z}{C_s} = \frac{1 + l^2 - \Omega_b^2}{\Omega_b \sqrt{1 + l^2}} \cos k_z z. \tag{1.55}$$

It is a function of the observational height z in the solar atmosphere.

1.2.3 MHD waves in gravitationally stratified plasmas

Magnetoacoustic gravity waves

In the simple verison of MHD wave theory, the density and pressure stratification is usually neglected. The temperature does not exhibit significant variation over height in the coronal condition, hence the plasma can be considered approximately isothermal. Following Bel & Mein (1971), we consider the linear propagation of MHD waves in an isothermal gravititionally stratified atmosphere permeated by a uniform magnetic field. The z-axis is assumed to be directed along the gravitational stratification. The gravitational field $\vec{g}$ and the magnetic field $\vec{B}$ are taken in the

(x, z) plane, so that

$$\vec{g} = (0, 0, g_z) \tag{1.56}$$

$$\vec{B}_0 = (B_x, 0, B_z). \tag{1.57}$$

The hydrostatic equilibrium state is assumed as exponential stratification,

$$\rho_{\mathrm{eq}} = \rho_0 \exp(-z/H) \tag{1.58}$$

$$P_{\mathrm{eq}} = P_0 \exp(-z/H), \tag{1.59}$$

where ρ_0 and P_0 are the density and pressure at a reference level, $H = C_s^2/\gamma \, |g|$ is the scale height, and C_s is the constant sound speed.

Assume that the density, pressure and magnetic field consist of an equilibrium value plus a small perturbation term:

$$\rho = (\rho_0 + \rho') \exp(-z/H) \tag{1.60}$$

$$P = (P_0 + P') \exp(-z/H) \tag{1.61}$$

$$\vec{B} = \vec{B}_0 + \vec{B}', \tag{1.62}$$

where ρ', P' and $\vec{B}'$ are the perturbation terms. Inserting these quantities into the MHD equations, and eliminating the perturbations of the density, pressure and the magnetic field, we obtain an equation for the velocity $\delta\vec{\tilde{v}}$. It is also a small quantity

$$\frac{\partial^2}{\partial t^2} \delta\vec{\tilde{v}} - C_s^2 \nabla\nabla \cdot \delta\vec{\tilde{v}} - \nabla(\delta\vec{\tilde{v}} \cdot \vec{g})$$
$$-(\gamma - 1)\vec{g}\nabla \cdot \delta\vec{\tilde{v}} + \frac{1}{4\pi}\rho_{\mathrm{eq}}\vec{B} \times (\nabla \times \nabla \times (\delta\vec{\tilde{v}} \times \vec{B})) = 0. \tag{1.63}$$

The wave component is assumed to be a plane wave form,

$$\delta\vec{\tilde{v}} = \delta\vec{v} \exp i(\vec{k}\vec{r} - \omega t), \tag{1.64}$$

where the $\vec{k}$ is the wave propagation vector, ω is the angular frequency, $\delta\vec{v}$ is the wave amplitude. Using spatial and temporal derivatives for such a wave form, $\nabla = i\vec{k}$ and $\partial/\partial t = -i\omega$, Eq. (1.63) becomes

$$(\omega^2 - (\vec{k} \cdot \vec{b})V_A^2)\delta\vec{v} + (i(\delta\vec{v} \cdot \vec{g}) + (\vec{k} \cdot \vec{b})(\delta\vec{v} \cdot \vec{b})V_A^2 - (C_s^2 + V_A^2)(\vec{k} \cdot \delta\vec{v}))\vec{k}$$
$$+i(\gamma - 1)(\vec{k} \cdot \delta\vec{v})\vec{g} + V_A^2(\vec{k} \cdot \delta\vec{v})(\vec{k}\vec{b}) \cdot \vec{b} = 0, \tag{1.65}$$

where $\vec{b} = \vec{B}/\,|B|$ is the unit vector along the magnetic field. Assuming that $z \ll H$,

the local dispersion relationship is obtained by setting the determinant of the scalar components equal to zero (Bel & Mein 1971; Bel & Leroy 1977),

$$
\begin{aligned}
(\omega^2 - (\vec{k} \cdot \vec{b})V_A^2)[\omega^4 &- \omega^2(i\gamma g k_z + (C_s^2 + V_A^2)k^2) + C_s^2 k^2 (\vec{k} \cdot \vec{b})^2 V_A^2 \\
&+ (\gamma - 1)g^2(k^2 - k_z^2) + i\gamma g b_z k^2 (\vec{k} \cdot \vec{b})V_A^2] = 0,
\end{aligned}
\tag{1.66}
$$

where $g = -g_z$, the subscript z denotes the z-components of the vector variables, i.e. $\vec{k}$, $\vec{b}$ and $\vec{g}$.

The first factor on the left-hand of Eq. (1.66) represents the dispersion relation of Alfvén waves. The second factor denotes the dispersion relation of the magnetoacoustic waves in the gravitationally stratified isothermal plasma.

Magnetoacoustic gravity cut-off frequency

From the second factor on the left-hand side of Eq. (1.66) (also see Eq. (6) in Bel & Mein 1971), the local dispersion of the magnetoacoustic gravity waves is,

$$
\begin{aligned}
\omega^4 &- [i\gamma g k_z + (C_s^2 + V_A^2)k^2]\omega^2 + C_s^2 k^2 (\vec{k} \cdot \vec{b})^2 V_A^2 \\
&+ (\gamma - 1)g^2(k^2 - k_z^2) + i\gamma g b_z k^2 (\vec{k} \cdot \vec{b})V_A^2 = 0.
\end{aligned}
\tag{1.67}
$$

This leads to the dispersion relation in Eq.(1) in Bel & Leroy (1977) (also note the typo therein):

$$
\begin{aligned}
\omega^4 &- [i\gamma g k_z + (C_s^2 + V_A^2)k_z^2]\omega^2 \\
&+ C_s^2 k_z^4 V_A^2 \cos^2\theta + i\gamma g k_z^3 V_A^2 \cos^2\theta = 0.
\end{aligned}
\tag{1.68}
$$

Here $k_\perp = 0$ is used in this step. Then we used the denotations: $l = V_A/C_s$, $m = V_A/C_s \cos\theta = l\cos\theta$, $k_z = \alpha + i\beta$ (Bel & Mein 1971; Bel & Leroy 1977), where α is the real wave number and β is the damping factor for positive values, or the growth factor for negative values, and the normalised dimensional variables: $\omega' = H\omega/C_s$, $Hk_z = x + iy$. After inserting these variables, the dispersion relation Eq. (1.68) is expressed as,

$$
\omega'^4 - [iHk_z + (1 + l^2)(Hk_z)^2]\omega'^2 + [(Hk_z)^4 + i(Hk_z)^3]m^2 = 0.
\tag{1.69}
$$

For a plane wave motion $\delta\vec{v} = \delta\vec{v}_0 \exp i[k_z z - \omega t]$ with $k_z = \alpha + i\beta$, it become a non-propagating wave, when the growth factor α approaches zero, therefore $Hk_z = iy$, and Eq. (1.69) becomes

$$
\omega'^4 + [y + (1 + l^2)y^2]\omega'^2 + (y^4 + y^3)m^2 = 0.
\tag{1.70}
$$

24

This equation agrees with Eq.(16) in Bel & Mein (1971). In the strong field (low plasma beta) approximation,

$$l \to \infty \tag{1.71}$$

$$m \to \infty \tag{1.72}$$

$$\frac{l}{m} = \frac{1}{\cos\theta}. \tag{1.73}$$

Now, Eq. (1.70) can be rewritten as,

$$y^2[(y+\frac{1}{2})^2 + \frac{\omega'^2}{\cos^2\theta} - \frac{1}{4}] = 0. \tag{1.74}$$

There is a solution for y in the real space, only if

$$\frac{\omega'^2}{\cos^2\theta} - \frac{1}{4} \leq 0.$$

Therefore the cut-off angular frequency is defined as $\omega'_c = \frac{1}{2}\cos\theta$. In dimensional variable, $\omega_c = 2\pi\nu_c = \frac{C_s}{2H}\cos\theta$. So the cut-off frequency in the strong field (low plasma beta) approximation, is given by

$$\nu_c = \nu_0 \cos\theta,$$

where $\nu_0 = C_s/4\pi H = \gamma g/4\pi C_s$.

1.3 Spectral analysis and significance tests

A time series of a physical quantity obtained in observations normally consists of a superposition of a signal $x(t_j)$ and a random noise $\sigma(t_j)$,

$$y(t_j) = x(t_j) + \sigma(t_j), \tag{1.75}$$

where t_j is the time of the j-th measurement. If the signal $x(t_j)$ consist of a number of quasi-periodic signals, spectral analysis is more illustrative and facilitates quantitative analysis. Usually, it is achieved by a Fourier transform (FT) or other FT-derived methods. In this section, I introduce the most commonly-used algorithm *Fast Fourier Transform* (FFT, Sec. 1.3.1) that performs a discrete Fourier transform of uniform data. Also, we overview the spectral analysis techniques used in this thesis. The *periodogram* (Sec. 1.3.2) technique and the *date-compensated Fourier transform* (Sec. 1.3.3) allow for spectral analysis of unevenly sampled data. Information about

time variation of spectral parameters of the analysed signal can be obtained with the *short-time* (windowed) *Fourier transform* (Sec. 1.3.4) and the *wavelet analysis* (Sec. 1.3.5). In Sec. 1.3.6, we discuss the significance tests for periodogram and other spectral analysis methods.

1.3.1 Fast Fourier Transform

Fast Fourier Transform is an efficient algorithm to perform discrete Fourier transform (DFT). DFT decomposes a time series into components over a range of discrete frequencies. Let y_j, where $j = 0, \cdots, N - 1$, be a series of complex numbers (the notation $y_j = y(t_j)$ is used alternatively in the following text). The DFT is defined as,

$$Y_k = \sum_{j=0}^{N-1} y_j e^{-i2\pi k \frac{j}{N}}, k = 0, \cdots, N - 1 \tag{1.76}$$

Direct DFT computation requires $\mathcal{O}\left(N^2\right)$ operations, while FFT computes the same results with only $\mathcal{O}\left(N \log N\right)$ operations. Hence FFT is much fast than DFT. The FFT is computed at sufficiently small frequency intervals, therefore the inverse FFT can be performed with negligible errors.

1.3.2 Periodogram

The periodogram is a commonly used spectral analysis technique to extract periodic components in unevenly-spaced data. Other spectral analysis techniques, i.e. FFT, wavelet, are not so efficient in handling this kind of data, as unevenly-spaced data usually generate spurious periods equal to time gaps and/or their harmonics in the FFT or wavelet techniques. However, the periodogram avoids such incapability. The periodogram is equivalent to the least-square fit with sinusoidal functions to the time series.

The reliability and efficiency of periodogram was studied in Scargle (1982), and here we follow that discussion. The periodogram $P_y(\omega)$ for an angular frequency component ω is defined as

$$P_y(\omega) = \frac{1}{2} \left\{ \frac{[\sum_j y_j \cos \omega(t_j - \tau)]^2}{\sum_j \cos^2 \omega(t_j - \tau)} + \frac{[\sum_j y_j \sin \omega(t_j - \tau)]^2}{\sum_j \sin^2 \omega(t_j - \tau)} \right\}, \tag{1.77}$$

where y_j is a physical observable at time sequence t_j. The parameter τ is defined as

$$\tan(2\omega\tau) = \left(\sum_j \sin 2\omega t_j\right) / \left(\sum_j \cos 2\omega t_j\right). \tag{1.78}$$

The quantity τ ensures the time-invariant properties of the power spectrum. $P_y(\omega)$ can be evaluated at any frequency ω. It is normally calculated at a set of M frequencies such that the $P_y(\omega_n)$ are independent random variables (Scargle 1982). In particular, the frequencies may coincide with the natural frequencies used in the Fourier analysis.

1.3.3   Date-compensated Fourier transform

Date-compensated Fourier transform is *de facto* superior than the periodogram, especially in estimating the amplitudes of spectral components, however it is less frequently used due to the lack of a reliable significance test. The periodogram mismeasures the amplitudes severely when the signal period and the data gaps are close in value. After subtracting the signal component, the residuals have a large value other than zero, and the periodic component still shows up as a significant peak (Foster 1995).

In common FT-derived methods, the average of the time series is removed prior to spectral analysis. Then the time series is decomposed into a two-dimensional function subspace consisting of sine and cosine. Ferraz-Mello (1981) considered projecting the data into a three-dimensional function subspace: sine, cosine and $\vec{1}$, which means that every trial frequency component ω still shares a non-zero residue. For a trial frequency ω, three basis functions are constructed,

$$H_0(t_j) = 1, \tag{1.79}$$

$$H_1(t_j) = \cos \omega t_j, \tag{1.80}$$

$$H_2(t_j) = \sin \omega t_j. \tag{1.81}$$

These functions are orthonormalised by the Gram-Schmidt formulae (Ferraz-Mello 1981):

$$h_0 = a_0 H_0, \tag{1.82}$$

$$h_1 = a_0 H_1 - a_1 h_0 < h_0, H_1 >, \tag{1.83}$$

$$h_2 = a_2 H_2 - a_2 h_0 < h_0, H_2 > -a_2 h_1 < h_1, H_2 > . \tag{1.84}$$

The angle bracket denotes the inner product $< y_1, y_2 >= \sum_0^{N-1} y_1(t_j)y_2(t_j)$. The coefficients a_0, a_1 and a_2 are determined in such a way that

$$< h_0, h_0 >=< h_1, h_1 >=< h_2, h_2 > . \tag{1.85}$$

The date-compensated discrete Fourier transform (DCDFT) is computed as

$$P(\omega) = F(\omega)F^*(\omega) \tag{1.86}$$
$$F(\omega) = < y, h_1 + ih_2 > /a_0\sqrt{2}, \tag{1.87}$$

where $(*)$ denotes complex conjugate, $i = \sqrt{-1}$ is the imaginary unit.

The DCDFT method measures the spectral amplitude with good accuracy. A harmonic filter was designed to remove certain periodic components in the time series in the temporal domain. This method is in contrast, but superior, to traditional filtering in the spectral domain. A harmonic signal at a certain frequency ω_0 is calculated with the DCDFT method and is subtracted from the original signal,

$$\hat{y}(t_j) = y(t_j) - [d_0 + d_1 \cos \omega_0 t_j + d_2 \sin \omega_0 t_j]. \tag{1.88}$$

The coefficients d_0, d_1 and d_2 are evaluated with the DCDFT method (Ferraz-Mello 1981).

1.3.4 Windowed Fourier transform

Windowed Fourier transform (WFT) is a Fourier transform performed at local sections of a time series, therefore the local spectra of the frequency, amplitude, phase and their changes over time are obtained. It is equivalent to multiplying a window function over the signal in the time domain. The window function is only non-zero over a certain range in time and is padded with zero over most of time. Usually the non-zero part is moving (sliding) over time, therefore the dynamical spectra are obtained. Mathematically, windowed Fourier transform is expressed as,

$$Y_{k,m} = \sum_{j=0}^{N-1} y_j w_{j-m} e^{-i2\pi k \frac{j}{N}}, k = 0, \cdots, N-1 \tag{1.89}$$

$$= \{Y_k \star W_k\}(m), \tag{1.90}$$

where w_j and W_k are the window function and its Fourier transform, respectively, and $(\star)$ in Eq. (1.90) denotes the convolution operation. There are a number of commonly used window functions, i.e. a rectangle window, cosine bell window,

28

Hamming window, Hanning window (Harris 1978; Nuttall 1981). The window size determines the temporal and spectral resolution. There is a trade-off effect between them: a small window size generates a dynamic spectrum with a good temporal resolution but a coarse spectral resolution; while a dynamic spectrum obtained with a sufficiently large window size has a good spectral resolution but a coarse temporal resolution. A wide spectra with both low and high frequency components may require different spectral and temporal resolution. This leads to the creation of wavelet transform, discussed in Sec. 1.3.5.

1.3.5   Wavelet analysis

Similarly to WFT, the wavelet transform is exploited to analyse the variability of series and gives the time-dependent power spectra (e.g. Daubechies 1990). It is defined as the convolution of the time series y_j with a scaled and translated version of a mother function $\Psi_0(\eta)$. The wavelet function $\Psi_0(\eta)$ depends on a non-dimensional time parameter η (Torrence & Compo 1998):

$$W_h(s) = \sum_{j=0}^{N-1} y_j \Psi^* \left[\frac{(j-h)\delta t}{s} \right],$$ (1.91)

where δt is the uniform time interval between two adjacent data points, s is the scale (width) of the wavelet, it is related to the Fourier period. Ψ is the normalised version of Ψ_0 (see Torrence & Compo 1998, for details). It must have zero mean and be localised in both time and frequency spaces to be admissible as a wavelet function (Farge 1992).

The Morlet wavelet is one of the most commonly used mother function to study oscillatory processes. It consists of a plane wave function modulated by a Gaussian profile (e.g. Farge 1992):

$$\Psi_0(\eta) = \pi^{-1/4} e^{i\omega_0 \eta} e^{-\eta^2/2},$$ (1.92)

where $\omega_0 = 6$ is the non-dimensional frequency that satisfies the admissibility condition (Farge 1992), however using larger ω_0 was found to improve the spectral resolution (De Moortel & Hood 2000).

Wavelet transform is usually evaluated in the Fourier space, benefiting from the efficient FFT computation. The Fourier transform of the mother function $\Psi(t/s)$ is denoted as $\hat{\Psi}(s\omega)$. According to the convolution theorem, the wavelet transform

29

is calculated as the product of the Fourier transform:

$$W_h(s) = \sum_{n=0}^{N-1} Y_n \hat{\Psi}^*(s\omega_n)e^{i\omega_n h\delta t}, \tag{1.93}$$

where Y_n is the Fourier transform of the time series. The angular frequency is defined as,

$$\omega_n = \begin{cases} 2\pi n/N\delta t, & k \leq N/2 \\ -2\pi n/N\delta t, & k \geq N/2. \end{cases} \tag{1.94}$$

Under the normalisation condition, at each scale s, the Fourier transform of the mother function has to fulfil

$$\sum_{n=0}^{N-1} |\hat{\Psi}(s\omega_n)|^2 = N. \tag{1.95}$$

If the wavelet spectrum is averaged over time, the global wavelet spectrum is obtained,

$$W_g^2(s) = \frac{1}{N} \sum_{h=0}^{N-1} |W_h(s)|^2. \tag{1.96}$$

It can also be approached by smoothing the Fourier spectrum (Torrence & Compo 1998). This is another way of estimating the spectrum of a time series.

1.3.6   Significance tests

Statistical significance is a statistical assessment of whether a peak in the spectrum represents a realistic periodic pattern or just a chance generated by noise. The chance, usually a small fractional probability, is called false alarm probability (FAP) or p-value. To estimate the significance of the obtained spectrum, a number of reliable significance tests were proposed. Usually the variable in the analysed series is assumed to follow a certain statistical distribution. The number of independent variables is called the degree of freedom (DOF). For example, the popular method to estimate FAP in the periodogram is based upon the assumption that the power amplitude follows an exponential distribution (cf. Sec. 1.3.2 and Scargle 1982; Horne & Baliunas 1986). In the wavelet technique, the local wavelet power is often assumed to follow the χ_2^2-distribution with two DOF (see Sec. 1.3.5 and Torrence & Compo 1998). The methods based on the assumption of a certain statistical distribution are called parametric methods. A non-parametric statistical method, called Fisher's randomisation test (also known as the permutation test or exact test), was proposed

by Fisher et al. (1970). It was applied successfully to Phase-Dispersion Minimisation (PDM, Linnell Nemec & Nemec 1985a) and periodograms (Yuan et al. 2011).

Noise analysis in Fourier spectrum

In Fourier analysis, the noise level is a good indicator of the significance level of the spectrum. The noise level of a Fourier spectrum of a time series can be modelled either as white noise or red noise. A simple model to estimate the red noise is given as,

$$y_j = \alpha y_{j-1} + z_j \tag{1.97}$$

where α is assumed to be the lag-1 auto-correlation coefficient, z_n is a random value (white noise) that follows a Gaussian distribution. y_0 is set to zero. $\alpha = 0$ gives the case of white noise. According to Gilman et al. (1963); Torrence & Compo (1998), the discrete Fourier power spectrum should be normalised as $N|Y_k|^2/2\sigma^2$, where Y_k is the Fourier complex amplitude, σ^2 is the total variance of the time series y_j. After normalisation, the corresponding red noise spectrum is estimated as

$$P_k = \frac{1 - \alpha^2}{1 + \alpha^2 - 2\alpha \cos(2\pi k/N)} \tag{1.98}$$

where $k = 0, \cdots, N/2$ is the frequency index.

False alarm probability in periodogram

To estimate the FAP of a periodogram, the magnitude $P_y(\omega_n)$ is normalised with the total variance of the signal $\sigma_y^2 = \mathrm{Var}\{y_j\}$ (Horne & Baliunas 1986). In this case, the normalised magnitude $P_N(\omega_n) = P_y(\omega_n)/\sigma_y^2$ follows the exponential distribution e^{-z}, where z is the power level at ω_n, if a Gaussian noise is assumed for $\sigma(t_j)$ (Scargle 1982).

Let $Z = \max P_N(\omega_n)$, the probability that Z is above a certain power level z is

$$Pr\{Z > z\} = 1 - [1 - e^{-z}]^M, \tag{1.99}$$

where the quantity M is the number of independent frequencies.

A random noise may generate a false peak above the maximum level z_0 in the spectrum at a small fractional probability p_0. This defines the false alarm probability (FAP) that the detection of the maximum peak is false. The detection threshold is, according to Eq. (1.99) (Scargle 1982),

$$z_0 = -\ln\left[1 - (1 - p_0)^{1/M}\right]. \tag{1.100}$$

The FAP (p_0) is usually a small fractional number, e.g. $p_0 = 0.01, 0.05$, therefore,

$$z_0 \simeq \ln(M/p_0) \qquad (1.101)$$

$$= 4.6 + \ln(M) \ \{\text{for } p_0 = 0.01\}. \qquad (1.102)$$

If the maximum peak level is above z_0, the detection is reliable with a significance level p_0 (or a confidence level of $1 - p_0$). Otherwise, the detection is not significant under the significance level p_0. The simple estimation of the significance level is an important advantage of periodogram: this is the reason why it is broadly applied in solar physics.

Randomisation test for periodogram

In the following text, I consider how the randomisation test is applied to the periodogram. For a time series $y_j = x_j + \sigma_j$, the periodogram always has a peak (or a maximum value) in the spectrum. A null hypothesis is suggested that x_j is a pure random noise with no periodicity,

$$H_0 : x(t_j) = \text{constant for all } t_j \qquad (1.103)$$

against the alternative that the time series x_j is a harmonic signal with a known period T_0,

$$H_1 : x(t_j) = x(t_j \pm kT_0) \text{ for all } t_j \text{ and } k = 0, 1, 2, \cdots. \qquad (1.104)$$

The maximum spectral amplitude P_m, irrespective of its location in the spectrum, is the measurable to evaluate the significance level. For the original time series $y_j = y_0, y_1, y_2 \cdots, y_{N-1}$, the maximum peak in the periodogram is denoted as $P_m^{y_j}$. A random permutation (re-ordering) of the time series is obtained: $y_r = y_{r_0}, y_{r_1}, y_{r_2}, \cdots, y_{r_{N-1}}$, and $P_m^{y_r}$ is the corresponding dominant peak in the periodogram of y_r. Notably the peaks $P_m^{y_j}$ and $P_m^{y_r}$ may locate at different frequencies. If y_j contains a periodic component, a permutation normally disrupts the phase and self-correlation of the time series, therefore the dominant peak $P_m^{y_r}$ is usually smaller than $P_m^{y_j}$. In rare cases, one obtains $P_m^{y_r} > P_m^{y_j}$, which means that a randomisation generates a higher peak in the modified spectrum than the original spectrum. The number of such cases R out of M permutations determines the significance level,

$$p = R/M. \qquad (1.105)$$

Ideally a sufficient number of permutations has to be performed in order to get a reliable result. In a series with N elements, the number of possible permutations is $N!$. In practical applications, $M \approx 100$ is sufficient. The uncertainty associated with p is (Linnell Nemec & Nemec 1985a; Yuan et al. 2011)

$$\delta p = \left[\frac{p(1-p)}{M} \right]^{1/2} . \tag{1.106}$$

The maximum uncertainty is $0.5M^{-1/2}$, for $M = 1000$, the maximum error is 0.016, this also defines the detection limit. Normally for those $p < 0.01$, the detection limit $p = 0.01$ is assumed as the significance interval.

The aforementioned procedure only applies to the maximum peak in a spectrum. To perform significance test for the secondary peaks, the maximum peak has to be removed. This can be done with spectral filtering (Inglis & Nakariakov 2009) or temporal filtering (Ferraz-Mello 1981; Yuan et al. 2011). Removing a harmonic signal from the time series is more robust in the time domain (cf. Sec. 1.3.3). After removing the dominant peak, the above procedure can be repeated iteratively to the residual spectrum and assess the significance levels of the secondary peaks (Yuan et al. 2011).

Noise analysis in wavelet spectrum

The noise of a wavelet spectrum was found to be more close to red noise and was shown to be identical to the Fourier power spectrum by Monte-Carlo simulation (Torrence & Compo 1998). Therefore, the noise of a wavelet spectrum can be approximated with FFT noise estimation as in Eq. (1.98), but it should be done within the local section of the time series.

To justify reliable detections of the oscillatory signals, one has to perform a significant test, say, at a significance level(or FAP) of 0.05 (or a confidence level of 0.95). This defines a probability $p = 0.05$ that a certain peak detection is false in the spectrum. It is equivalent to the false alarm probability in the periodogram. A null hypothesis has to be performed by assuming a reasonable variable distribution. If the time series y_j is a normally distributed variable, then the real and imaginary parts of its Fourier transform Y_k also follow normal distribution (Chatfield 2003). Therefore the normalised Fourier spectrum $N|Y_k|^2/2\sigma^2$ is chi-square distributed with two degree of freedom DOF $= 2$, denoted with χ_2^2, (Jenkins & Watts 1969; Torrence & Compo 1998). The local wavelet spectrum is also assumed to follow the mean Fourier spectrum, therefore it also follows χ_2^2 distribution and can be formulated as

(Torrence & Compo 1998),

$$\frac{|W_h(s)|^2}{\sigma^2} = \frac{1}{2} P_k \chi_2^2 \tag{1.107}$$

at time index h and scale s. The value P_k is given in Eq. (1.98), and χ_2^2 is the value at a certain significance level. For example for $p = 0.05$, $\chi_2^2 = 5.991$. Repeating this process at each scale s, the contours of a significance level are constructed.

At the edge of a wavelet spectrum, a finite time series gives discontinuity. It is usually padded with sufficient zeros to avoid complexity in computation, therefore the spectrum at the edge become unrealistic and unreliable. The boundary of this region is called the cone of influence (COI, Torrence & Compo 1998). The COI increases with the scale, as the scale gets larger, more zeros are required to pad the missing data.
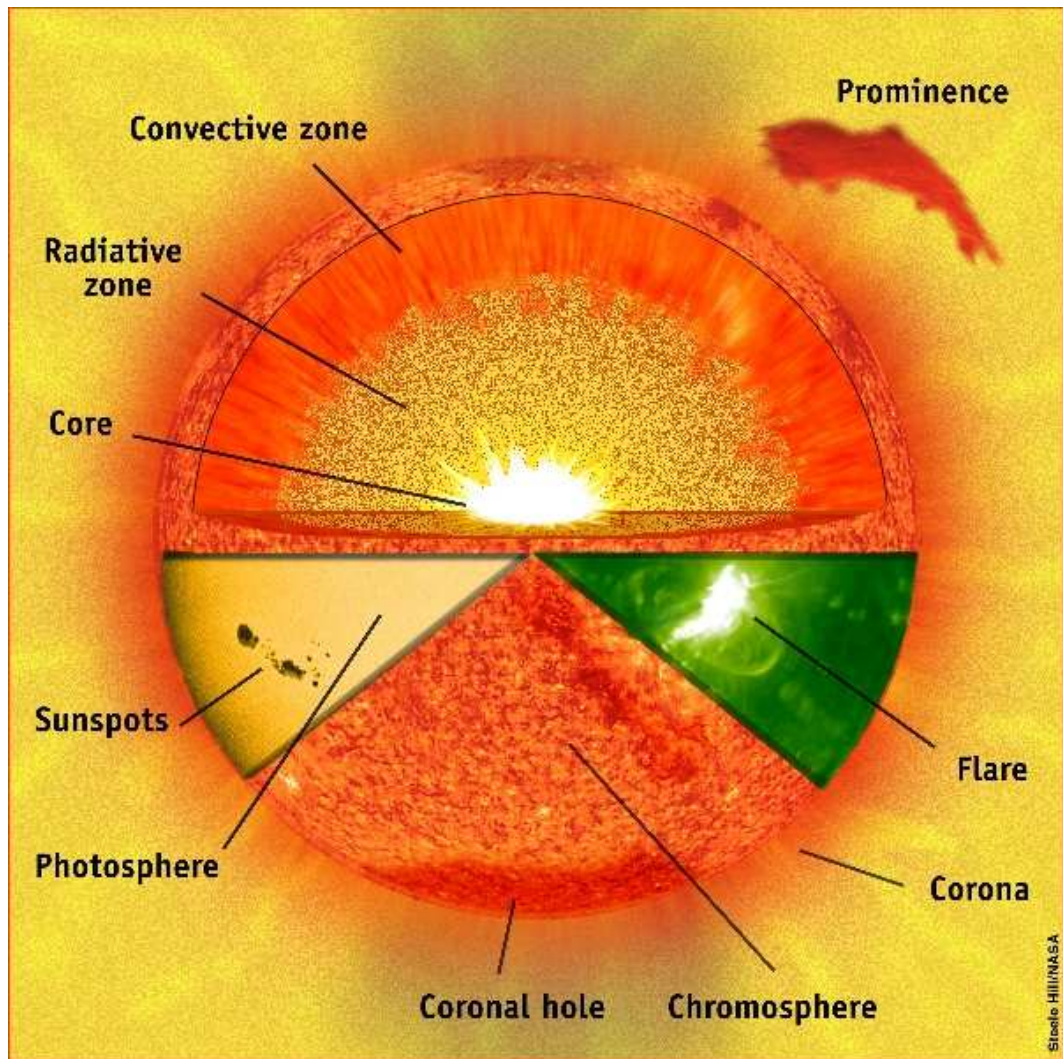
Figure 1.1: Schematic sketch of the solar interior, the solar atmosphere and the inner corona. Courtesy of the SOHO project (ESA and NASA).
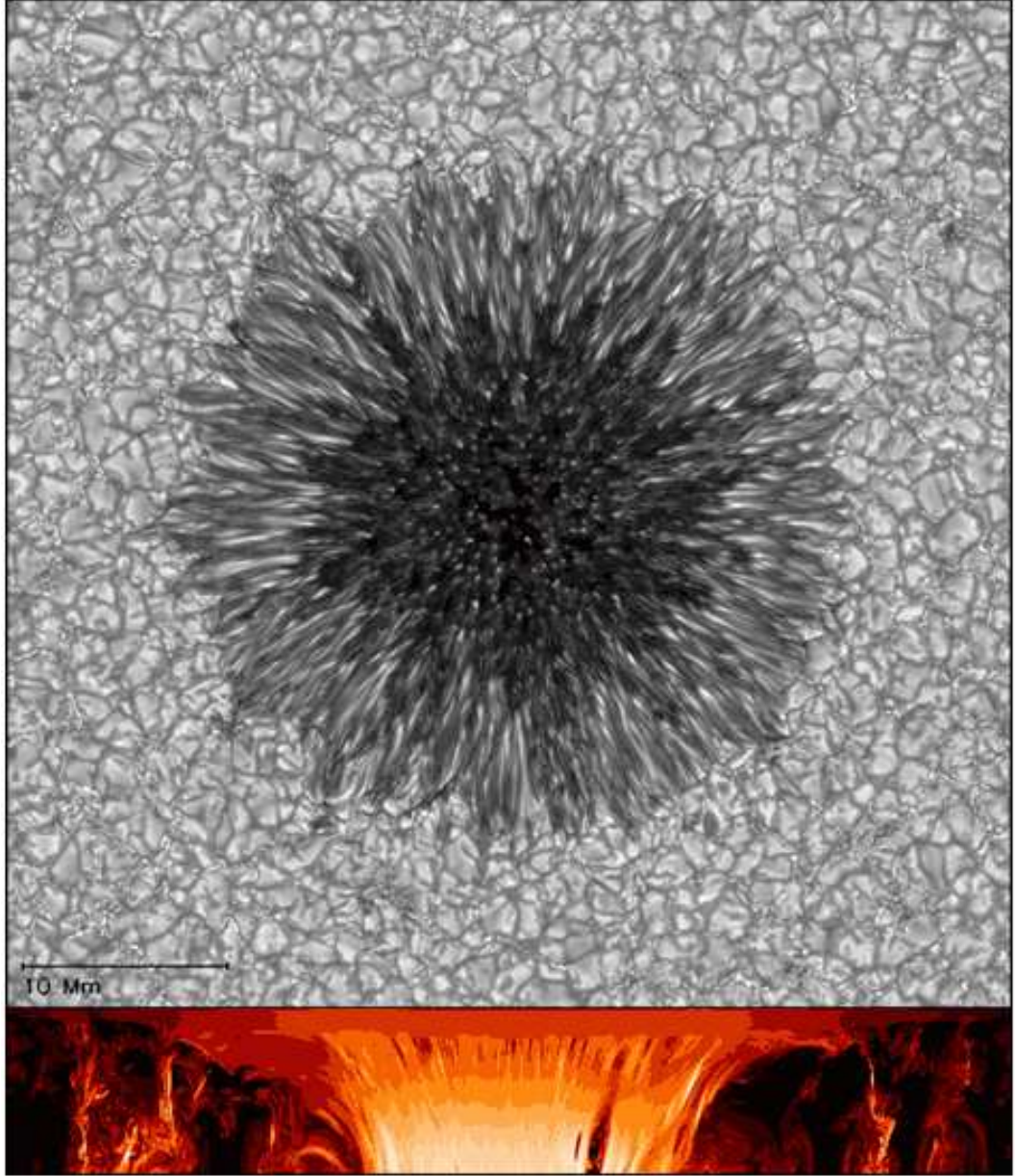
Figure 1.2: Snapshot of a sunspot from radiative MHD simulations (Rempel et al. 2009). Top: surface brightness map of the sunspot and the surrounding granulation. Bottom: A vertical cut through the mid-plane of the sunspot. Colour denotes the field strength, brighter colour denotes stronger field strength.
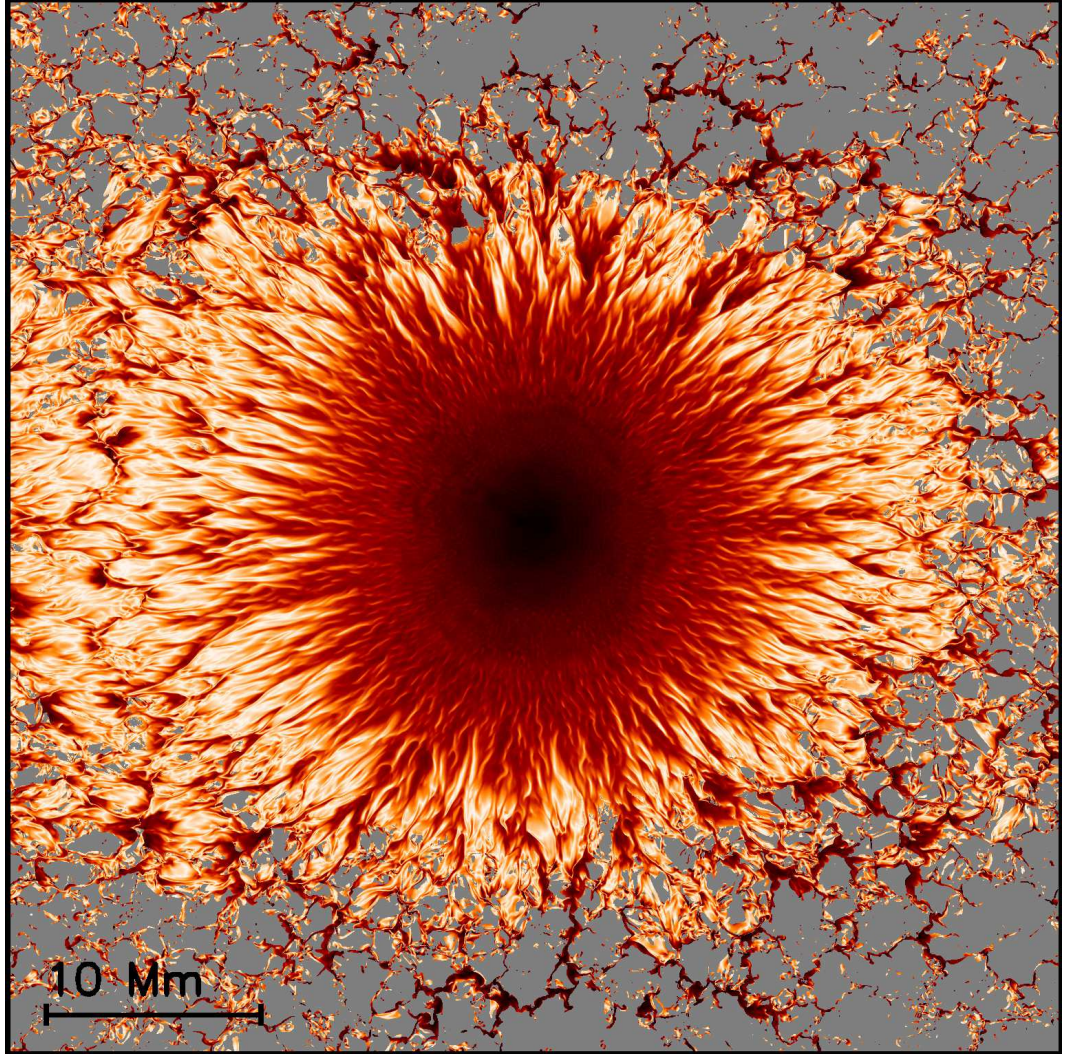
Figure 1.3: The inclination angle of the magnetic field in the photosphere (the same sunspot as in Fig. 1.2). The gray colour indicates regions with field strength $< 200\,$G. Source: High Altitude Observatory.
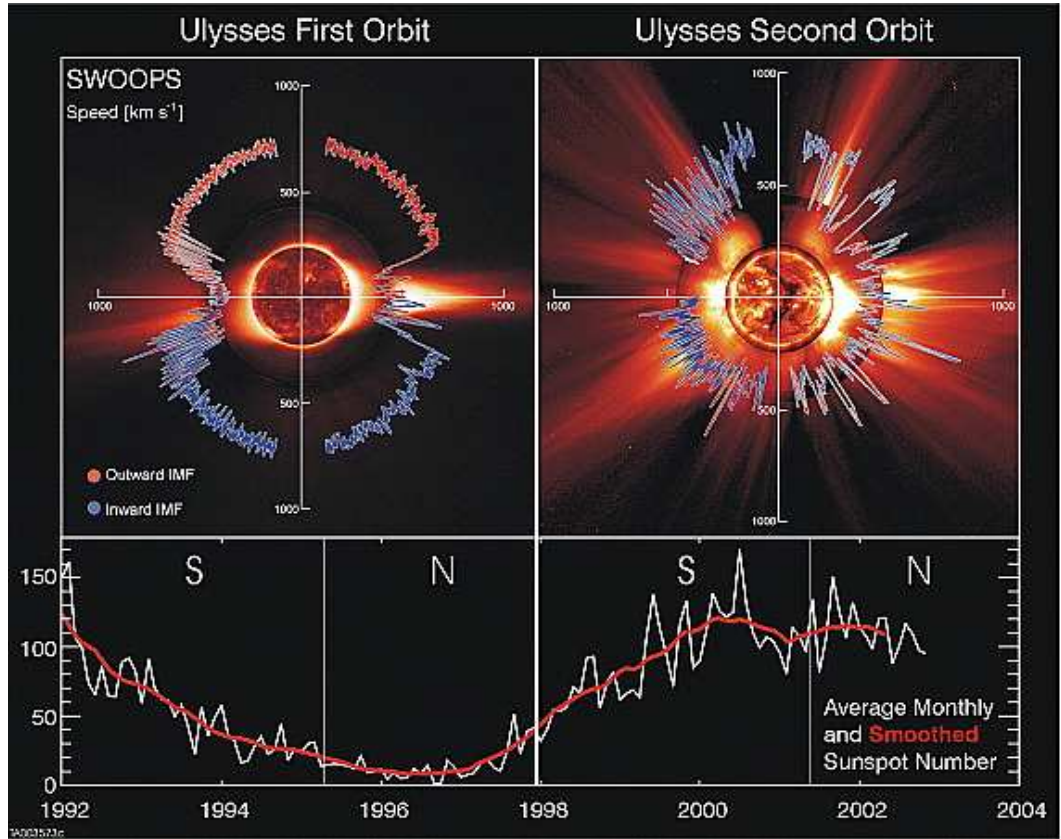
Figure 1.4: The speed of the solar wind as a function of the latitude measured by Ulysses/SWOOPS during its first orbit near a solar minimum (left panel) and its second orbit near a solar maximum (right panel). The polar plots are overlaid with images from SOHO/LASCO and EIT, and the Mauna Loa K-coronameter (McComas et al. 2003).
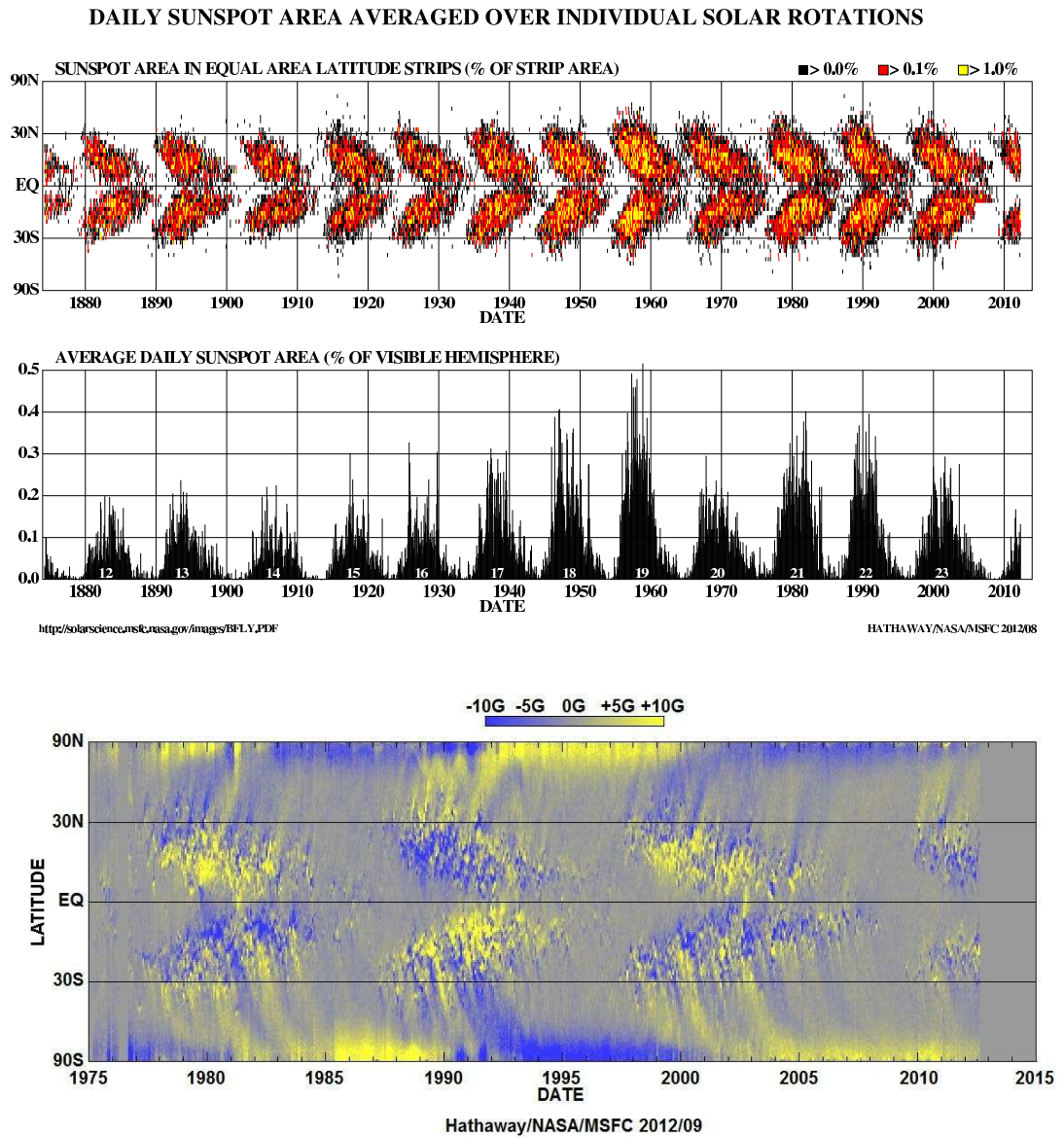
Figure 1.5: Top: the butterfly diagram: evolution of sunspot latitude locations over time; the colour index denotes the area occupied by the sunspots. Middle: the average sunspot area in percents of the visible hemisphere and its variation over solar cycles since May 1874. Bottom: the magnetic butterfly diagram showing the evolution of the line-of-sight magnetic field over the solar cycles 21–24. Courtesy of the Marshall Space Flight Centre/NASA.
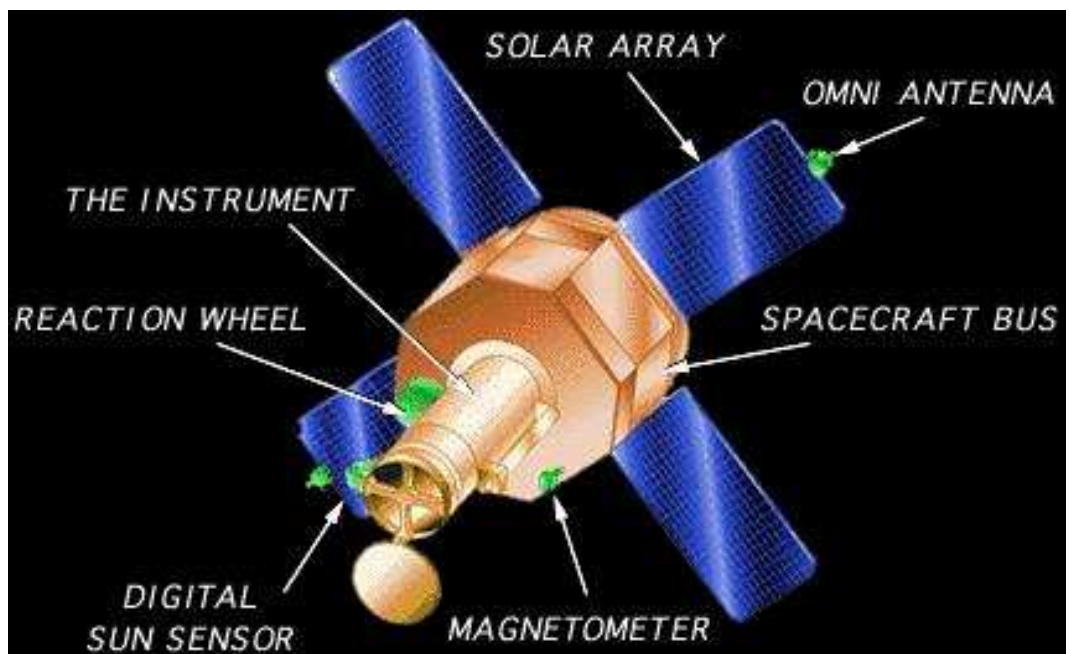
Figure 1.6: Transition Region and Coronal Explorer (TRACE) satellite. Courtesy of NASA.
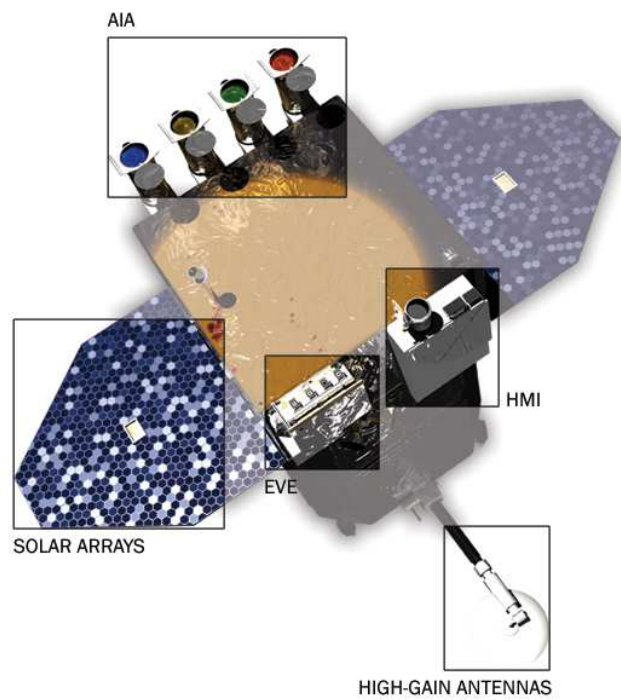
Figure 1.7: Top: the Solar Dynamics Observatory (SDO). Bottom: the Atmospheric Imaging Assembly (AIA), the Helioseismic and Magnetic Imager (HMI). Courtesy of NASA.
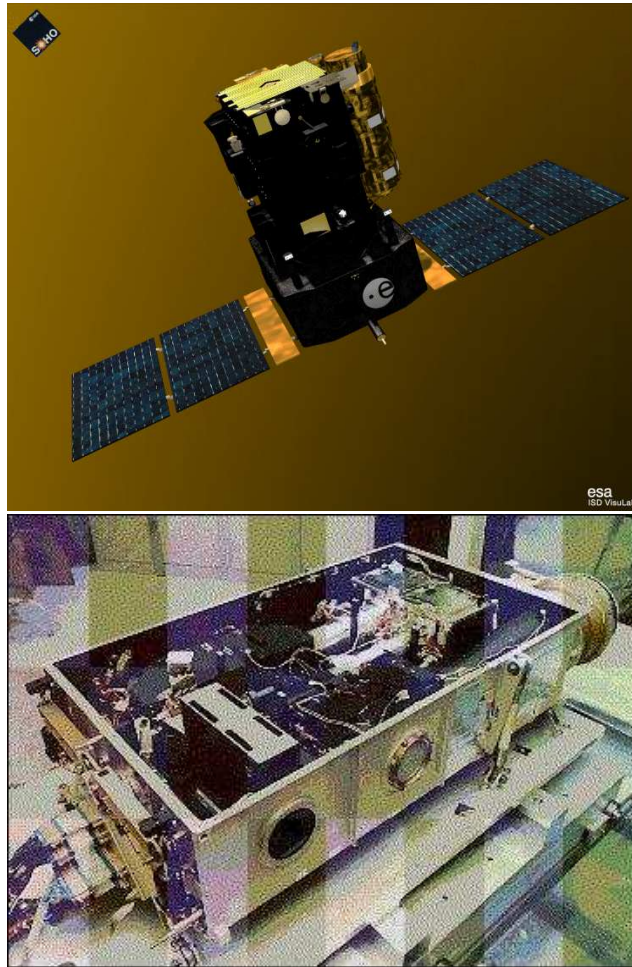
Figure 1.8: Top: the Solar and Heliospheric Observatory (SOHO). Bottom: the Michelson Doppler Imager (MDI). Courtesy of ESA and NASA.

Figure 1.9: The site of the Nobeyama Radioheliograph (NoRH). Courtesy of NAOJ.
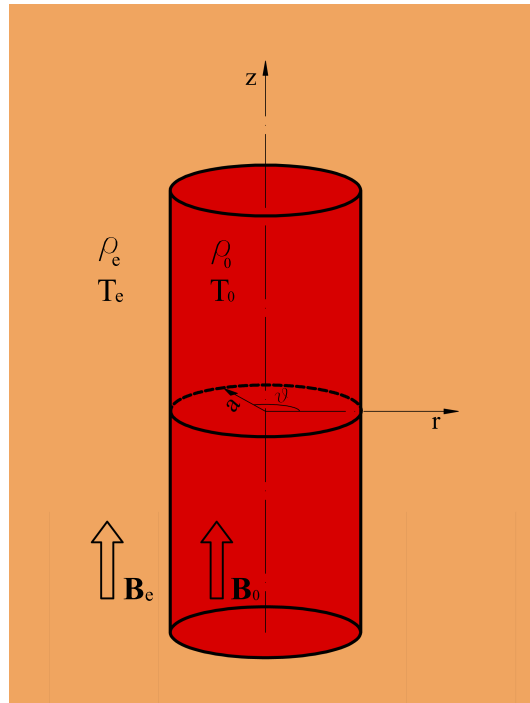
Figure 1.10: The ideal plasma cylinder model

Chapter 2

Instrumental artifacts and noise analysis

Instrumental artifacts appear in a number of instruments, their existence may lead to erroneous interpretations. In this chapter, the instrumental artifacts in the imaging data sets, obtained by recording the plasma emission intensity at a certain wavelength, are presented by taking specific examples in TRACE and SDO/AIA. The TRACE image intensity responds to the CCD temperature, which is a function of the incoming EUV radiation. The TRACE satellite orbits the Earth with a 96 min period, therefore the average image intensity also bears a periodicity at 96 min. As the EUV radiation along the orbit is inhomogeneous, other harmonics of the 96 min periodicy also appears in the TRACE images (cf. Sec. 2.1). In processing AIA image data cubes, if an object is tracked for sufficiently long time (~30 min), it requires to remove the solar differential rotation (de-rotation) by harshly cropping lines of discrete pixels. This procedure leads to a periodic jittering in the images (cf. Sec. 2.2). The periodicity can ride in the range of 3– and 5–min, which is close to the seismic periodicites observed in sunspots, quiet Sun chromosphere, propagating longitudinal waves in the coronal structures and transverse oscillations of the coronal loops. Periodic artificial periodicities in the data should be distinguished from the physical periodicities, it requires a deep understanding of the possible manifestation of the artificial signals in the data.

2.1 TRACE orbital artifact

TRACE orbits in a polar sun-synchronous orbit, roughly following the solar terminator (twilight zone). The orbital period is ~96 min (~0.17 mHz). Because of the orbital

44

motion, the EUV flux incident on the CCD detector changes periodically, therefore the CCD temperature is modulated and varies with the orbital period (Fig. 2.3, top row). The changes in temperature introduce variability to the pedestal value of the observed intensity and the readout noise (Aschwanden et al. 2000). It should be accounted when studying the long-period intensity oscillations.

Consider an illustrative example that shows the appearance of the orbital artifact in the data. The spectrum of the temporal variation of the pixel count averaged over the ROI in 171 Å data (Fig. 2.1(a)) in 1998-07-03 00:47 - 12:00 UT (Fig. 2.3, middle row) revealed pronounced peaks at the frequency corresponding to the orbital period $0.17\,\text{mHz}$ (96 min) and its higher harmonics $0.35\,\text{mHz}$ (48 min), $0.52\,\text{mHz}$ (32 min), $0.69\,\text{mHz}$ (24 min). The same periodicities were detected in a rather quiet region (Fig. 2.3, bottom row), chosen off the ROI region (Fig. 2.1(a)). The same results are found in both 171 Å and 195 Å data. The presence of the higher harmonics of the orbital period is connected with the nonlinear dependence of the image intensity on the CCD temperature (Fig. 2.3, top row).

The variation of the CCD temperature is periodic. The anharmonicity of the signal leads to the appearance of higher harmonics in the spectrum. Assume that the CCD temperature consists of an average term and a small modulation term: $T = \langle T \rangle + \delta T \cos\left(\frac{2\pi t}{P} + \phi\right)$, where T is the CCD temperature, it is a funciton of time, $\langle T \rangle$ is the average CCD temperature, t denotes the time, $p = 96\,\text{min}$ is the orbital period, while ϕ is a random phase. We expand the average intensity $F(T)$ of the images into the Taylor series and re-arrange it by trigonometric operations:

$$F(T) = \qquad\qquad F(\langle T \rangle) + \frac{dF}{dT}\delta T + \frac{d^2 F}{2! dT^2}(\delta T)^2 + \ldots \qquad (2.1)$$

$$= \qquad a_0 + a_1 \cos\left(\frac{2\pi t}{p} + \phi\right) + a_2 \cos^2\left(\frac{2\pi t}{p} + \phi\right) + \ldots \qquad (2.2)$$

$$= \qquad b_0 + b_1 \cos\left(\frac{2\pi t}{p} + \phi_1\right) + b_2 \cos\left(\frac{2\pi t}{p/2} + \phi_2\right) \qquad (2.3)$$

where a_0, a_1 and a_2 are the zeroth, first and second Taylor coefficients, while b_0, b_1 and b_2 are the coefficients after trigonometric operations. This explains the presence of the artificial short-periodicities (48 min, 32 min, 24 min, more specifically, the orbiltal period divided by an integer) in the TRACE signals. Here the harmonic periods affect the image intensities, as the telescope orbits around the Earth. It is due to the non-linearity of the orbital environment, the detection efficiency and the telescope system. In particular, these artificial periods are in the same range as long-period oscillations in sunspot atmospheres, and hence it must be taken into account in the analysis. A similar orbital effect applies to other space missions operating at

the sun-synchronous orbits as well, e.g. Yohkoh, Hinode and CORONAS-Photon. It varies between instruments and has to be studied systematically to avoid misleading results.

The non-linear orbital artifact has to be removed before analysing other periods that are close to the orbital period or its harmonics. One of the ways to iteratively remove the orbital period is to perform harmonic filtering in the time domain (see Sec. 1.3.3 for the detailed description of this procedure). The harmonic filtering should be applied to the higher harmonics as well, until they become negligible compared to other periodicities (Yuan et al. 2011).

2.2 AIA image de-rotation artifact

SDO/AIA images the whole solar disk over $4k \times 4k$ pixels, hence, the ROI is subject to solar differential rotation. The rotation rate is observed to be fastest at the solar equator and become slower at higher latitude. The differential rotation rate is formulated as (see Howard et al. 1990, and reference therein),

$$\omega(\phi) = A + B \sin^2(\phi) + C \sin^4(\phi), \tag{2.4}$$

where ω is the angular velocity in degrees per day, ϕ is the solar latitude, A, B, and C are constants that are determined by observations. The constants A, B and C are slightly different for different measuring techniques and reference proxy (magnetic features, sunspot etc.), and they vary with the time interval (solar cycle) studied. The most up-to-date set of values is, based on tracking small bright coronal structures (Wöhl et al. 2010),

$$A = 14.449 \pm 0.006 \, \text{deg/day}, \tag{2.5}$$

$$B = -2.54 \pm 0.06 \, \text{deg/day}, \tag{2.6}$$

$$C = -0.77 \pm 0.09 \, \text{deg/day}. \tag{2.7}$$

If we transform the image coordinates into a co-rotating coordinate system with the solar differential rotation, the relative velocity of an AIA image pixels is

$$v_{\text{rot}} = \frac{2\pi R_\odot}{T_{\text{syn}}} = 1.8557 \, \text{km/s} = 0.00256 \, \text{arcsec/s} = 0.00427 \, \text{pixel/s} \tag{2.8}$$

with $R_\odot = 696,000 \, \text{km}$ and a synodic rotation period $T_{\text{syn}} = 27.753 \, \text{days}$. Notably the traditionally chosen T_{syn} corresponds to the differential rotation at 26° latitude. At the solar equator, the image pixels move at a relatively higher velocity (note: a

rigid rotation motion is assumed in this estimation),

$$v_{\rm rot}^0 = v_{\rm rot}/\cos(26°) = 0.00475\,{\rm pixel/s} \tag{2.9}$$

It requires $P_0 = 210.7\,{\rm s}$ (~3.5 min) to accumulate one pixel, this is equivalent to about 18 consecutive frames at a 12 s cadence. P_0 is the artificial period, that may be introduced into the intensity images, as one performs discrete cropping to the AIA images. However, as one crop the images at a higher latitude ϕ, the artificial period becomes $P = P_0/\cos\phi$. This effect is also subjected to longitudal projection, the artificial period is increased to $P = P_0/\cos\phi\cos\lambda$ at the longitude λ.

The above analysis assumes that the operations are based on vertical cropping or interpolation. However it is not usually the case, if one interpolates the image with a certain angle θ relative to the horizontal direction in the image coordinate, the artificial period is further modified as $P = P_0/(\cos\phi\cos\lambda\cos\theta)$. The artificial perturbation is more apparent if a pixel have very sharp discrimination with its ambient pixels, e.g. a bright coronal loop in the dark background, or the edge of a coronal hole. If one takes the time series of a bright pixel perturbed by a dark background, and that of a dark pixel perturbed by a bright background in the same image set, the phase difference would be exactly 180 degrees.

To illustrate this effect, we took an example in an AIA 171 Å data of active region AR 11330 observed on 27 Oct 2011 (cf. Fig. 2.4). A 12-hour data set from 04:00 - 16:00 UT 27 Oct 2011 was prepared at AIA level-1.5 data. A transient loop, as labelled in Fig. 2.4, moved towards the east and interacted with the fan-structure, then it started to fade out and diminished at around 06:00 UT. This loop is surrounded by a dark background structure (Note that the logrithmatic scale renders this feature less apparent visually), so it is a good target for this study. We took a slice along the loop, the spectral analysis of one macro-pixel (3×3 pixels) is illustrated in Fig. 2.5. The time series of the average intensity of the macro-pixel is detrended by removing the running average of 50 data points, equivalent to 600 s temporal averaging. The top row in Fig. 2.5 displays the detrended time series and its histogram, the second row shows the Morlet wavelet analysis and global wavelet. The COI is cross-hatched in purple. In the bottom row in Fig. 2.5, the windowed FFT and periodogram are presented, the Gaussian window of 60–min in size is chosen for this study, the edge of the windowed FFT spectrum was cross-hatched to disregard the region where zero-padding was implemented to obtain the spectrum.

In the global wavelet and periodogram spectrum in Fig. 2.5, the well-known 3–min oscillation is observed as quasi-periodic EUV disturbance. The spectral peaks

clusters around 180 s, and show a cut-off period at around 200s (see detailed study in Yuan & Nakariakov 2012, and reference therein). Further above the peaks generated by known physical processes, a significant peak arise at ~390 s (6.5–min). If we look at the temporal variation of the period, it is only localised between ~30 min to ~130 min starting from 04:00 UT, it matches the time when the loop become visible and fadeout, while the 3–min oscillation is persistently observable as wave trains. The amplitude of the 3–min oscillation is less than 5% of the total intensity in agreement with previous studies (De Moortel et al. 2002c,a; De Moortel 2009; Yuan & Nakariakov 2012), while that of the 6.5–min oscillation reaches more than 10% of the background intensity.

In Fig. 2.6, the spectral analysis of the average intensity of the whole loop is presented. It clearly shows that the 3–min oscillation is smoothed out. As 3–min oscillation displays phase variation along the loop, positive and negative phases cancel each other during averaging, so it completely disappeared. The only periodic component left is the 6.5–min periodicity. It indicates that it is a global effect with high spatial coherency along the loop. Therefore, it is most likely an image artifact, instead of a physical process. The time-distance plot shows vertical ridges, namely, the propagating speed is infinity, or cannot be resolved within AIA spatial and temporal limit. A further clue comes from the phase of the 6.5–min periodicity. The phase difference between different pixels along the loop shows zero phase difference, while a macro-pixel 3×3 pixels selected from a dark region with bright border shows a phase difference of exactly 180° compared with those from this loop. So we conclude that the 6.5–min period is an artifact from discrete image cropping, as explain theoretically in the above text.

To remove the de-rotation artifact due to discrete image cropping, one has to trade out with the accuracy of the image flux. Since SDO/AIA observe the whole solar disk, the alignment is much better than previous missions that record partial image of the solar disk (e.g. TRACE) and those missions with a coarse spatial resolution (e.g. STEREO, EIT). If one is more interested in the relative image flux, or the absolute value won't affect the result, then it is a better option to interpolate (spline interpolation is quite acceptable) the image into a smoothly co-moving frame with the solar differential rotation. After performing this step, the interpolation error and rounding error will be introduced into the data, spline interpolation improves the spatial coherency within the nearest 3 neighbours, it should be born in mind in the follow-up analysis.

2.3 AIA image flux noise analysis

AIA outperforms TRACE (Handy et al. 1999) in FOV, temporal cadence and the number of observing channels. It resembles TRACE in most aspects, and many of the calibration and data preparation routines are adopted from the TRACE programme. We followed the study of Aschwanden et al. (2000) on TRACE and analysed the noise of the AIA 171 Å image flux. Data obtained in other EUV/UV channels can be analysed similarly.

In the data calibration, we neglected the uncertainties introduced by preparing the data from level 1 to 1.5, namely the errors accompanying the roll angle rotation and plate scale resizing, because the data processing is irreversible and untraceable (detached from CCD pixels). Therefore the data noise was analysed by assuming the data are in level 1 (connected to the CCD pixels). For a pixel flux value F, we combined the uncertainties generated from all the steps in unit of data numbers (DN), accumulated over a fixed exposure time of $2\,\mathrm{s}$, the photon Poisson noise σ_{photon}, electronic readout noise $\sigma_{\mathrm{readout}}$, digitisation noise σ_{digit}, compression noise $\sigma_{\mathrm{compress}}$, dark current noise σ_{dark}, subtraction noise $\sigma_{\mathrm{subtract}}$, and the noise due to removal of spikes in the images σ_{spikes} (Aschwanden et al. 2000):

$$
\begin{aligned}
\sigma_{\mathrm{noise}}^2(F) = {} & \sigma_{\mathrm{photon}}^2(F) + \sigma_{\mathrm{readout}}^2 + \sigma_{\mathrm{digit}}^2 + \sigma_{\mathrm{compress}}^2 \\
& + \sigma_{\mathrm{dark}}^2 + \sigma_{\mathrm{subtract}}^2 + \sigma_{\mathrm{spikes}}^2(F).
\end{aligned}
\tag{2.10}
$$

We first examine the photon statistics. The image flux in units of DN was translated from the charge readout from each pixel through an analog-to-digital converter (ADC). The camera gain G_λ (e/DN) is defined as the number of electrons acquired in the detector to generate a unit DN read in the image pixel, it is a telescope (bandpass λ) specific parameter (Boerner et al. 2012, Table 6). The electrons are accumulated in the detector and follow Poisson statistics, thus for a pixel flux F in the image in bandpass λ, FG_λ electrons are detected with an uncertainty of $\sqrt{FG_\lambda}$, so the photon noise in F is $\sqrt{FG_\lambda}/G_\lambda = \sqrt{F/G_\lambda}$.

The intrinsic trait of CCD is the readout noise that is inevitable in all applications. The readout noise in AIA CCDs is $\approx$ 20-22 e = 1.1-1.2 DN. For the 171 Å images, it is constant $\sigma_{\mathrm{readout}} = 1.15\,\mathrm{DN}$ (Boerner et al. 2012).

The rounding of the ADC signal into integer introduces a maximum uncertainty of $\sigma_{\mathrm{digit}} = 0.5\,\mathrm{DN}$ (Aschwanden et al. 2000).

The AIA images implement the Rice compression algorithm, a lossless compression. A look-up table was used with the bin size proportional to the pixel value (Boerner 2011), thus we assume the noise $\sigma_{\mathrm{compress}} = 0.25\sigma_{photon}$ as suggested in

Boerner (2011). The TRACE images deployed the *jpeg* data compression algorithm, a lossy compression algorithm. The average noise caused by the compression for the entire image was estimated as $\sigma_{\mathrm{compress}} \lesssim 0.1\,\mathrm{DN}$ (Aschwanden et al. 2000). The compression noise for TRACE was underestimated.

The noise caused by the dark current is quite low. In the current AIA operation, the seasonal variation has not be corrected yet, and we assumed a half digit noise level $\sigma_{dark} = 0.5\,\mathrm{DN}$ (Boerner 2011).

Subtracting the dark current, as well as the background variation, in integer DN in the data processing from level–0 to level–1, adds two additional digitisation errors, $\sigma_{\mathrm{subtract}} = \sqrt{2 \times 0.5^2} = 0.7\,\mathrm{DN}$ (Aschwanden et al. 2000).

The de-spiking algorithm for AIA images was directly adopted from the TRACE programme (Lemen et al. 2012), so the uncertainty analysis is transferable as well. In the deep cleaning algorithm (Aschwanden et al. 2000), if a pixel value is above $q_{\mathrm{thresh}} = 1.15$ times its local median value (defined by the nearest eight neighbours around the spiky pixel), it would be replaced with the local median, three iterations were applied to the images. A residue of $\sigma_{\mathrm{spikes}}(F) = F(q_{\mathrm{thresh}} - 1) = 0.15F$ was generated in the spiky pixel and its nearest four neighbours (Aschwanden et al. 2000). In Aschwanden et al. (2000), an uncertainty of $\sigma_{\mathrm{spikes}}(F) = 0.15F$ was assigned to each pixel empirically. In AIA images, about 10^4 pixels out of 4k × 4k are normally hit by energetic particles in quiet Sun condition (Boerner 2011). As an upper limit, we therefore assume that about 10^5 pixels (0.6%) are affected, and estimated $\sigma_{\mathrm{spike}}(F) = 0.006 \times 0.15F = 0.0009F$ for the entire image.

Then we summarised the above estimations, the data noise for a signal pixel with the flux value F in the 171 Å images is

$$
\begin{aligned}
\sigma_{\mathrm{noise}}(F) &= \sqrt{(1 + 0.25^2)\frac{F}{17.7} + 1.15^2 + 4 \times 0.5^2 + (0.0009F)^2} \\
&\approx \sqrt{2.3 + 0.06F}\,(\mathrm{DN})
\end{aligned}
\tag{2.11}
$$

The data noises of different origin in the 171 Å bandpass are plotted in Fig. 2.7 as a function of the image flux F. The photon noise is comparable to the other noises, caused by readout and dark current extraction and compression, at lower flux value F, and become the dominant noise at the flux value of hundreds and over. The de-spiking noise is practically negligible, but could become significant during a flare.
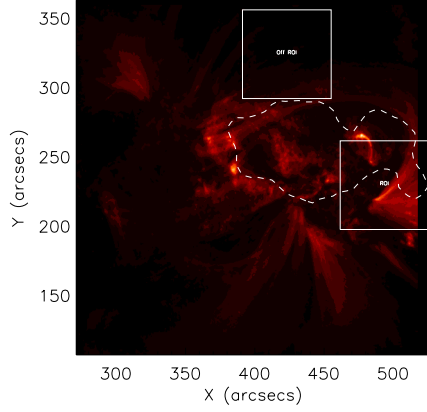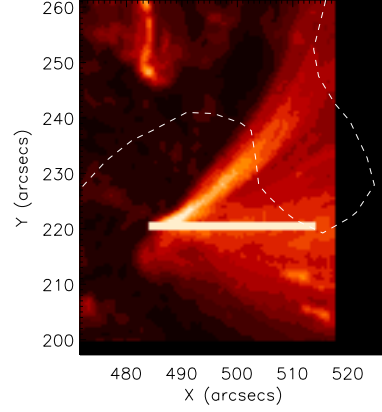
(a)   (b)
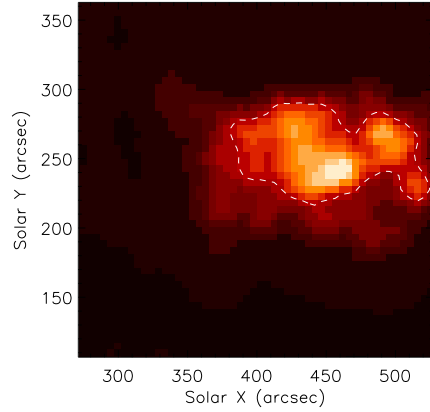
(c)

Figure 2.1: (a) The field of view over AR8253 taken at 1998-07-01 01:01 UT in TRACE 171 Å bandpass, the region of interest (ROI) in the white box includes the fan-like structure and is re-sized to the left, an off-ROI region including the weakest intensity area is marked to the top. (b) The region of interest (128×128 pixels) showing the fan-like structure; a slit of the macro-pixels (3×3) is selected along the fan. (c) The intensity map of 17 GHz radio emission over AR8253 at 1998-07-01 01:01 UT. The contour in dashed line marked the sunspot area.
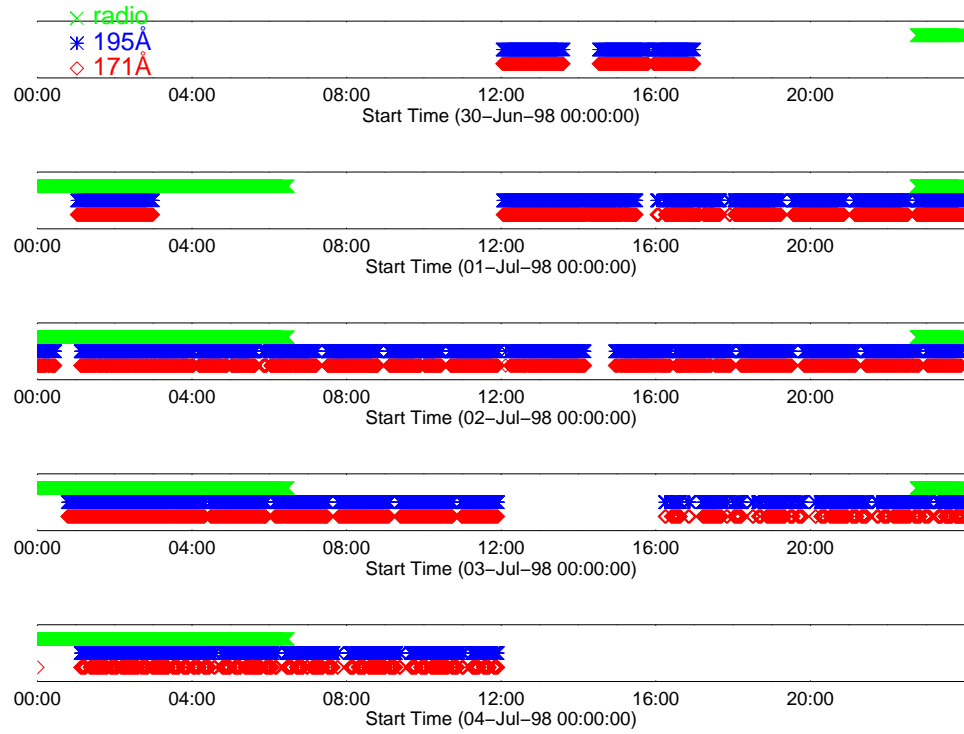
Figure 2.2: Observational coverage over AR8253 by TRACE 171 Å (red) and 195Å (blue), and NoRH 17 GHz (green) in the analysed time interval. Small gaps in EUV observations of order 100 s are due to channel switching, and large ones are due to routine observations on the solar limb (including polar regions), re-pointing or to avoid radiation belts.
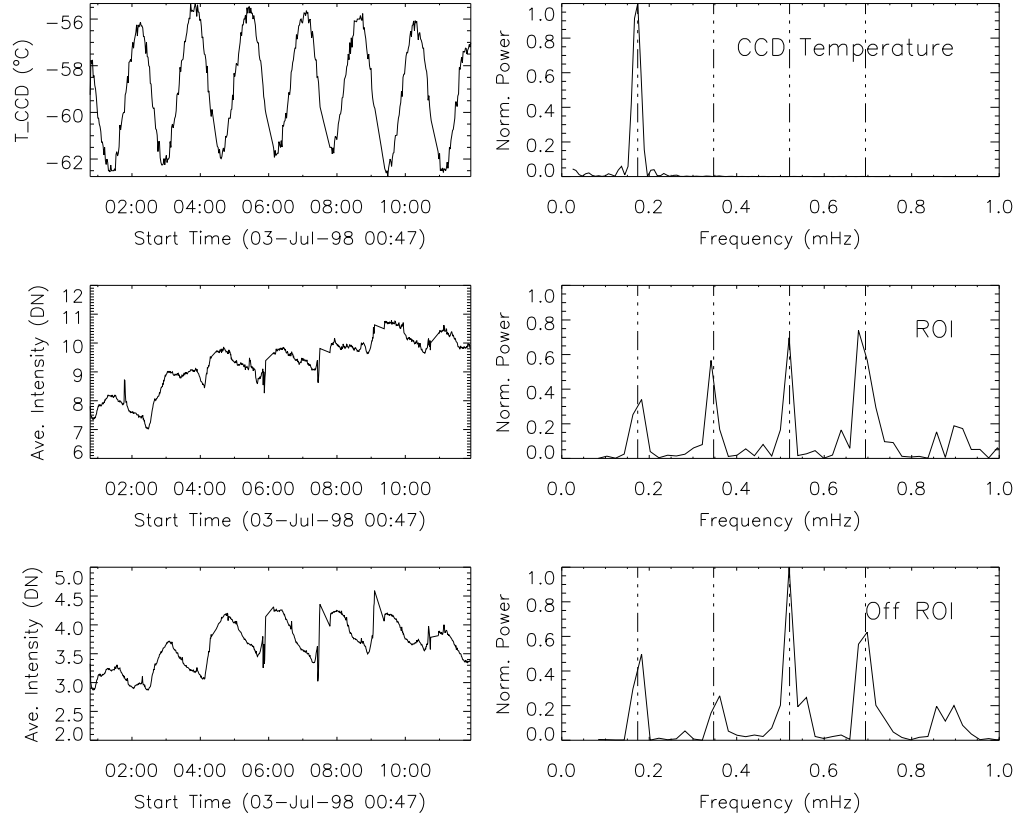
Figure 2.3: Left column: time series (1998-07-03 00:47 - 12:00 UT). Right column: the corresponding normalised power spectra, a 30-min running average is removed from the intensity time series beforehand, the harmonics of the orbital periods are marked with the vertical dash-dot-dot lines, corresponding to the periods 96, 48, 32, 24 min. From top to bottom row: TRACE CCD temperature variation (°C), the average intensity (DN) of the ROI, and off ROI.
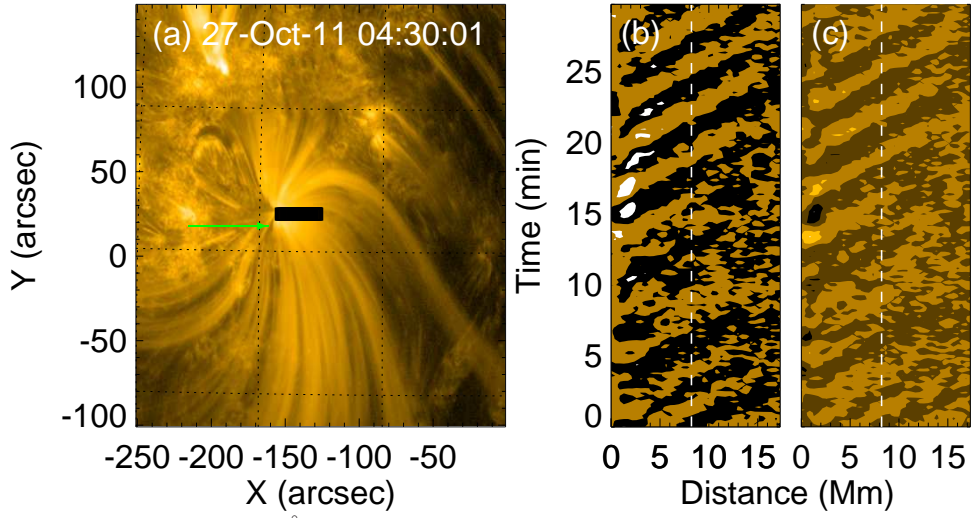
Figure 2.4: a) AIA 171 Å image of active region NOAA 11330 observed on 27 Oct 2011 at 04:30:01 UT is shown with the flux on the logarithmic scale. The green arrow labels a bright loop in dark backgound, used to study the de-rotational artifacts as detaled in Sec. 2.2. A cut that was taken to make the time-distance plot is indicated with a black bar. b) The running difference R_1 of the time-distance plot started at 04:30:01 UT. R_2 is the first half of R_1, to the left of the white dashed line. It covers about 10 cycles of the propagating features. Panel (c) shows the background-subtracted time-distance plot D_1. The first half of D_1 on the left of the white dashed line is D_2.
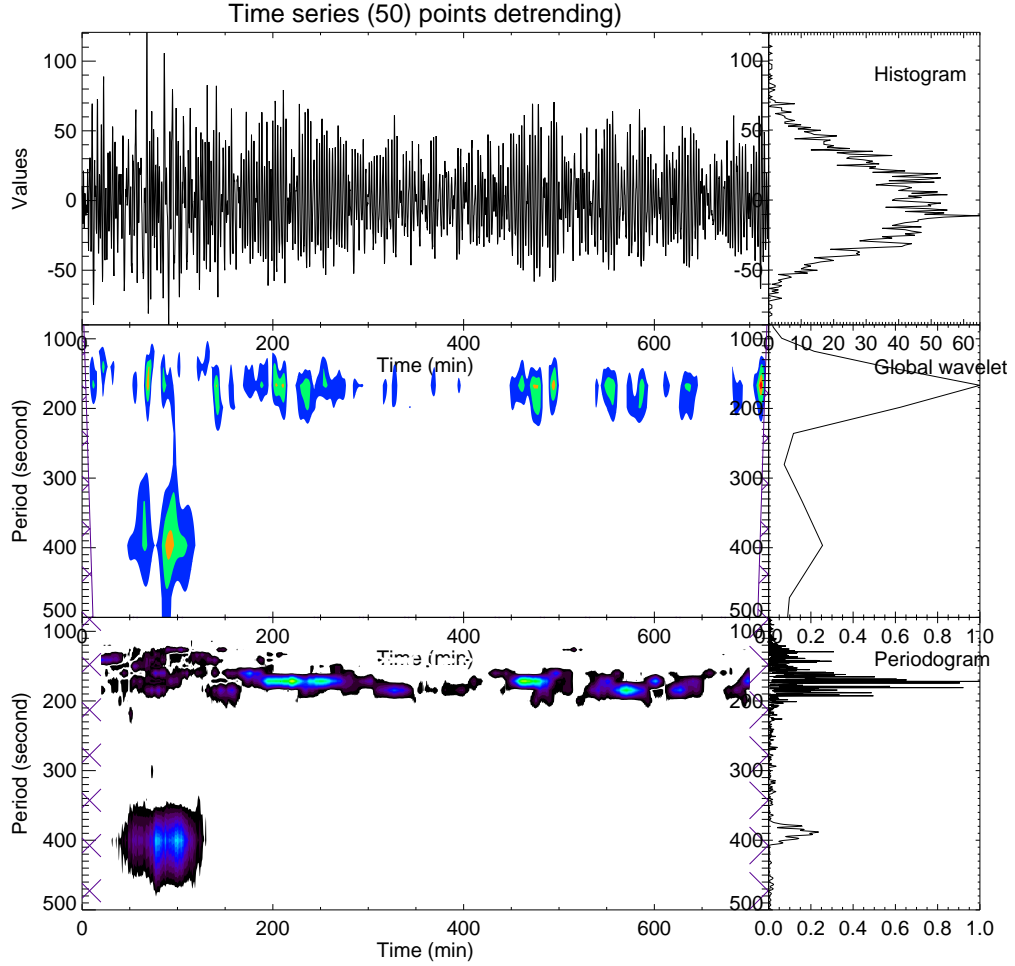
Figure 2.5: Top left: the temporal intensity variation of a macro-pixel of 3×3 pixels, the time series is detrended by removing the running average of 50 data points. The histogram is displayed on the top right. Middle left: the Morlet wavelet analysis to the time series displayed above, the COI is cross-hatched. Middle right, the global wavelet. Bottom left: windowed FFT transform with a Gaussian function with window size of 60 min. The parts of the spectrum that is subject to edge effect are cross-hatched. Bottom right: the periodogram spectrum.
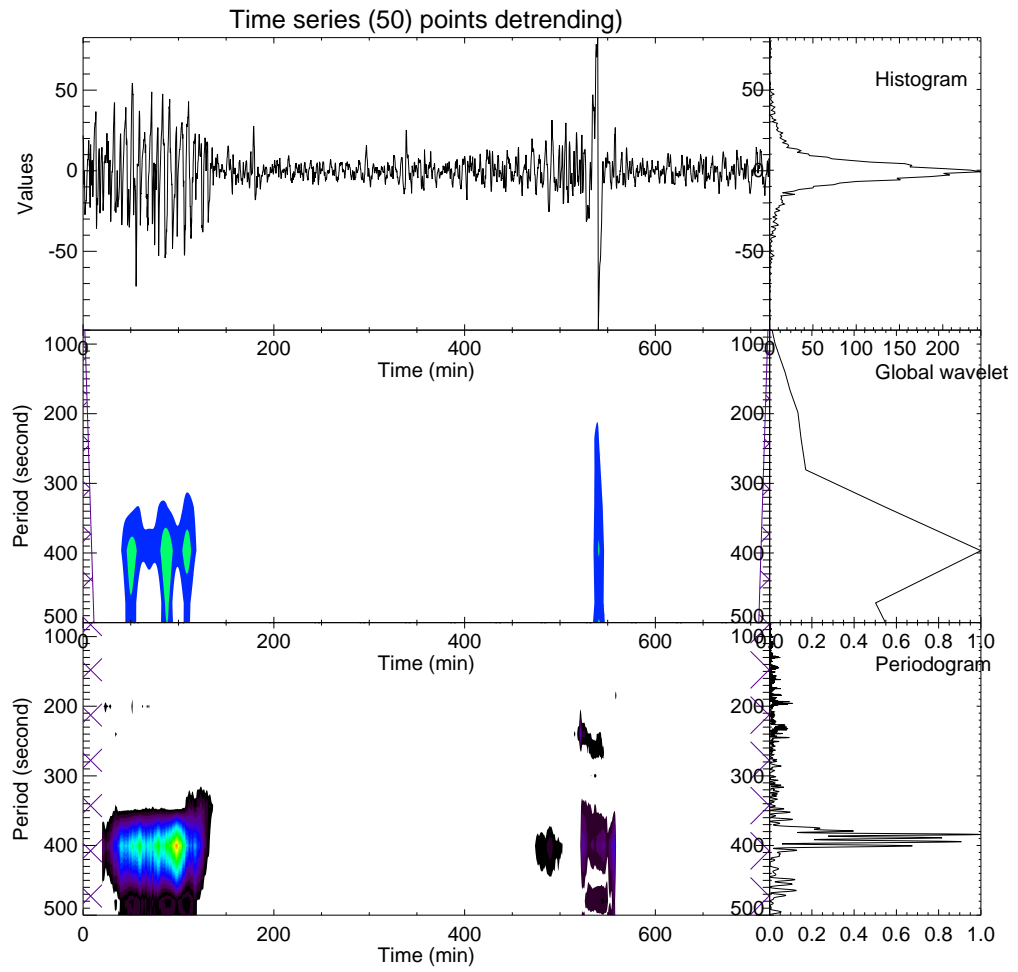
Figure 2.6: The same as Fig. 2.5, but for the average intensity of the loop indicated in Fig. 2.4.
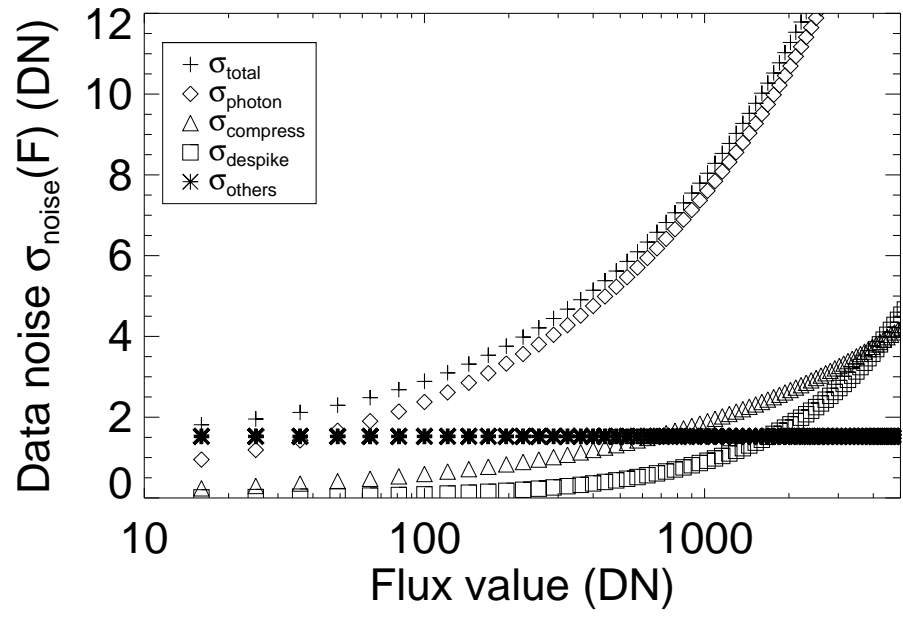
Figure 2.7: Data noise $\sigma_{noise}(F)$ (plus sign) in Eq. (2.11) as a function of pixel flux F in AIA 171 Å images. The components caused by the photon noise, compression, de-spiking and other reasons are plotted with diamonds, triangles, squares and stars, respectively.

Chapter 3

Waves and oscillations in sunspot atmospheres

3.1 Introduction

Sunspot oscillations are one of the most prominently studied magnetohydrodynamic wave phenomena in solar physics (e.g. Lites et al. 1992; Bogdan 2000; Bogdan & Judge 2006). The interest in these oscillations arise particularly from their use as a tool to probe the structure of the sunspot atmosphere (e.g. Zhugzhda et al. 1983; Shibasaki 2001; Zhugzhda 2008; Botha et al. 2011), and photospheric-coronal magnetic connectivity (e.g. Sych et al. 2009). Also, sunspots and their magnetic field are excellent test grounds for the MHD wave theory (e.g. Cally 2005; Khomenko & Collados 2006) and for the interaction of acoustic waves with the magnetic field concentrations (e.g. Cally et al. 2003; Gordovskyy & Jain 2008). Moreover, sunspot oscillations appeared to reveal the internal, sub-photospheric structure of sunspots (e.g. Zhugzhda 2008).

It is known that the oscillating power with different periods is non-uniformly distributed over a sunspot (e.g. Bogdan & Judge 2006) in both horizontal and vertical directions. In particular, 3-min oscillations occupy the umbral part of the sunspot with the maximum power in the chromosphere (e.g. Abdelatif et al. 1986; Reznikova et al. 2012). The effect of height inversion takes place: over the umbra, the spatial location of the horizontal maximum of 3-min oscillation power in the chromosphere corresponds to the relative decrease in the power of these oscillations in the photosphere (e.g. Kobanov et al. 2011). In the corona, 3-min oscillations become propagating slow magnetoacoustic waves, and follow magnetic fan structures stretched upwards from the sunspot (e.g. Kiddie et al. 2012; Yuan & Nakariakov

2012).

On the other hand, in large sunspots 5-min oscillations are usually suppressed inside the umbra, and have the maximum power at the umbra-penumbra boundary, forming a ring-structure enclosing the sunspot (see Nagashima et al. 2007; Sych & Nakariakov 2008; Reznikova et al. 2012; Yuan et al. 2012, for recent results). Analysing the phase of the oscillations in the ring structure reveals that they form patches of opposite phase along the ring (e.g. Zhugzhda et al. 2000; Nindos et al. 2002; Sych & Nakariakov 2008). Moreover, oscillations of different physical quantities, e.g., the line-of-sight velocity, intensity and the magnetic field are observed to have different spatial structure. The physical mechanism responsible for such a behaviour is still under debate. Solar p-mode acoustic waves are candidate energy source (Abdelatif et al. 1986). In particular, the interaction of p-modes with the strong magnetic field in the sunspot can lead to the excitation of the magnetoacoustic modes (e.g. Cally & Bogdan 1997; Cally et al. 2003; Schunker & Cally 2006; Khomenko 2009). The oscillations intermittently localised at the umbra-penumbra boundary can be associated with the "whispering gallery" mode, which is a magnetoacoustic mode of the sunspot magnetic flux tube with a high azimuthal wavenumber m (Zhugzhda et al. 2000). However, as it was pointed out in Zhugzhda et al. (2000) there are alternative interpretations, e.g. connection with the random filamentary structure of the magnetic field near the umbra-penumbra boundary.

Mangetoacoustic gravity (MAG) waves in the solar atmosphere are subject to strong dispersion: their properties depend strongly on the frequency. In particular, the parameters of the solar atmosphere determine the MAG cut-off frequency. MAG waves with frequencies below the cut-off value become evanescent, and therefore cannot reach the upper layers of the solar atmosphere. The cut-off value also determines the oscillating frequency of MAG waves as the response of the atmosphere to a broadband (e.g., impulsive) excitation (e.g. Suematsu et al. 1982; Botha et al. 2011). The cut-off frequency for MAG waves was derived for a stratified isothermal solar atmosphere permeated by a uniform magnetic field (Bel & Leroy 1977; Zhugzhda & Dzhalilov 1984). It generally depends on the local plasma β ($\beta = 2\mu_0 p/B^2 = 2C_{\rm s}^2/\gamma V_{\rm A}^2$, where p is the gas pressure, μ_0 is the magnetic permeability in vacuum space, B is the magnetic field strength, $V_{\rm A}$ is the local Alfvén speed, $C_{\rm s}$ is the local sound speed, and $\gamma = 5/3$ is the adiabatic index) and the magnetic field inclination ϕ. In the high-β regions ($\beta \gg 1$, e.g. the photosphere and chromosphere of the quiet Sun), it is reduced into the pure acoustic cut-off frequency $\nu_0 = \gamma g/4\pi C_{\rm s} = 5.2\,{\rm mHz}$ (with the corresponding cut-off period $p_0 = 3.2\,{\rm min}$), where $g = 274\,{\rm m/s^2}$ is the gravitational acceleration, and $C_{\rm s} = 7\,{\rm km/s}$ is the sound speed

estimated for typical chromospheric conditions. In the low-β approximation ($\beta \ll 1$, e.g. in a sunspot or coronal active region), the cut-off frequency is modified by the magnetic inclination $\nu_{ac} = \nu_0 \cos\phi$ (Bel & Leroy 1977)[1]. This helps explaining the existence of low-frequency waves in the corona, which are believed to carry a larger portion of energy flux than its high-frequency counterpart (e.g. Fontenla et al. 1993; Jefferies et al. 2006). Also, the study of the cut-off frequency effect on compressive waves observed in the solar atmosphere provides us with a seismological tool to determine the local geometry of the magnetic field.

According to Bel & Leroy (1977), the low-frequency (long-period) waves are able to penetrate the upper solar atmosphere, along the magnetic concentrations, e.g. sunspots, pores, which work as MAG waveguides. It was suggested that, due to the effect of the magnetic inclination, the 5–min oscillations appear in the chromospheric spicules (De Pontieu et al. 2004) and in coronal loops at active regions (De Moortel et al. 2002b; De Pontieu et al. 2005). de Wijn et al. (2009) observed the propagation of solar global p-modes to the chromosphere through the inclined magnetic fields at the periphery of plage regions. Other observations of long-period oscillations in the corona could be attributed to channelling by the inclined field as well (see e.g. Wang et al. 2009b; Marsh et al. 2009; Yuan et al. 2011).

A direct observation of the magnetoacoustic cut-off in a sunspot has been performed with full Stokes (I, U, V, Q) spectropolarimetry (see Fig. 5 in Bloomfield et al. 2007). The authors found that the cut-off frequency closely followed the magnetic field modification in the strong-field limit ($\beta \ll 1$) of Bel & Leroy (1977). However no further examination was done to compare the information with the magnetic inclination inverted by full Stokes observables. It appeared that the correlation and phase difference of the time series of the intensity variation obtained at various heights of the solar atmosphere looked more realistic when the offsets at the spatial location were corrected by considering the magnetic inclination (Bloomfield et al. 2007). McIntosh & Jefferies (2006) studied the travel time of narrow-band signals around a sunspot and found good consistency with the prediction of Bel & Leroy (1977) for both the quiet sun ($\beta \gg 1$) and a sunspot ($\beta \lesssim 1$). Tziotziou et al. (2006) applied the empirical formula $\nu_{peak}(\phi) \approx 1.25\nu_{ac}(\phi)$, where ν_{peak} denotes the peak frequency at each location, ν_{ac} indicates the corresponding magnetoacoustic cut-off frequency, to the waves observed in a sunspot's chromosphere, and estimated the magnetic field inclination $\phi = \arccos[\nu_{peak}/(1.25 \times \nu_0)]$ (Bogdan & Judge 2006). Reznikova et al. (2012) compared the spectra and phase relations of the UV and

---

[1] The derivations in Bel & Leroy (1977) contain obvious misprints, Sec. 1.2.3 redo the derivation. However the numerical results and figures are reliable. In this work, we use the trustworthy extreme case of $\beta \ll 1$

EUV emission intensity at various heights of the solar atmosphere to identify the features of upwardly propagating waves and found that the variation of the cut-off frequency across the umbra was consistent with Bel & Leroy (1977). The follow-up study (Reznikova & Shibasaki 2012) compared the observational MAG cut-off frequencies in AIA 304 Å with the values obtained by the potential field extrapolation (Sakurai 1982) and found good agreement.

In Bel & Leroy (1977), an adiabatic plasma was implicitly assumed, while in the photosphere and chromosphere, radiative loss is of significance. Centeno et al. (2006, 2009) used a linear wave equation with a radiative cooling term and explained well the observed phase delay and wave amplitude variation with height in both sunspots and pores. A detailed study using multiple spectral lines formed at different heights was presented in Felipe et al. (2010). The connectivity of different layers of the atmosphere determined by the phase difference and power amplification was demonstrated. Therefore, the study of the cut-off frequency can also retrieve the plasma parameters associated with radiative losses.

3.2 Detection of high-order azimuthal mode in sunspot

In this section, we consider the observational evidence of the high-m azimuthal modes in a sunspot observed with SDO/AIA. The modes have the period of about 5–minutes, and are observed at the umbra-penumbra boundary. We demonstrate that the phase of the 5-min oscillations varies periodically with the azimuthal angle.

3.2.1 Observation

In this study we used the SDO/AIA 1700 Å, 1600 Å and 304 Å) data (see Lemen et al. 2012; Boerner et al. 2012; Yuan & Nakariakov 2012, for instrumentation, calibration and image flux error analysis, respectively. Also see Sec. 1.1.6). The images are taken with cadence of 24 s in the two UV channels and 12 s in the EUV channel, respectively. We used the observations of the NOAA AR 11131 from 02:30 to 03:30 UT 08 Dec 2010. The sunspot lower atmosphere was well imaged in all these channels (see Fig. 3.1). The data sets were prepared with the standard routine *aia_prep.pro* (v4.13).

The sunspot considered in this study was situated near $30^{°}$ latitude in the northern hemisphere. It crossed the central meridian on 08 Dec 2010. It is a pretty large and symmetric sunspot with the umbra and penumbra size of about ~10 Mm and 22 Mm in diameter, respectively. It consisted of a strong magnetic concentration of south polarity. Sources of the north polarity are spread sparsely to the west and
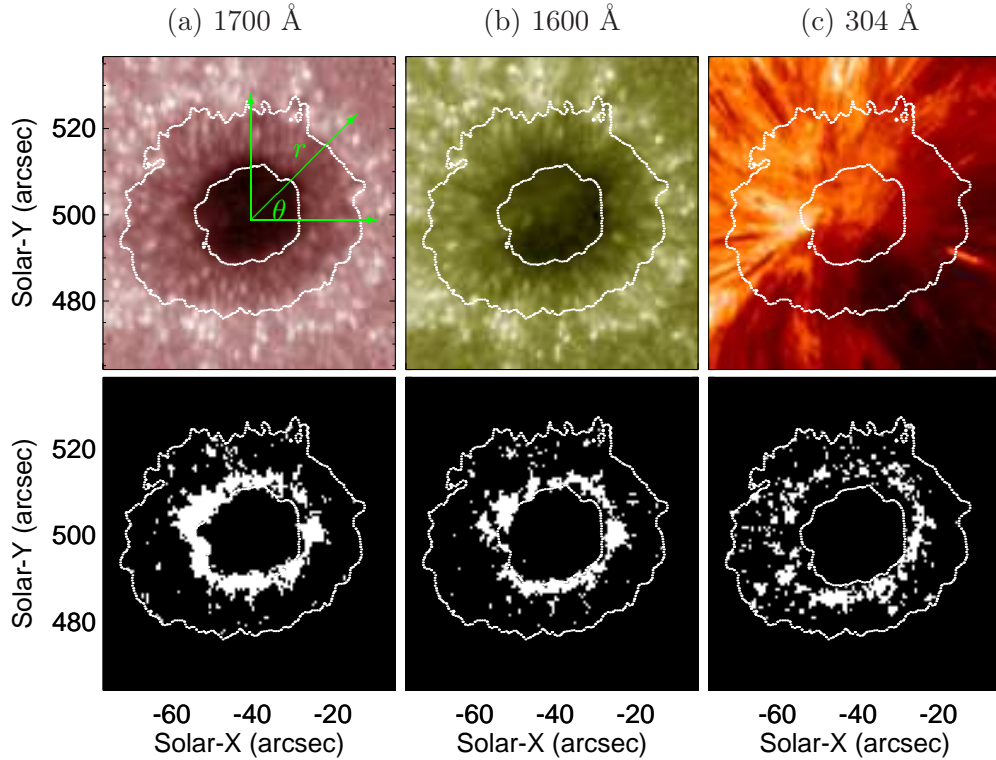
Figure 3.1: Top row: AIA intensity images of sunspot AR 11131 on 08 Dec 2010, shown on a logarithmic scale, demonstrate different levels: the temperature minimum level (1700 Å), the upper photosphere and transition region (1600 Å) and the chromosphere (304 Å) of the sunspot's atmosphere. Bottom row: The corresponding 5-min masks in each bandpass accounting the pixels where the strongest oscillating period ranges from 4.5 - 5.5–min. The polar coordinate system used in this study is shown in (a). The dotted lines show the boundaries of umbra and penumbra, determined with the 4500 Å intensity image.

north of the sunspot. This sunspot has already been the subject of detailed studies Reznikova et al. (2012); Reznikova & Shibasaki (2012); Yuan et al. (2012).

3.2.2   Analysis

For all three bandpasses used in this study, the narrowband power maps for the periods $2, 2.1 \ldots, 20$ min were prepared with the Pixelised Wavelet Filtering technique (Sych & Nakariakov 2008; Sych et al. 2010). The 5-min power maps are shown on the left column in Fig. 3.2. The 5-min spatial mask (Fig. 3.1, bottom rows) was obtained by accounting the pixels where 5 ± 0.5 min was the peak period in the spectra in each channel. The correlation map (Fig. 3.2, central column) was ob-

tained by filtering the intensity signals in each pixel with a Gaussian filter centred at $3.3\,\mathrm{mHz}$ with $\sigma = 0.3\,\mathrm{mHz}$. The maximum cross-correlation coefficient was obtained by cross-correlating the intensities in each pixel to the average signal of the filtered data set within the 5-min mask. The phase map (Fig. 3.2, right column) was obtained by Fourier analysing the original intensity signals. A very similar result was also obtained with the nonlinear least-square fitting technique.

The power, correlation and phase maps all show the clear ring-shaped nodal patterns, clearly demonstrating the oscillatory dependence on the polar angle θ (see Fig. 3.2). To quantify this effect, we took the average phase ϕ and the correlation coefficients R over radial direction at every $5°$ of the polar angle θ, (see left columns in Fig. 3.3, Fig. 3.4 and Fig. 3.5). The uncertainties of the phase ϕ and the correlation coefficients R are set to the corresponding standard deviations over radial direction. The variations of phase $\phi(\theta)$ and $R(\theta)$ with the polar angle θ were smoothed with a running difference of 30 data points with edge wrapping and fitted with the function $A\cos(m\theta + \delta)$ using *mpfitfun.pro* (Markwardt 2009). The azimuthal mode m must be an integer, but for the calculation purpose, we treat it as a real number. However we accept only its nearest integer value. The fits are over-plotted on the top of the general trends in each panel. The fit results are presented in Table 3.1.

The best-fitted curves show that the dependences $\phi(\theta)$ and $R(\theta)$ have more than one mode of oscillation. The Lamb-Scargle periodogram (Scargle 1982; Horne & Baliunas 1986, also Sec. 1.3.2) gave us the power spectra as a function of azimuthal mode number m (see the left columns of Fig. 3.3, Fig. 3.4 and Fig. 3.5). The significance of the spectral peaks was assessed by using the Horne & Baliunas (1986, also see Sec. 1.3.2) test based on the exponential noise distribution and the Fisher randomisation test (Linnell Nemec & Nemec 1985b) with no bias in noise distribution (see details in Inglis & Nakariakov 2009; Yuan et al. 2011, and also Sec. 1.3.2). In the Horne & Baliunas test, a false alarm probability of 0.05 was chosen. The Fisher randomisation test was performed with 1000 permutations in each run, using the PERIOD package developed in the Starlink project (Dhillon et al. 2001). Since both tests can only be applied to the highest peak in the spectrum, the maximum peaks were iteratively removed from the original signal with the time-series harmonic filter for assessing the significance of the next highest peak (Ferraz-Mello 1981; Yuan et al. 2011, also see Sec. 1.3.2).

3.2.3 Result

Fig. 3.2 shows the maps of 5-min power, correlation and phase at different levels of sunspot AR 11131. The regions of the enhanced power of 5-min oscillations form

a ring structure enclosing the sunspot umbra. The ring size increases, but becomes more diffused with height. The phase maps exhibit an oscillatory pattern along the ring, with the typical size of about 10–16 arcsec.

Non-linear fits to the phase and correlation coefficient distribution with the polar angle in 1700 Å (Fig. 3.3) give the mode number $m = 3.17 \pm 0.06$ and $m = 6.76 \pm 0.63$, respectively. The doubling is naturally explained, since the cross-correlation with positive and negative lags give the same value, therefore, a whole cycle is complete. While for phase, it just is a half cycle. In the periodogram analysis of the phase distribution, $m = 1.77 \pm 0.78$ and 3.55 ± 0.78 are detected with significance levels $p \leq 0.03$ in the Fisher randomisation test. In the correlation distribution, the periodogram gives $m = 3.28 \pm 0.26$ with $p \leq 0.03$. The second peak at $m = 2$ existed in the spectrum with significance level $p > 0.05$, therefore it is not listed in Table 3.1.

In the 1600 Å bandpass (Fig. 3.4), the same modes were detected at $m = 2.02 \pm 0.75$ and 3.29 ± 0.78 in the phase distribution and $m = 3.04 \pm 0.75$ in the correlation distribution with $p < 0.03$. An extra mode in the phase distribution was obtained at $m = 4.83 \pm 0.78$ with $p = 0.03$, the nonlinear fit got a similar value $m = 5.06 \pm 0.06$. In the correlation distribution, the nonlinear fit got 3.30 ± 0.39, similar to the periodogram analysis.

In the 304 Å bandpass (Fig. 3.5), higher modes were generally obtained. In the phase distribution, $m = 7.10 \pm 0.24$ was detected with $p = 0.03$ in the Fisher's randomisation test, while the false alarm probability in the Horne & Baliunas test is greater than 0.05. The mode in correlation distribution $m = 8.37 \pm 0.78$ was also detected with FAP greater than 0.05. In the Fisher's randomisation test, $p = 0.09$ was obtained. The nonlinear fits to phase and correlation distributions give 5.84 ± 0.06 and 7.05 ± 0.57, respectively. These values are different from their counterparts calculated in the periodogram.
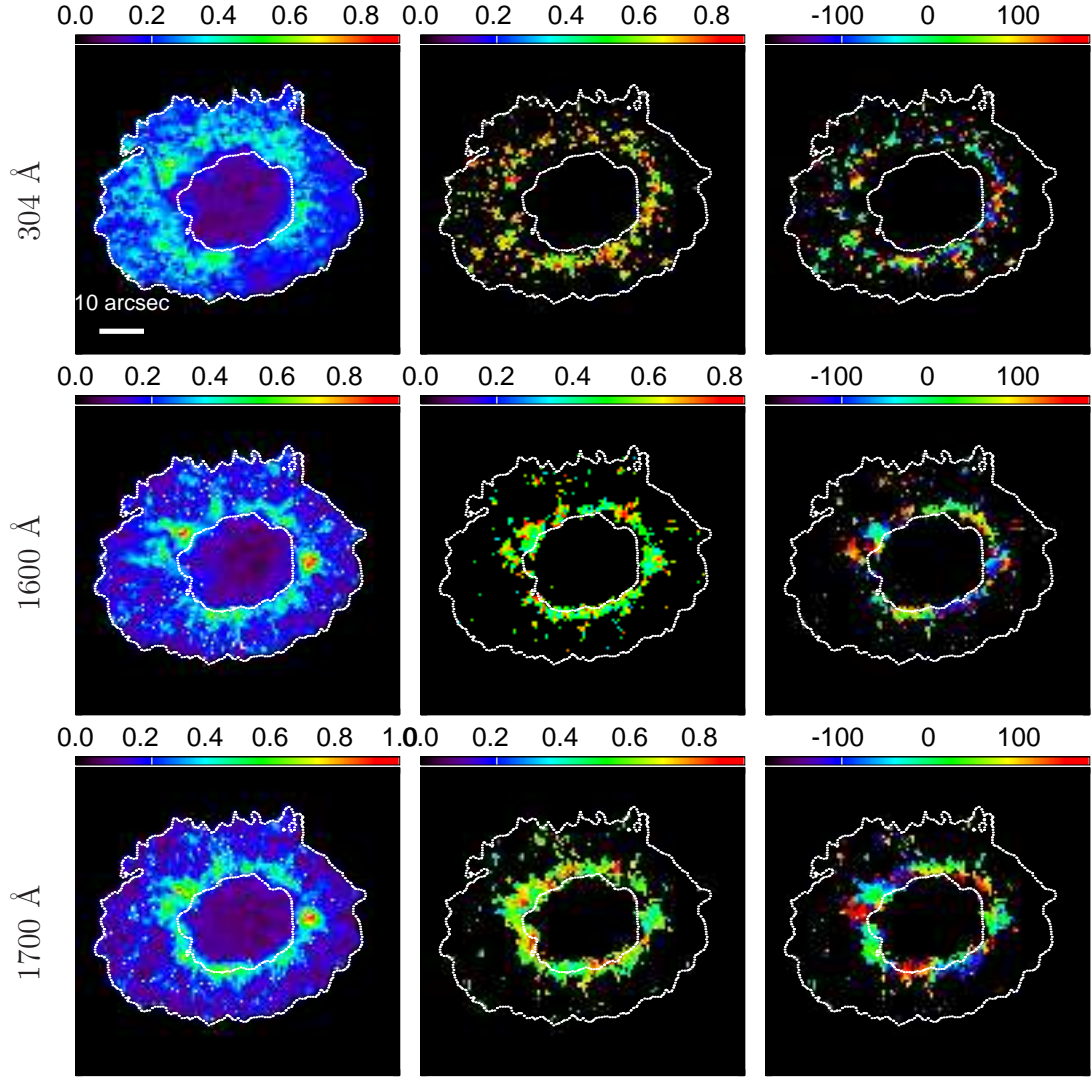
Figure 3.2: Left column: 5 min narrow band power maps. Middle column: correlation maps within the 5–min mask. Right column: The 5-min phase maps within the 5–min mask. The corresponding channel are labelled on the left edge, 304 Å, 1600 Å and 1700 Å from top to bottom. A bar in the top left panel shows the scale length of 10 arcsec. The dotted curves contour the umbra and penumbra border.
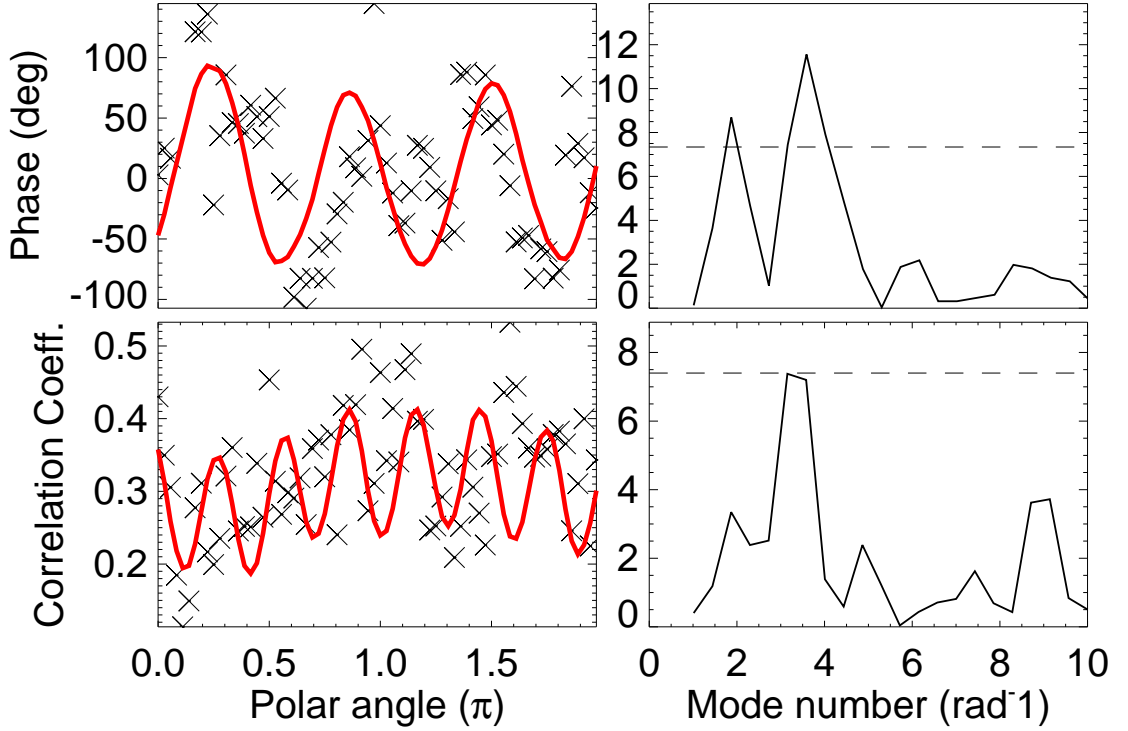
Figure 3.3: Top left: the angular distribution of the phase and its nonlinear fit (red solid line, $m = 3.17 \pm 0.06$). Top right: The periodogram of the phase distribution as a function of integer mode number m. Bottom left: the angular distribution of the correlation coefficient and its nonlinear fit (red solid line, $m = 6.76 \pm 0.63$). Bottom right: The periodogram of the correlation distribution as a function of mode number m. The dashed lines in the periodograms mark the significance level at 95%. The analysis was done with the 1700 Å data set.
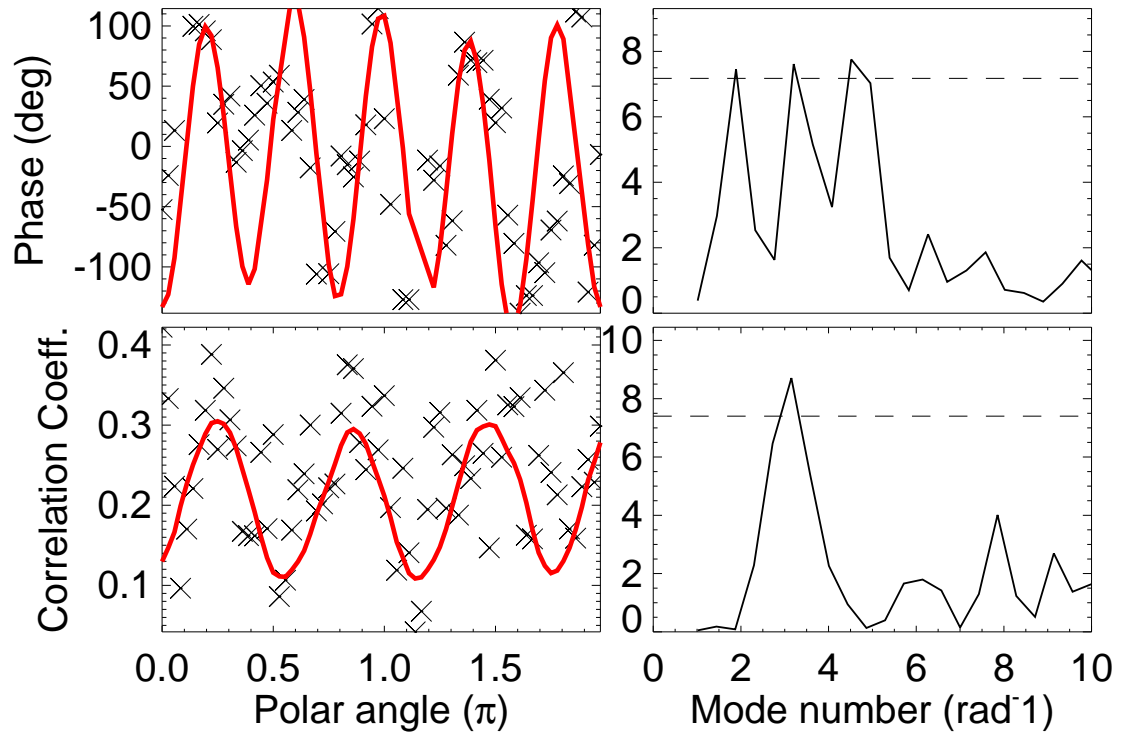
Figure 3.4: The same as Fig. 3.3 but by the 1600Å data set. $m = 5.06 \pm 0.06$ and 3.30 ± 0.39 were obtained in the nonlinear fit to phase and correlation distribution, respectively.
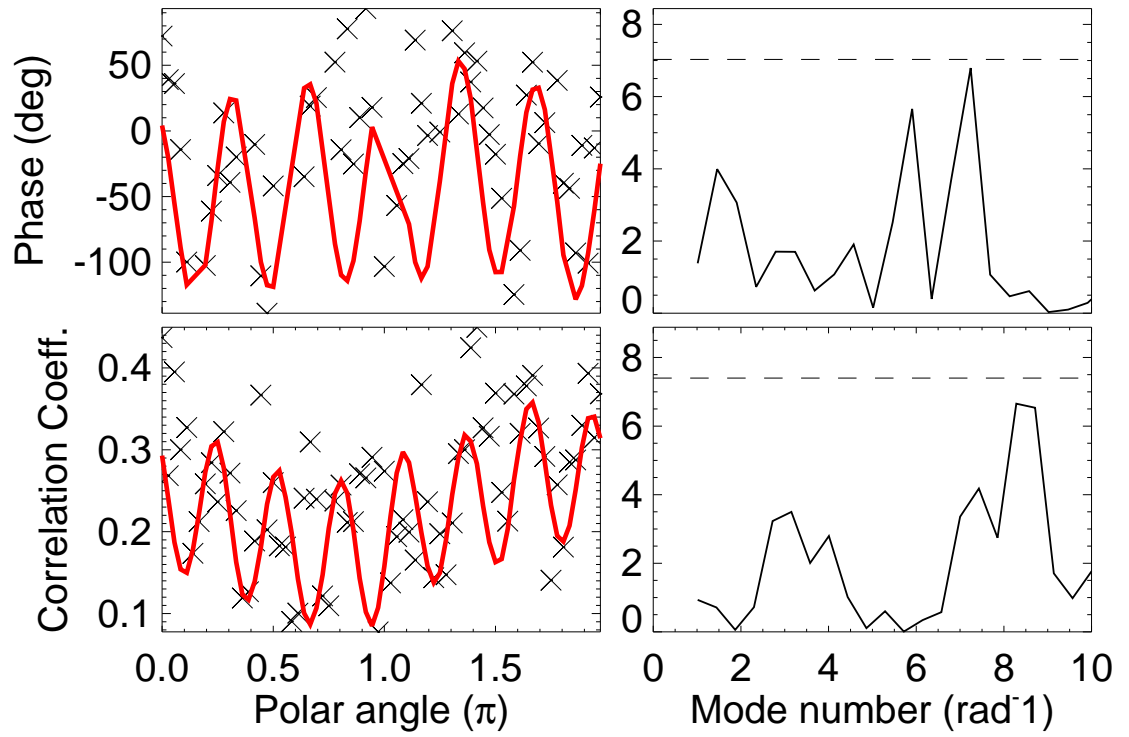
Figure 3.5: The same as Fig. 3.3 but by the 304Å data set. $m = 5.84 \pm 0.06$ and 7.05 ± 0.57 were obtained in the nonlinear fit to phase and correlation distribution, respectively.

Table 3.1: Summary of the detected modes and significance tests

Bandpass	Integer mode number	Phase distribution			Correlation distribution		
		Nonlinear fit	Periodogram	p-value	Nonlinear fit	Periodogram	p-value
1700Å	$m = 2$	$\ldots$	1.77 ± 0.78	≤ 0.03	$\ldots$	$\ldots$	$\ldots$
	$m = 3$	3.17 ± 0.06	3.55 ± 0.78	≤ 0.03		3.28 ± 0.78	0.03
	$m = 7$	$\ldots$	$\ldots$	$\ldots$	6.76 ± 0.63	$\ldots$	$\ldots$
1600Å	$m = 2$	$\ldots$	2.02 ± 0.75	≤ 0.03	$\ldots$	$\ldots$	$\ldots$
	$m = 3$	$\ldots$	3.29 ± 0.78	≤ 0.03	3.30 ± 0.39	3.04 ± 0.75	0.03
	$m = 5$	5.06 ± 0.06	4.83 ± 0.78	0.03	$\ldots$	$\ldots$	$\ldots$
304Å	$m = 6$	5.84 ± 0.06	$\ldots$	$\ldots$	$\ldots$	$\ldots$	$\ldots$
	$m = 7$	$\ldots$	$[7.10 \pm 0.24]$	0.03	7.05 ± 0.57	$\ldots$	$\ldots$
	$m = 8$	$\ldots$	$\ldots$	$\ldots$	$\ldots$	$[8.37 \pm 0.78]$	0.09

The detected values with more than 0.05 false alarm probability in the Horne & Baliunas test are enclosed in square bracket.
p-values less than 0.03 (the lower detection limit) in the Fisher's randomisation test are denoted as ≤ 0.03

3.2.4 Conclusion

In this study, the analysis of the 5-min oscillation power ring structure enclosing a sunspot umbra was reported with the AIA data. It exhibited a stronger power, larger local interaction scale and better nodal structure in the lower atmosphere (1700Å and 1600 Å), these features get more diffused and less clear in the chromosphere (304 Å). This indicates that the 5-minute oscillations originates in the photosphere (1700 Å) or even deeper.

In the phase distribution of 1700 Å and 1600 Å bandpasses, $m = 2, 3$[2] were detected significantly, while in the correlation distribution, only $m = 3$ was detected in both bandpasses. The best-fits to the phase and correlation distribution in 1700 Å bandpass gave $m = 3.17 \pm 0.06$ and 6.67 ± 0.21, respectively. The doubling in the correlation distribution arises from its non-negativity. However in the 1600 Å bandpass, a higher mode $m = 5.84 \pm 0.06$ was obtained in the best-fit to the phase distribution and $m = 3.30 \pm 0.39$ in the correlation distribution, respectively. This may be caused by the extra peak $m = 5$ appearing in the phase periodogram. In the 304 Å data, higher modes $m = 6, 7$ and 8 were obtained. The best-fit and periodogram gave different values in both the phase and the correlation distribution. Less consistency were shown with modes detected in lower atmosphere (1600 Å and 1700 Å).

The physics causing this high azimuthal modes is not clear. Given that it modulated the phase of 5–min oscillation, the travel time of 5–min oscillations to the height of each bandpass can be expressed in a format of $\int_{z_0}^{z_\lambda} v_p^{-1}(z, \cos m\theta)dz + \phi_0(\theta)/\omega_5$, where v_p is the phase speed of 5-minute oscillation as a function of height z and azimuthal variation $\cos(m\theta)$, z_λ denotes the height of bandpass λ (1700, 1600 and 304), while z_0 indicates the origin of 5-min oscillation, $\phi_0(\theta)$ is the initial phase of the 5-min oscillation at forming time, ω_5 is the angular frequency of 5-min oscillation. To build up a peak-to-peak azimuthal contrast around 2π, either the 5-min oscillation should be deeper enough, and therefore it allows the long-travel accumulation, or the modulations (perturbations) to v_p should be large enough, or a combination of both of them.

One possible explanation is the multi-mode oscillations of sunspot as theorised in Sec. 1.2.2 and Zhugzhda et al. (2000); Staude (2002), which is an extension of wave modes in a plasma cylinder (Roberts & Webb 1978; Edwin & Roberts 1983b) to larger magnetic bundle. The slow body modes with $m > 1$ confine the maximum

---

[2]Considering the error bars and noise different channels, in the following discussion, we adopt integer mode number m referring to values obtained in periodogram, while the best-fit values were kept in original format. Note all the error bars in this section use 3σ value.

modulations at certain radial locations less than the sunspot radius R, specified by high-mode m Bessel function J_m. The modulations to sound speed and Alfvén speed are also subject to azimuthal variation $\cos(m\theta)$. A theoretical and numerical study is required to fully justify the results.

To directly observe a global multi-mode sunspot oscillation, a time-dependence study with intensity information is required. Given the large size of sunspots, a detailed study of the magnetic field and line-of-sight velocity variations can be resolved using full Stokes parameters with current ground-based instruments, but the observation interval may have to be sufficient long and cover several cycles of high-order azimuthal modes.

3.3 Mangetoacoustic gravity cut-off frequency

The cut-off frequency detected in a sunspot atmosphere is a good indicator of local plasma parameters, therefore it can be used to diagnose the local atmosphere, e.g. temperature, magnetic field inclination angle. In our study, we present the observation of the spatial distribution and height variation of the cut-off frequency with SDO/AIA (Lemen et al. 2012; Boerner et al. 2012, and Sec. 1.1.6) and infer the magnetic field inclination angle. The observational results were used to reconstruct the 3D geometry of the magnetic field. The information was deployed to diagnose the magnetic field inclination.

In this section, we present the analysed data sets in Sec. 3.3.1. The methods are summarised in Sec. 3.3.2. Then we compare the diagnostic results with the potential field extrapolation in Sec. 3.3.3, and conclusions are given in Sec. 3.3.4.

3.3.1 Observations

We selected two large sunspots associated with well-developed active regions in the corona, where outwardly propagating EUV disturbances were persistently detectable (Yuan & Nakariakov 2012). We chose good observation intervals without disruptions from either flares or other transient events. The observation intervals correspond to the days when the sunspots were crossing the central meridian: they were least affected by Wilson depression (Loughhead & Bray 1958) and were well exposed for imaging.

The first sunspot was the same sunspot studied in Chapter 3.2. We used AIA data sets of 1600 Å, 1700 Å and 304 Å from 02:30 to 03:30 UT 08 Dec 2010. The cadence time was 24 s for 1600 Å and 1700 Å images, and 12 s for 304 Å images.

This sunspot was also analysed in Reznikova et al. (2012); Reznikova & Shibasaki (2012); Yuan et al. (2012, 2013a).

The second sunspot chosen for this study was the leading main sunspot on the eastern part of active region AR 11330 situated slightly to the north of the solar equator. The trailing sunspot group of north polarity was about 150 Mm to the main sunspot. It formed into a non-symmetric shape with a protrusion due to the tearing of the other polarity (see B_{LOS} in Fig. 3.6 (e)). The shape was inherited at the temperature minimum (1700 Å, see Fig. 3.6 (f)), the photosphere and transition region (1600 Å, see Fig. 3.6 (g)). In the chromosphere (304 Å, Fig. 3.6 (h)), the shape was less pronounced and was replaced by a far-extending fan structure. The study of propagating EUV disturbances in the coronal fan over this sunspot was presented in Yuan & Nakariakov (2012). We used a one-hour data set from 04:00 to 05:00 UT on 27 Oct 2011 in 1700 Å, 1600 Å and 304 Å. The instrumentation and data preparation are presented in Yuan & Nakariakov (2012). The cadence time was 24 s and 12 s for UV and EUV images, respectively.

3.3.2 Methods

Power map by Pixelised Wavelet Filtering

The Pixelised Wavelet Filtering (PWF) method was developed by Sych & Nakariakov (2008). It is based on the wavelet transform and is well validated in determining the spatial, temporal and phase structure of oscillations in an imaging cube $I_\lambda(x, y, t)$, where λ is the wavelength of the data channel, x, y and t are the discrete spatial locations and the measuring times, respectively. It gives the spatial distribution of the amplitude (power), frequency and phase of a signal in the spectral interval of interest.

For data sets $I_\lambda(x, y, t)$, we performed PWF analysis and obtained narrow-band power maps $P_\nu^\lambda(x, y)$ (or $P_p^\lambda(x, y)$, where $p = \nu^{-1} = 2, \cdots, 20$ min with the resolution of $\mathrm{d}p = 0.1$ min). In a sunspot, the power distribution normally forms a filled disk (short periods / high frequencies) or a power ring (long period / low frequencies) concentric at the sunspot centre (e.g. Sych & Nakariakov 2008; Reznikova et al. 2012). Therefore, to facilitate quantitative analysis, the power maps were transformed into a polar coordinate system with the origin coinciding with the sunspot centre $P_\nu^\lambda(r, \theta)$, where r is the distance to the sunspot centre, θ is the polar angle relative to the horizontal line pointing to the solar west (see Fig. 3.6 (a) and (e)).

For the power maps $P_\nu(r, \theta)$, the denotation λ is dropped to refer to the general case that is applicable to all wavelengths. We computed the maximum
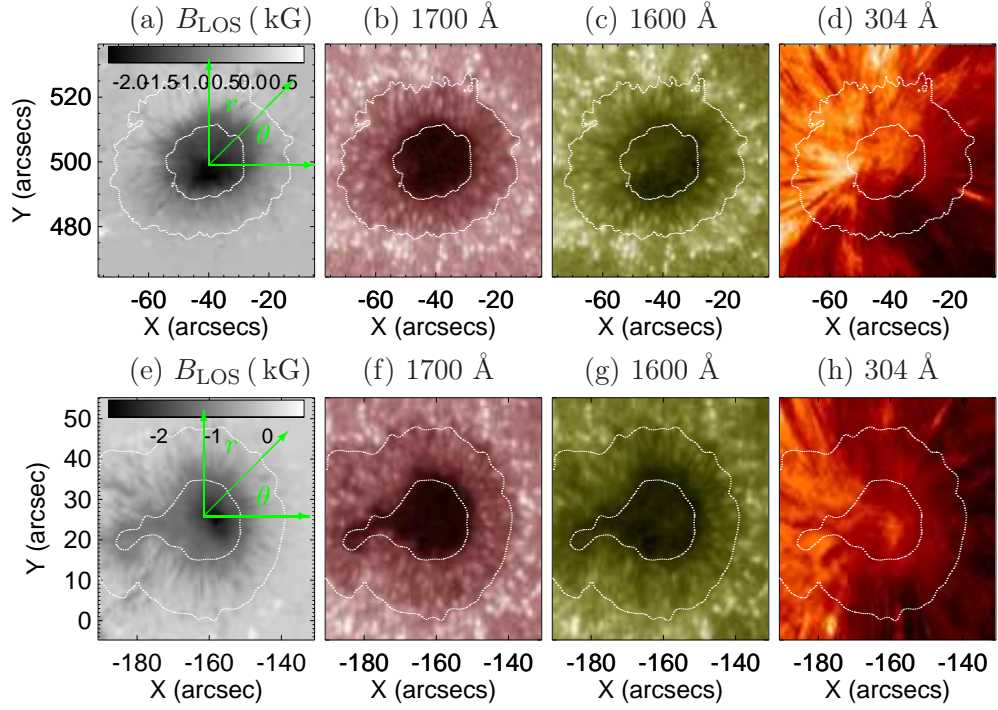
Figure 3.6: Multi-instrument imaging of AR 11131 (top, 08 Dec 2010) and AR 11330 (bottom, 27 Oct 2011) and the underlying sunspots at different heights. (a) and (e): The LOS magnetic field strength determined with HMI. The polar coordinate systems used in this study are overlaid. (b) - (d) and (f) - (h): AIA intensity images on logarithmic scales at different observational wavelengths show different levels of the sunspots and the associated active regions. In order of increasing heights of the observed levels, the displayed images illustrate the temperature minimum level (1700 Å), upper photosphere and transition region (1600 Å), and the chromosphere (304 Å). The dotted lines show the border of the sunspot umbra and penumbra determined with the 4500 Å image.

power at each location $P_{\max}(r, \theta)$ (see panel (a) in Fig. 3.8, Fig. 3.9 and Fig. 3.10). The corresponding peak period is $p_{\text{peak}}(r, \theta)$ (see panel (b) in Fig. 3.8, Fig. 3.9 and Fig. 3.10). The dependence of $p_{\text{peak}}(r, \theta)$ shows the spatial distribution of the period with the dominant oscillating power, while $P_{\max}(r, \theta)$ illustrates the significance of these oscillations. The variance of the spectral power over the spectrum for each pixel was also calculated, $\text{Var}(r, \theta) = \text{Var}(P_\nu(r, \theta))_\nu$[3] (see Fig. 3.8 (d)). This value is a good indicator of the significance of the signal at a specific location. To estimate the 1σ noise level, we took the average over the spectrum $\sigma(r, \theta) = \langle P_\nu(r, \theta) \rangle_\nu$ (see example in Fig. 3.8(e)). For the analysis of the symmetric sunspot, a further

---

[3]The subscript ν means the operation(s) along the spectral dimension. With the same philosophy, the subscripts θ and r mean the operation(s) along the polar angle dimension and radial distance dimension, respectively.

Table 3.2: Notations used in the work

Physical meaning	denotation
2D spectral power map	$P_\nu(r,\theta)$
2D spectral noise level	$\sigma(r,\theta) = \langle P_\nu(r,\theta)\rangle_\nu$
2D spectral power variance	$\mathrm{Var}(r,\theta) = \mathrm{Var}(P_\nu(r,\theta))_\nu$
2D spectral peak power	$P_{\max}(r,\theta) = \max(P_\nu(r,\theta))_\nu$
2D peak period	$p_{\mathrm{peak}}(r,\theta)$
2D MAG cut-off period	$p_{\mathrm{ac}}(r,\theta)$
2D MAG cut-off frequency	$\nu_{\mathrm{ac}}(r,\theta) = 1/p_{\mathrm{ac}}(r,\theta)$
1D spectral power map	$P_\nu(r) = \langle P_\nu(r,\theta)\rangle_\theta$
1D spectral noise level	$\sigma(r) = \langle P_\nu(r)\rangle_\nu$
1D spectral power variance	$\mathrm{Var}(r) = \mathrm{Var}(P_\nu(r))_\nu$
1D spectral peak power	$P_{\max}(r) = \max(P_\nu(r))_\nu$
1D peak period	$p_{\mathrm{peak}}(r)$ for all θ
1D MAG cut-off period	$p_{\mathrm{ac}}(r)$ for all θ
1D MAG cut-off frequency	$\nu_{\mathrm{ac}}(r) = 1/p_{\mathrm{ac}}(r)$
1D power spread	$s(r) = \mathrm{stdev}(P_\nu(r,\theta))_\theta\vert_{\nu=\nu_{\mathrm{ac}}}$

averaging over the polar angle θ was performed to reduce the θ dimension. Table 3.2 summarises the denotations and their physical meanings in both 1D and 2D cases.

Several typical narrow-band power maps obtained in 304 Å bandpass on 27 Oct 2011 are shown in Fig. 3.7. For the periods less than 3.2 min (frequencies greater than 5.2 mHz), the dominant power fills up the umbral region. The inhomogeneity of the power distribution implies a fine structure in the umbra (see the study in Jess et al. 2012, using imaging data with a resolution of 50 km/pixel in contrast to 430 km/pixel of AIA images). For the periods greater than 3.2 min, the power of significant oscillations is normally concentrated in an annular structure enclosing the umbra. The annulus expands with the increasing period. We interpret this phenomenon as modification of the cut-off frequency by the inclined magnetic field (Bel & Leroy 1977; De Pontieu et al. 2004, 2005; McIntosh & Jefferies 2006, also see discussions in Reznikova et al. (2012)). As the magnetic field lines approach the outer penumbra, the inclination angle becomes larger, therefore the cut-off frequency is lowered to a smaller value (Bel & Leroy 1977), and allows the channelling of upwardly propagating waves with lower frequency (longer period).

1D reconstruction in a symmetric sunspot (08 Dec 2010)

Reconstruction of field line inclination by MAG cut-off

For the symmetric sunspot AR 11131 (08 Dec 2010), we present an example of 304 Å data in Fig. 3.8. The distribution of the peak power $P_{max}(r,\theta)$ and the corresponding

74
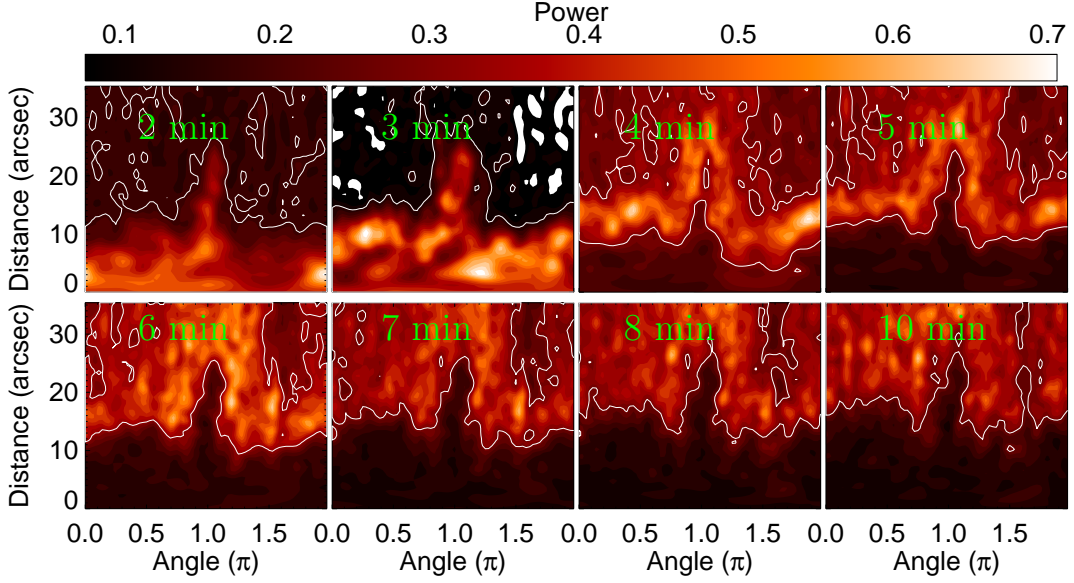
Figure 3.7: Typical narrow band power maps of 304 Å bandpass in polar coordinate made for 27 Oct 2011.

peak period $p_{\text{peak}}(r, \theta)$ are illustrated in Fig. 3.8 (a) and Fig. 3.8 (b), respectively. The dominant oscillating power fills in the umbra and gradually decreases further out in the penumbra and arcade region. In the umbra, the peak period is the well-known chromospheric 3–min oscillation (see review paper Bogdan & Judge 2006). It fills up the whole umbra and a tiny part of the penumbra. In the penumbra, the peak period gradually increases with the radial distance from the sunspot centre, indicating the modification of the cut-off frequency by inclined magnetic field lines. The variation with the polar angle is found to be very small. We averaged the power along the polar angles and obtained the normalised power $P_\nu(r)$ as a function of the distance to the sunspot centre, r, and the frequency ν, as shown in Fig. 3.8 (c). We defined the contour of the global median in $P_\nu(r)$ as the curve of the cut-off period $p_{\text{ac}}(r)$ (or frequency $\nu_{\text{ac}}(r) = 1/p_{\text{ac}}(r)$, see Fig. 3.8 (c)).

According to Bel & Leroy (1977), the MAG cut-off frequency in the low-β approximation is modified when the magnetic field line is inclined from the vertical direction, $\nu_{\text{ac}} = \nu_0 \cos \phi$. We estimated the inclination angle ϕ by

$$\phi(r) = \arccos \frac{\nu_{\text{ac}}(r)}{\nu_0} = \arccos \frac{p_0}{p_{\text{ac}}(r)} \tag{3.1}$$

where $\nu_0 = 5.2\,\text{mHz}$ ($p_0 = 3.2\,\text{min}$) is the acoustic cut-off frequency (period) (see Fig. 3.8 (f)).

Error and significance analysis

According to Eq. (3.1), the uncertainty of ϕ is calculated as

$$\Delta\phi(r) = \frac{\Delta\nu_{\mathrm{ac}}(r)}{\sqrt{\nu_0^2 - \nu_{\mathrm{ac}}{}^2(r)}} = \frac{\cos^2\phi}{\sqrt{1-\cos^2\phi}}\frac{\Delta p_{\mathrm{ac}}(r)}{p_0} \tag{3.2}$$

which requires the estimation of Δp_{ac}. This quantity can be assumed to be proportional to the noise level $\sigma(r)$, and the spread (standard deviation) of the spectral power over the polar angle $s(r)$. Δp_{ac} should also be inversely proportional to the maximum spectral power $P_{max}(r)$ and the square root of the number of the data points in polar angles, $\sqrt{N_\theta}$. The noise level $\sigma(r)$ is found to vary between 0.16 and 0.36. When we normalise it with its total median, it gives a factor between 0.52 and 1.13 to the uncertainty. We did the same to the spread $s(r)$ and obtained another factor between 0.31 and 1.4 added to the error bar. The value of $P_{max}(r)$ changes from 1 to about 0.4 with r, giving a factor from about 1 to about 2.5 to the total error bar. We choose a constant $\mathrm{d}p = 0.1\,\mathrm{min}$, the spectral resolution of PWF analysis, therefore the total uncertainty becomes

$$\Delta p_{\mathrm{ac}}(r) = \frac{\sigma(r)}{\mathrm{Med}(\sigma(r))}\frac{s(r)}{\mathrm{Med}(s(r))}\frac{\mathrm{d}p}{\sqrt{N_\theta}P_{\max}(r)}. \tag{3.3}$$

When the cut-off period approaches the detection limit (20 min in our application), the observation of the cut-off effect becomes less reliable. Applying this limit, we estimated the regions of significant measurements. We estimated the noise in the spectra as $\sigma(r,\theta) = \langle P_\nu(r,\theta)\rangle_\nu$. The noise level is illustrated in Fig. 3.8 (e). It was further averaged over the polar angles, $\sigma(r) = \langle P_\nu(r,\theta)\rangle_{\theta,\nu}$. The measurements with the noise level distributed above 68% (more than a standard deviation above the mean) of the noise are considered as less reliable (see the cross-hatched regions in all panels of Fig. 3.8). An alternative way is to consider the variance of the power maps, which reflects the contrast of the oscillating powers, giving us the significance of the measurements. We excluded 23% (lower than one standard deviation below the mean) of the smaller portion of the power variance distribution. As the results determined with either power variance or noise distribution are almost similar, we utilised only the results quantified by the noise level in the significance analysis.

2D reconstruction in an asymmetric sunspot (27 Oct 2011)

In 2D spectral power maps, we consider the areas with the spectral power above the median of the corresponding narrow-band power map as regions that allowed upward
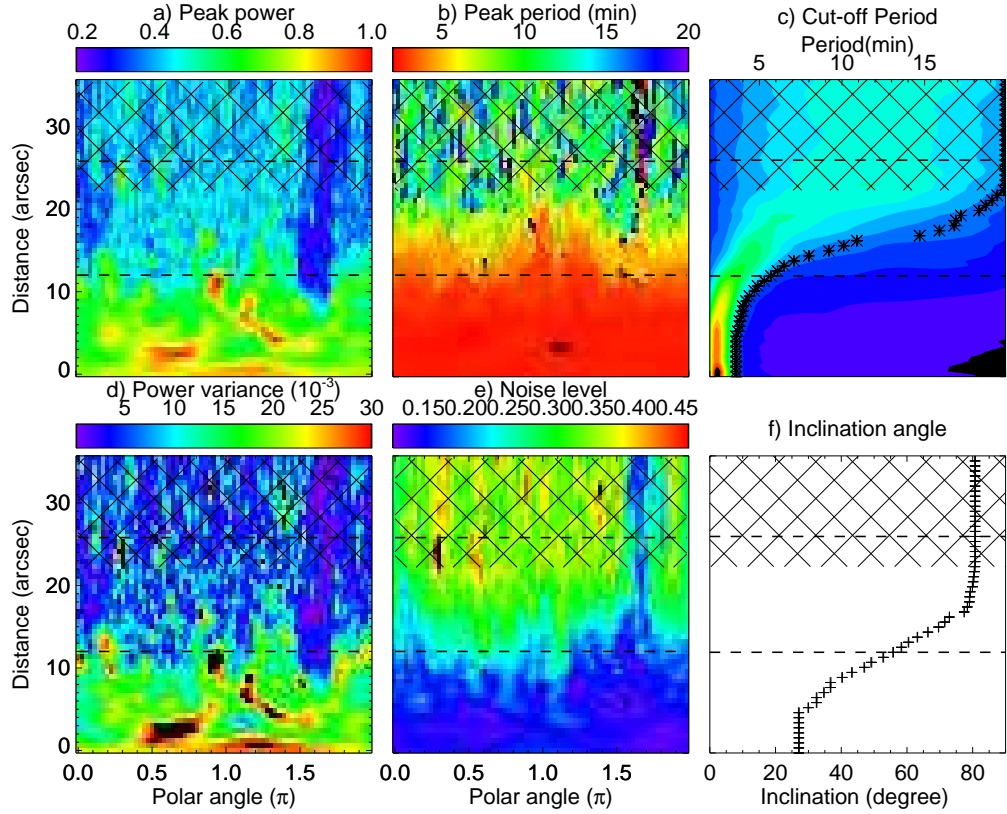
Figure 3.8: The oscillating power information extracted from the 304 Å data set of the sunspot AR 11131 (08 Dec 2010), shown in the polar coordinates (r and θ). The dashed lines mark the borders of the umbra and penumbra. The unreliable region is cross-hatched. a) The peak power distribution. b) The peak period distribution. c) The 1D spectral power map as a function of r and p. The contour in asterisk shows the cut-off period. d) The spectral power variance distribution. e) The spectral noise distribution. f) The reconstruction of the magnetic field inclination.

propagating MAG waves. The borders of these areas were defined as contours of the MAG cut-off. By labelling the cut-off contours, we were able to reconstruct the field line inclination.

The reconstruction steps are similar to those in the 1D case. The estimation of the error, $\Delta p_{\mathrm{ac}}(r, \theta)$, is simplified,

$$\Delta p_{\mathrm{ac}}(r, \theta) = \frac{\sigma(r, \theta)}{\mathrm{Med}(\sigma(r, \theta))} \frac{\mathrm{d}p}{P_\nu(r, \theta)} \tag{3.4}$$

We masked out the regions with the less significant measurements. The masks were designed with two criteria: 1) the pixel should be within the penumbra and umbra; 2) the noise level in that pixel should not exceed the 68% level in
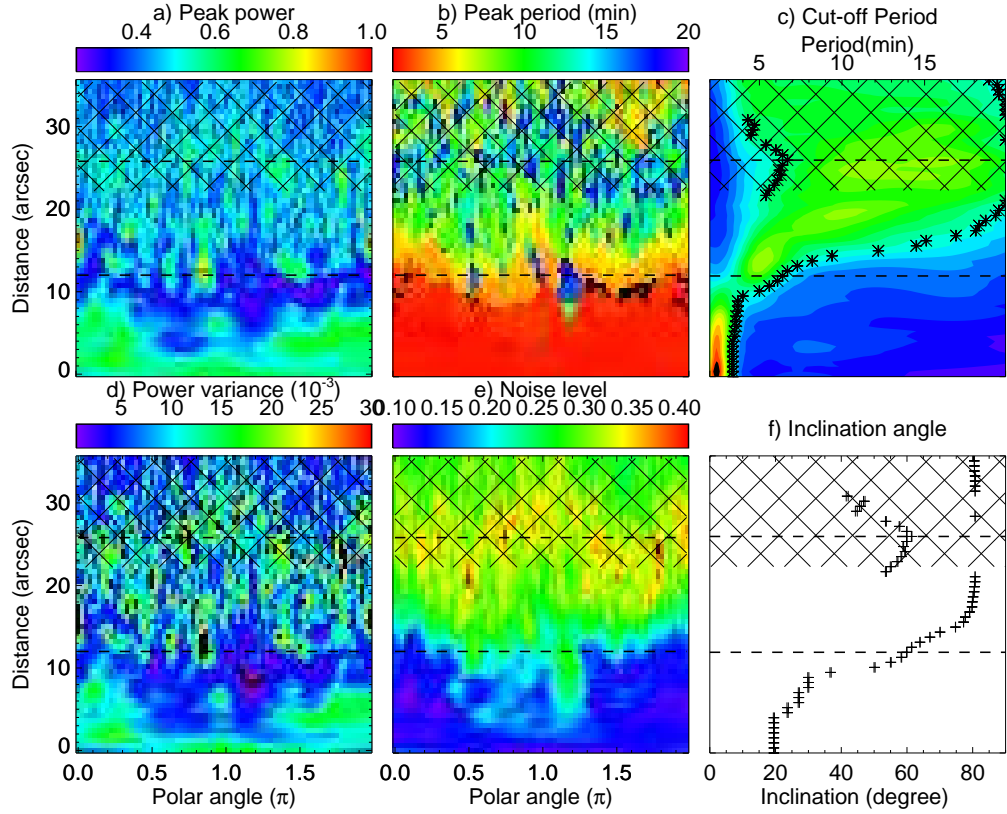
Figure 3.9: The same as Fig. 3.8 but in 1600 Å

$\sigma(r, \theta)$ distribution. Only the measurements within the mask are shown in Fig. 3.11, Fig. 3.12 and Fig. 3.13

Magnetic field extrapolation

We compare the field reconstruction with 3D magnetic field extrapolation. Potential (current-free) fields were extrapolated using the MAGPACK2 package (Sakurai 1982). The current-free model in this code is based on the Green's function method and requires a line-of-sight magnetogram as the bottom boundary condition. Although, we cannot *a priori* exclude the presence of the electric currents in the considered volume, we have chosen this model because of the following reasons: 1) both of ARs did not produce any flares within or close to our observational intervals; 2) we are interested in field structures in the layers below the corona where the dense material can influence the field inclination. Therefore, the choice of the non-potential field is unlikely to produce better approximation at these heights.

Fig. 3.14 presents a 2D projection of reconstructed magnetic field lines overlaid on the photospheric line-of-sight magnetogram (a) sunspot AR 11131 (08 Dec
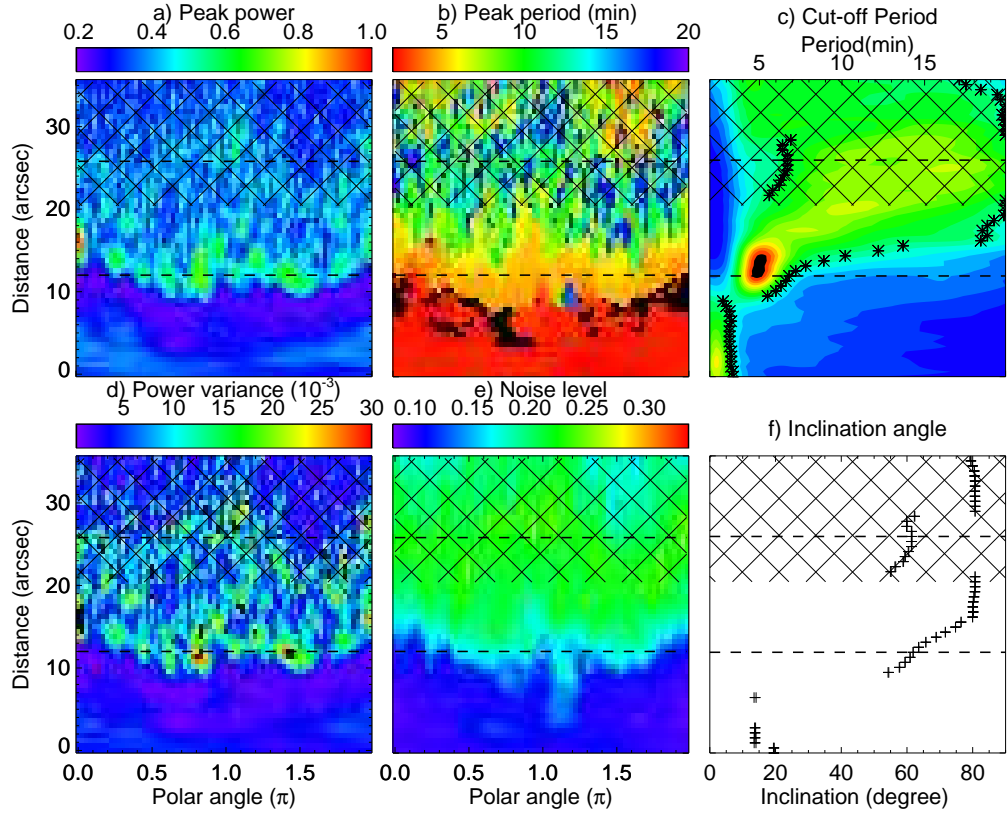
Figure 3.10: The same as Fig. 3.8 but in 1700 Å

2010) and (b) sunspot AR 11330 (27 Oct 2011). The colour coding represents the magnetic field strength, using blue for southern (negative) and red for northern (positive) polarities. For the sunspot AR 11131, we selected sub-area of $160'' \times 160''$ from the SOHO/MDI full-disk magnetogram taken at 04:51 UT, as shown in Fig. 3.14(a). For the sunspot AR 11330, the HMI line-of-sight magnetogram was obtained as a level-1.5 FITS file. A larger size of $300'' \times 300''$ was selected to include the sufficient amount of positive polarity following the main sunspot. The magnetic field was computed with a $2''$ mesh spacing using a spherical boundary.

3.3.3 Results

Spatial and height distribution of dominant oscillations

Based on the 1D power distribution, panel (c) of Fig. 3.8, Fig. 3.9 and Fig. 3.10, it is clearly seen that 3-min oscillations are very strictly constrained within the umbral region, while 5-min oscillations dominate only at a thin annulus (about 2.9 - 5.0 Mm in width) between the umbra and penumbra. Although 3-min oscillation

is strongest in the umbra, it is predominant within the disks of radii about 2.1, 5.8 and 7.2 Mm in the 1700 Å (temperature minimum), 1600 Å (upper photosphere) and 304 Å (chromosphere) data, respectively. Although 3-min oscillation can propagate through both vertical and inclined magnetic field, it is constrained only in the umbra. This implies that the 3-min oscillation is not likely to originate from the solar interior. Instead, it is consistent with the acoustic resonator model (Zhugzhda 2008; Botha et al. 2011). The 5-min oscillation is well pronounced in the 1700 Å data. It appears that there is strong interaction between the magnetic fields and the ambient plasma enclosing the sunspot umbra, where the magnetic field is medium in strength and slightly inclined and has a strong longitudinal gradient. It seems there is strong p-mode absorption at the umbra border. The maximum energy transmission was predicted to occur at the height where the Alfvén speed is approximately equal to the local sound speed and at an attack angle of about 30° (Cally et al. 2003; Schunker & Cally 2006). Thus the 5-min oscillation may form at the temperature minimum (about 500 km above the photosphere). The 2D power maps also confirm these results, see panels a) and b) in Fig. 3.8, Fig. 3.9, Fig. 3.10, Fig. 3.11, Fig. 3.12 and Fig. 3.13. In panel (a) of Fig. 3.8 and Fig. 3.11, the power of 3-min oscillations show variations within the umbra. This implies fine structuring inside the umbra. Stronger sources of oscillations were found better correlated with the 3-min propagating disturbances in the corona loops in the 171 Å bandpass (Jess et al. 2012; Sych et al. 2012).

Correlation of the peak and cut-off frequencies

The detected cut-off frequencies are plotted versus the corresponding peak frequencies, see Fig. 3.15. ν_{ac} was almost constant as ν_{peak} varied between 1.5 and 3.0 mHz. Then a sharp rise of ν_{ac} was found as ν_{peak} increased from 3.0 to 3.5 mHz. This effect was more apparent in the lower atmosphere (1700 Å), but rather less significant in higher atmosphere (304 Å). As ν_{peak} approached 3.5 mHz or higher values, a very good linear increase in ν_{ac} was found. The correlation between them is very high: the Pearson's correlation coefficients R are 0.996, 0.993 and 0.995 for the 1700 Å, 1600 Å and 304 Å data, respectively. We fitted a linear relationship ($\nu_{ac} = a\nu_{peak} + b$) to the data with ν_{peak} greater than 3.5 mHz using the MPFITEXY routine [4] (Williams et al. 2010). The MPFITEXY routine depends on the MPFIT package[5] (Markwardt 2009). The slopes are 0.65 ± 0.03, 0.64 ± 0.05 and 0.81 ± 0.03 for the 1700 Å, 1600 Å and 304 Å data, respectively. The result slightly

---

[4]http://purl.org/mike/mpfitexy
[5]http://cow.physics.wisc.edu/ craigm/idl/idl.html

deviated from the empirical relation ($\nu_{\mathrm{peak}} \simeq 1.25\nu_{\mathrm{ac}}$) between the peak and cut-off frequency as suggested in Bogdan & Judge (2006); Tziotziou et al. (2006), except the value obtained in the 304 Å data. Moreover we obtained non-zero intercepts in the linear fits, $0.57 \pm 0.18\,\mathrm{mHz}$, $0.39 \pm 0.34\,\mathrm{mHz}$ and $-1.0 \pm 0.18\,\mathrm{mHz}$ for 1700 Å, 1600Å and 304 Å, respectively (see Fig. 3.15).

Reconstruction of the magnetic field inclination

As described in Sec. 3.3.2, the results of 1D reconstruction are illustrated in Fig. 3.8 (304 Å), Fig. 3.9 (1600 Å) and Fig. 3.10 (1700 Å). Comparison of our results obtained with the seismological technique with the potential field extrapolation is shown in Fig. 3.16. The inclination angles were retrieved at 500 km (1700 Å), 1100 km (1600 Å) and 2200 km (304 Å) above the solar surface. The magnetic inclination was estimated with both the theoretical acoustic cut-off frequency $\nu_0 = 5.2\,\mathrm{mHz}$ and the corresponding observationally determined cut-off frequency ν_0^λ, where the index λ corresponds to the observational channel used in its determination.

Fig. 3.16 shows clearly that the general profiles of field inclinations reconstructed with the MAG cut-off at 1600Å, 1700 Å and 304 Å, agree very well with the potential field extrapolation in the region from $0.2r_{\mathrm{p}}$ to $0.8r_{\mathrm{p}}$, where r_{p} is the average radius of the penumbra. The average offsets are 32.7/28.8, 27.9/26.6, 30.9/29.7 for ν_0/ν_0^λ reconstructions in 1700 Å, 1600 Å and 304 Å, respectively. The results are slightly improved by using the observed maximum cut-off frequency, but the large offsets cannot be fully removed. This implies that the inclined magnetic field is not the only factor that influence the MAG cut-off frequency, it only accounts for 60-80% of the lowering in the cut-off frequency. In the inner umbra (from 0 to $0.2r_{\mathrm{p}}$), the deviations from the potential field extrapolation are about $20^\circ - 30^\circ$. These deviations may arise from using a constant ν_0; choosing the observed ν_0^λ for the corresponding bandpass appears more realistic. We obtained a flat distribution in all bandpasses in the inner umbra. It implies that the wave characteristics inside the inner umbra may be different from other regions of the sunspot, or that the impact of the plasma temperature needs to be considered as well. We notice that at $0.8r_{\mathrm{p}}$-$1.2r_{\mathrm{p}}$ in the 1600 Å and 1700 Å data, a region of low inclination was obtained. In our method, $\cos(\pm\phi) = \left|\cos(180^\circ \pm \phi)\right|$ can not be differentiated (the 180° ambiguity problem, see Metcalf et al. 2006). By considering this effect, this low-inclination region in the penumbra border can be connected with the return-flux region with the magnetic vector pointing downwards, instead of upwards. The green asterisk denotes the return flux in the potential magnetic field corrected into $[0^\circ, 90^\circ]$. The results are consistent with the values estimated with the use of the MAG cut-off, both in the

inclination and the distance to the sunspot centre. Such behaviour is consistent with the return-flux sunspot model (Fla et al. 1982; Osherovich 1982). The return-flux region is found to spread at about $0.8r_\mathrm{p}$- $1.2\ r_\mathrm{p}$. If we assume a parabolic shape of the magnetic field lines, the returning flux at about $0.4r_\mathrm{p}$-$0.6\ r_\mathrm{p}$ extends to the height of about $0.14\ r_\mathrm{p}$- $0.26\ r_\mathrm{p}$ and returns to the surface about 0.4 - 0.6 r_p apart from the source. This effect is less pronounced in the 304 Å data, in which the magnetic field shows a steady extension outwards the sunspot. The agreement between the inferred magnetic inclination and the values obtained with the potential field extrapolation is better in the return-flux region compared with the inner sunspot region. The return fluxes were normally found at the periphery of the sunspot penumbra with a weaker magnetic field and higher temperature, so we infer that other effects, e.g. radiative cooling, should be accounted as well to understand the lowering of the MAG cut-off frequency.

In 2D reconstruction, we compare the reconstructed magnetic field inclination, panel (e) of Fig. 3.11, Fig. 3.12 and Fig. 3.13, with the potential field extrapolation shown in Fig. 3.17. Our method reconstructed the magnetic inclination distribution: both the global profiles, fine structure inside the sunspot umbra and the protrusion at the penumbra. In the 1600 Å and 1700 Å data, the return flux is reconstructed very well. It appears that in 2D geometry, no apparent physics modified the result, except the morphology. The potential field extrapolation reflects the general profiles, including the protrusion structure and the return flux. The average offsets are larger, 41.0, 37.8 and 37.0, which may arise from the error accumulation, since the outliers cannot be effectively excluded.

3.3.4 Conclusions

We observed the 3D structure of the variations of compressive oscillation periods in two sunspots. Our results confirm the previous findings that short-period (high-frequency) oscillations are constrained inside the sunspot umbra, while long-period (low-frequency) oscillations are mainly present outside the umbra. Longer the period is, further away the oscillations are observed from the sunspot centre. The predominant oscillation inside the umbra is the well-known 3-min oscillation. The variation over different heights indicates that the 3-min oscillation is not sourced from the solar interior, rather it is more consistent with the acoustic resonator model (Zhugzhda 2008; Botha et al. 2011). The 5-min oscillations form a ring-shape at the umbra border. We may speculate that the strong power of 5-min oscillations may indicate strong interaction of acoustic waves with the magnetic field, where the local condition favoured the absorption of global solar p-modes (Cally et al. 2003; Schunker &

Cally 2006).

We seismologically reconstructed the magnetic field inclination with the use of the Bel & Leroy (1977) formalism, and found its results to be consistent with the results obtained with potential field extrapolation. It confirmed the conclusion in Bel & Leroy (1977) that the inclined magnetic field lowers the cut-off frequency. The MAG-reconstructed magnetic inclinations are generally larger than the potential field extrapolation. The small discrepancy may be attributed to the other effects, e.g. radiative cooling (Centeno et al. 2006, 2009; Felipe et al. 2010). The effect of the magnetic field inclination accounts for about 60-80% of the lowering in the cut-off frequency. The seismological method applied in our study provides an alternative way to reconstruct the magnetic field. Moreover, it may provide the boundary or initial conditions for the magnetic field extrapolation.

In our method, we assumed $\beta \ll 1$, which may be incorrect in some parts of the sunspots. The method can be improved by considering an observational or empirical β profiles at various heights of the sunspots. If the 3D magnetic field vector field is available, the magnetic field strength and inclination can be calculated, we are able to reconstruct the sound speed and local temperature profiles in both 1D and 2D at various heights.
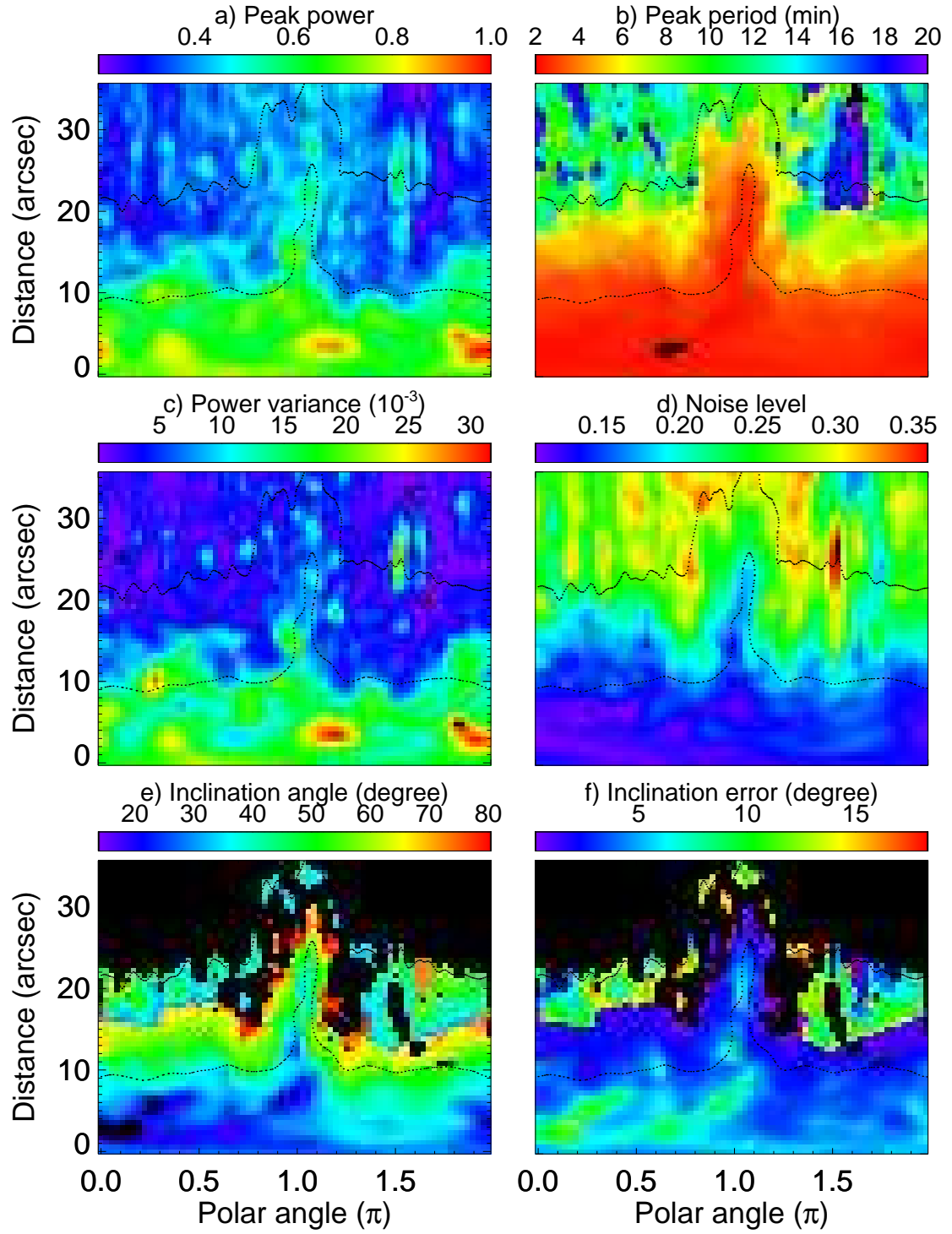
Figure 3.11: a) - d) are the same as a), b), d) and e) in Fig. 3.8. e) and f) are the inclination angle and its uncertainty reconstructed in 2D.
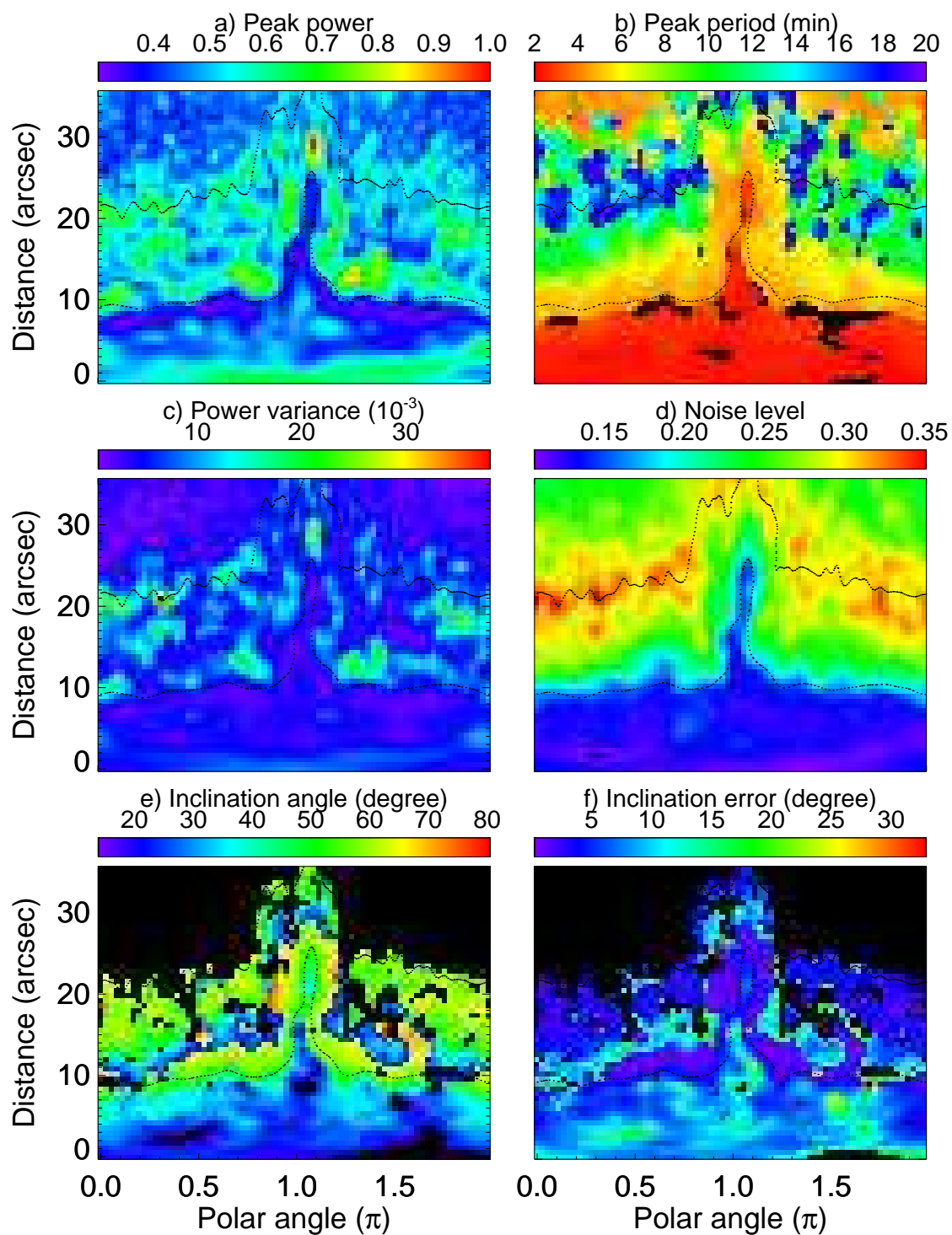
Figure 3.12: The same as in Fig. 3.11 but in 1600 Å
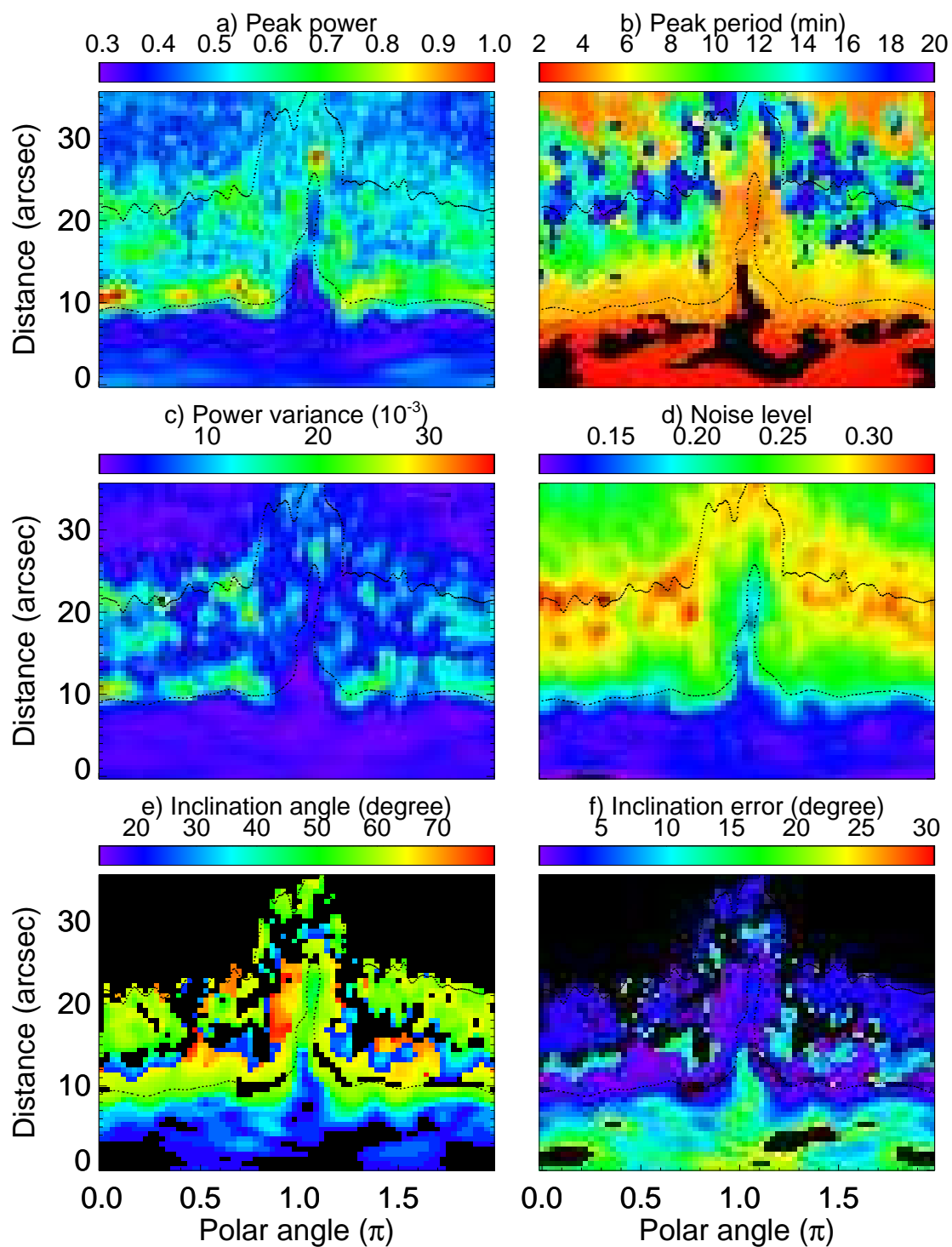
Figure 3.13: The same as in Fig. 3.11 but in 1700 Å
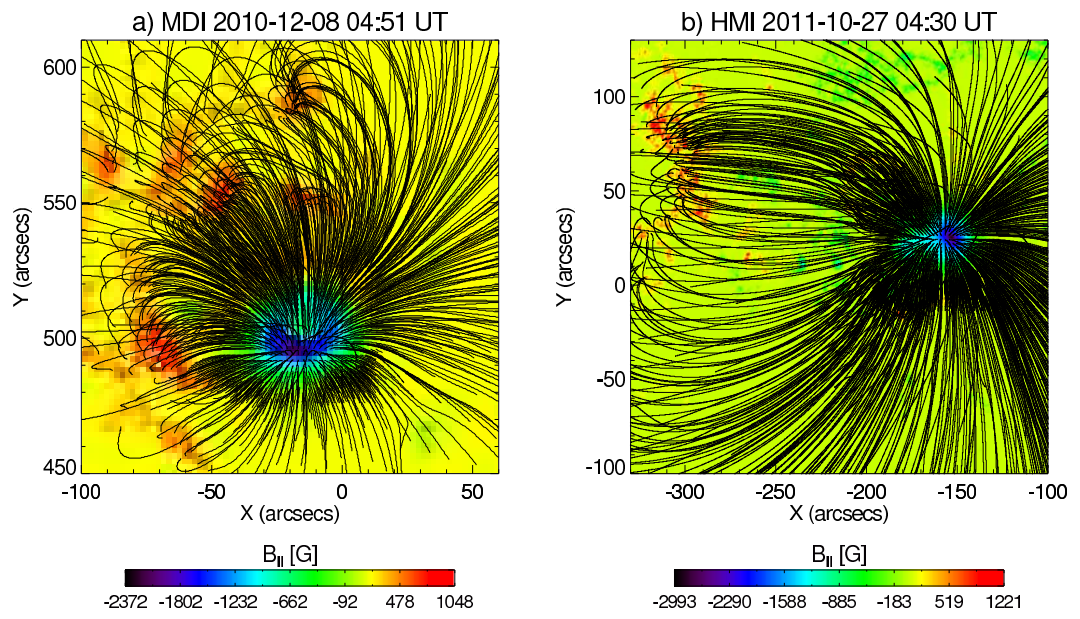
Figure 3.14: Results of the potential field extrapolation using the MDI magnetogram for sunspot AR 11131 on 08 Dec 2010 (a) and with the HMI magnetogram for sunspot AR 11330 on 27 Oct 2011 (b).
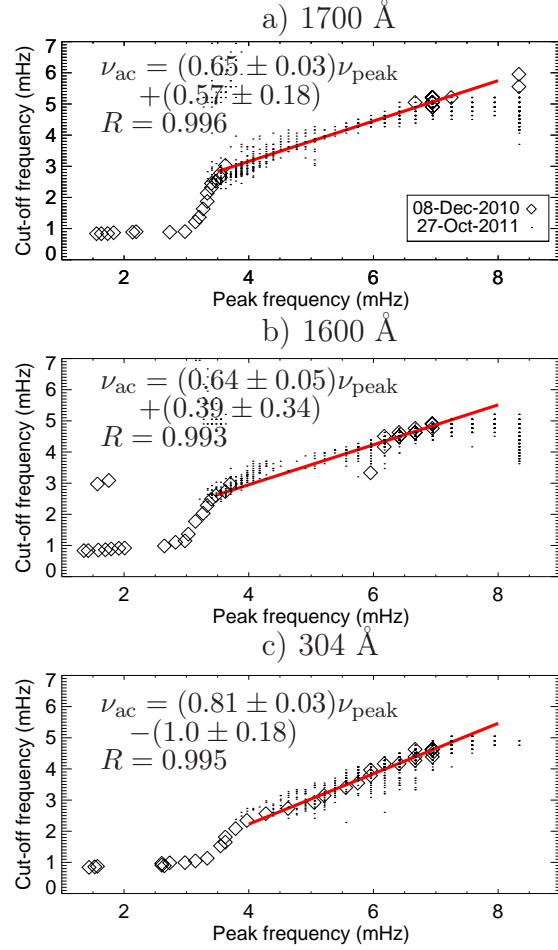
Figure 3.15: Correlation between the cut-off frequency and peak frequency for 1700 Å (a), 1600 Å (b) and 304 Å (c) data. The diamond symbols represent the measurement at sunspot AR 11131 observed on 08 Dec 2010, while dot symbols indicate the data of sunspot AR 11330 observed on 27 Oct 2011. The data are fitted with a linear relationship $\nu_{\mathrm{ac}} = a\nu_{\mathrm{peak}} + b$, as plotted in red solid line. The fit parameters, as well as the Pearson's correlation coefficient, are displayed in each panel.
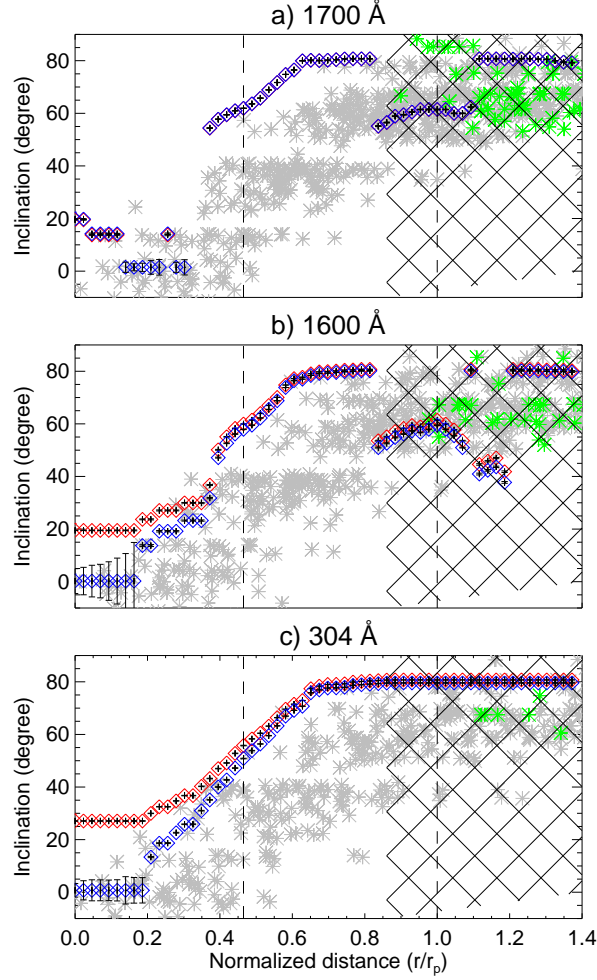
Figure 3.16: Comparison of magnetic field inclination reconstructed by magneto-acoustic cut-off with potential field extrapolation for sunspot AR 11131 (08 Dec 2010) in 1700 Å (a), 1600 Å (b) and 340 Å (c) bandpasses. The inclination angles obtained with the potential field extrapolation are represented in grey asterisk as the scatter plot, while the data in green asterisks denote the absolute values of inclinations of the return flux. The inclination angles reconstructed with $\nu_0 = 5.2\,\mathrm{mHz}$ are plotted in the red diamonds, while those reconstructed with the observational maximum cut-off frequency ν_0^λ are plotted in blue diamonds. The dashed lines show the border of the sunspot umbra and penumbra. The cross-hatched region marks the measurements below the significant level.
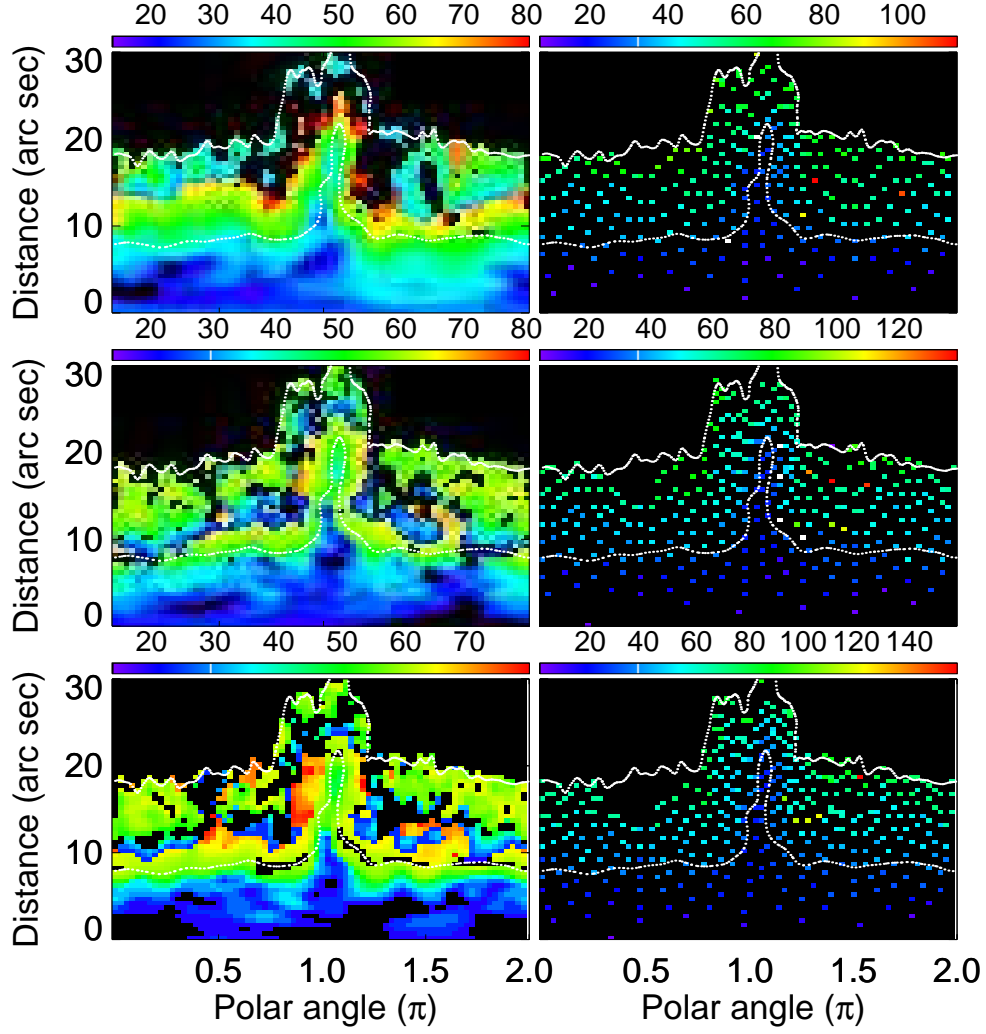
Figure 3.17: Left column: magnetic field inclination obtained with ν_0 reconstruction. Right column: the inclination angle obtained from potential field extrapolation for AR 11330 on 27 Oct 2011. From top to bottom rows, the panels correspond to 304 Å, 1600 Å and 1700 Å data. The dotted lines mark the umbra and penumbra borders.

Chapter 4

Characteristics of propagating EUV disturbances

4.1 Introduction

Propagating extreme ultraviolet (EUV) intensity disturbances were discovered in the solar polar plumes (Deforest & Gurman 1998) and coronal loops (Berghmans & Clette 1999) with the Extreme ultraviolet Imaging Telescope (EIT) onboard the SOlar and Heliospheric Observatory (SOHO). The follow-up studies (e.g. Ofman et al. 1999; De Moortel et al. 2000, 2002c,a; Robbrecht et al. 2001; King et al. 2003; Marsh et al. 2003; De Moortel 2009) were carried out with or in combination with the Transition Region and Coronal Explorer (TRACE, see Handy et al. 1999), which observed a part of the Sun with a better resolution, 0.5 arcsec/pixel in contrast to the 2.6 arcsec/pixel of SOHO/EIT. The propagating speeds, observed as the apparent speed projected to the image plane perpendicular to the line-of-sight (LOS) of the imagers, were normally found to be lower than the local sound speed (which can be estimated as $\simeq 152\sqrt{T[\mathrm{MK}]} \approx$ 150-260 km/s for the temperature T from 1 MK to 3 MK). A stereoscopic observation with the Extreme Ultraviolet Imager (EUVI, A and B) on the Solar TErrestrial RElations Observatory (STEREO) revealed that the phase speed was well consistent with the sound speed inferred from the temperature measure (Marsh et al. 2009). The propagating EUV disturbances are usually interpreted as propagating slow magnetoacoustic waves (Nakariakov et al. 2000; De Moortel 2006; Verwichte et al. 2010). ITheir wave nature was additionally confirmed by joint observations of intensity (density) and Doppler shift (velocity) oscillations with the EUV Imaging Spectrometer (EIS) on Hinode (Wang et al. 2009a,c; Mariska & Muglach 2010).

The amplitude of propagating EUV disturbances is normally found to be ~1-10% of the background intensity (De Moortel et al. 2002c). The low-amplitude disturbances were found to be satisfactorily modelled in the linear approximation (Nakariakov et al. 2000). The amplitude is observed to damp very quickly, typically within 2.9–23.3 Mm (1–2 visible wave fronts) along the wave path (De Moortel et al. 2002c). Thermal conduction appears to be the dominant damping mechanism (De Moortel & Hood 2003; Ofman & Wang 2002; Klimchuk et al. 2004). The energy flux carried by the EUV propagating disturbances was estimated to be far too insufficient to contribute significantly to coronal heating (Ofman et al. 2000a; De Moortel et al. 2002c).

Propagating EUV disturbances are usually quasi-monochromatic with the periods categorised into two classes: the short period (~3-5 min, see De Moortel et al. 2000, 2002c,a; De Moortel 2009; King et al. 2003; Marsh et al. 2003; Wang et al. 2009a) and long period (~10-30 min, see Berghmans & Clette 1999; McIntosh et al. 2008; Marsh et al. 2009; Wang et al. 2009c; Yuan et al. 2011). De Moortel et al. (2002c) found statistically that the 3 min oscillations are more likely to be detected above sunspot regions, while the 5 min oscillations are usually found off the sunspots (e.g. above the plage region). This feature suggests the likely association of the coronal propagating disturbances with chromospheric 3 min oscillations and the photospheric 5 min oscillations, respectively. Chromospheric 3 min oscillations were found to leak from sunspot umbrae to the corona (Shibasaki 2001; Sych et al. 2009; Botha et al. 2011). Photospheric 5-min oscillations in plage regions are apt to be wave-guided to the corona by inclined magnetic field lines (Bel & Leroy 1977, and Sec. 1.2.3), and could be associated with the leakage of global p-modes from the photosphere (De Pontieu et al. 2005). Long-period oscillations are detected often in the corona as well, but the possible source remains poorly understood (see discussions in Yuan et al. 2011, and Chapter 6).

There are also observations of cases with multiple periods (Mariska & Muglach 2010; Wang et al. 2009c). Wang et al. (2009c) detected two harmonics in 12 and 25 min with EIS/Hinode and found that the detection lengths (70 -90 Mm) of the long-period oscillations are much longer than previous TRACE studies (e.g. De Moortel et al. 2002c). This result is in agreement with the period-dependency of the damping length of slow magnetoacoustic wave decaying due to thermal conduction mechanism.

The apparent phase speed was measured at tens to hundreds of km/s (De Moortel et al. 2002c; De Moortel 2009). The spread of the measured speeds is usually attributed to the variation of the angle between the propagating direction and image plane in different cases. Robbrecht et al. (2001) reported that the phase

speeds of propagating disturbances measured in TRACE 171 Å (1 MK) are normally lower than those measured in EIT 195 Å (1.6 MK). The temperature-dependence of the phase speed was recently found in polar plumes and the inter-plume medium with AIA (Krishna Prasad et al. 2011). In some cases, acceleration of the disturbances was detected at larger heights (typically above ∼20 Mm, see Banerjee et al. 2011, for a review).

Joint imaging and spectroscopic investigations revealed that the Doppler velocity oscillates in phase with the intensity (density) perturbation at the footpoints of active region loops (Wang et al. 2009a,c; Mariska & Muglach 2010), this is consistent with the slow magnetoacoustic wave theory (see Nakariakov et al. 2000; Tsiklauri & Nakariakov 2001). Recent spectrometric studies observed the blue-wing asymmetry in the emission spectral lines at the footpoints of coronal fan structure, and hence, the propagating disturbances were interpreted as periodic upflows (e.g., Doschek et al. 2007, 2008; Sakao et al. 2007; Del Zanna 2008; Harra et al. 2008; Hara et al. 2008; De Pontieu & McIntosh 2010; Tian et al. 2011a,b; Martínez-Sykora et al. 2011). A single Gaussian fit to the spectral lines suggest that the flow speed is about ∼10 km/s, much less than the observed apparent speed of propagating disturbances. Tian et al. (2011b) implemented a guided double-Gaussian fit to the spectral lines and found that the emission-line width could be associated with two components. The secondary component contributes a few percent of the total emission, its blueward asymmetry is associated with flows of speed of 50-150 km/s. The faint secondary component modulates the peak intensity, line centroid and line width quasi-periodically, therefore propagating disturbances can be observed consistently (De Pontieu & McIntosh 2010; Tian et al. 2011b). A similarity was reported between the spatial distribution of flow speed observed with Hinode/EIS and the temporal distribution of the speed of propagating disturbances observed with SDO/AIA (Tian et al. 2011b). On the other hand, the blue-wing asymmetry was found to be an intrinsic feature of upward propagating slow magnetoacoustic waves (Verwichte et al. 2010).

The typical method for studying coronal propagating disturbances is the so-called time-distance plot. In each image, a cut is taken following the direction of propagation, $F(x_i, y_j, t_k)$, where x_i and y_j are the image pixel coordinates, t_k is the time frame index. The time-distance array $C(s_m, t_k)$, where s_m is the index along the cut, is made by stacking the cuts in order of time. Propagating disturbances of the emission intensity are featured by diagonal ridges in the plot of the time-distance array (a time-distance plot). The visibility of the ridges is normally fairly poor, since EUV disturbances are weak, normally $\lesssim 10\%$ of the background intensity, and of

the same order of magnitude with the data noise. A simple and well-implemented technique, the running difference, can be applied to a time-distance plot to enhance the contrast (visibility) of the propagating disturbances. The running difference is obtained by subtracting from the cut $C(s_m, t_k)$ the value of another cut $C(s_m, t_{k-l})$ taken in the lth image ahead of the current one $R(s_m, t_k) = C(s_m, t_k) - C(s_m, t_{k-l})$. The slope of the ridges in the running distances relative to the time axis is the apparent (projected) phase speed of the propagating disturbances. Another way to enhance the visibility is to remove the quasi-static background from the image, and normalise the residue with it. The background can be obtained by temporal averaging $B(s_m, t_k) = \sum\limits_{h=-N/2}^{N/2-1} C(s_m, t_{k+h})/N$, where N is the number of time frames. Thus, a time-distance array with background-removal and normalisation is obtained by $D(s_m, t_k) = [C(s_m, t_k) - B(s_m, t_k)]/B(s_m, t_k)$. We refer generally hereafter to the enhanced time-distance plot $X(s_m, t_k)$ as either the time-distance array made by the running difference $R(s_m, t_k)$ or the background-subtracted and normalised array $D(s_m, t_k)$.

Although a number of measurements were made on the phase speed (see De Moortel et al. 2002c,a; De Moortel 2009), no method was designed to quantify and standardise the measurement, to remove human-based bias and to make the measurements consistently comparable. The aim of this chapter is to design rigorous methods for measuring the apparent phase speed of propagating disturbances in coronal imaging data, and compare their performance by the analysis of coronal propagating disturbances observed with AIA.

We describe the data pre-processing and the observation dataset in Sec. 4.2.1; the methods for phase speed measurement are detailed in Sec. 4.2.2; the results are summarised in Sec. 4.2.3; the conclusion is made in Sec. 4.2.4.

4.2 Phase speed measurement

4.2.1 Dataset

We used the observational dataset over a very quiescent active region (NOAA 11330) in the 171 Å bandpass at 04:00 - 08:00 UT on 27 Oct 2011. No flare occurred during the observation time interval that the active region was gradually approaching the centre of the solar disk. The leading eastern part of the active region formed a fan-like feature (see Fig. 2.4(a)) that consisted of both closed and open plasma structures. Continuous propagating EUV disturbances were observed following the fan-like feature.

A four-hour dataset was downloaded as a cutout data of level 1 and prepared into level 1.5 as described in Sec. 1.1.6. A typical image is displayed in Fig. 2.4. The cadence time was very uniform, 12.000 ± 0.006 s, the exposure time was 1.9996052 ± 0.0000038 s, the total number of images in 171 Å was 1200. We truncated the size of the dataset into an array $F(x_i, y_j, t_k)$, a set of 1200 images of 100×100 pixels, so that the fan-like structure becomes the only prominent morphological feature in the images. The images were corrected for the solar differential rotation and further co-aligned with the offsets calculated by 2D cross-correlation. The morphology of the images did not change much during the observations, either geometrically (shape) or photometrically (intensity), so the co-alignment reached a fairly good accuracy of sub-pixel.

Propagating EUV disturbances are visible along most of the strands in the fan that extends from the footpoint. We took a cut (41 pixels, ~17.7 Mm) in every image starting from the footpoint and following the coronal structure extended from the west to the east (see Fig. 2.4). The intensity of each pixel in each image was averaged over three pixels in the vertical direction. The running difference was made with $R(s_m, t_k) = C(s_m, t_k) - C(s_m, t_{k-9})$ ($T_{\text{lag}} = t_k - t_{k-9} = 9 \times 12 = 108$ s). The running difference plot is shown in Fig. 2.4(b). The background-subtracted normalised time-distance plot $D(s_m, t_k)$ was obtained by estimating the background with $N = 50$ smoothing ($T_{\text{detr}} = 50 \times 12 = 10$ min) and is illustrated in Fig. 2.4(c). The propagating EUV disturbances are featured by the repeating diagonal ridges in the time-distance plot (~10 cycles during a 30-min observation). The EUV disturbances are gradually damped with height (or are buried in noise) after ~17.7 Mm along the slit. The gradient of the ridges relative to the time axis is the phase speed of EUV disturbances, projected to the image plane perpendicular to the LOS. The typical observables and physical parameters of the propagating disturbances are summarised in Table 4.1.

We measured the average apparent speed in the enhanced time-distance plot $X(s_m, t_k)$ with either a full (41 pixels, both the prominent part and relatively noisier part) set of pixels or its lower half (20 pixels, only the prominent part), see Fig. 2.4(b). We prepared the enhanced time-distance plots of two sizes 41×150 and 20×150 pixels (referred to hereafter as R_1 and R_2, consequently, and R for running difference, either R_1 or R_2; D_1, D_2 and D are their analogues taken from the background-subtracted and normalised time-distance plot.) R_2 (D_2) is the first half of R_1 (D_1) between 0 and 8.6 Mm along the slit, see Fig. 2.4(a). The quality of $X(s_m, t_k)$ is quantified by two parameters: the amplitude ratio of the propagating waves and the data noise $\langle A_{\text{w}} \rangle / \langle A_{\text{n}} \rangle$, and the amplitude ratio of the propagating waves and the background

Table 4.1: Observables and physical parameters of the analysed propagating EUV disturbances

Parameters	Values
Date of observation	27 Oct 2011
Time interval of the observation	04:00:00-08:00:00 UT
Time interval of the samples	04:30:01-05:00:01 UT
Active region number	NOAA 11330
Location of the active region	[-160″, 30″]
Oscillation period p	$\simeq 179\,\mathrm{s}\ (\simeq 3\,\mathrm{min})$
Apparent phase speed V_p	$\simeq 48\,\mathrm{km/s}$
Spatial wave number k	$\simeq 0.74\,\mathrm{Mm}^{-1}$
Detection distance	~17.7 Mm
Number of visible wave fronts	2
$\langle A_{\mathrm{w}} \rangle / \langle A_{\mathrm{b}} \rangle (R)$	~1.4%
$\langle A_{\mathrm{w}} \rangle / \langle A_{\mathrm{n}} \rangle (R)$	~3.4
$\langle A_{\mathrm{n}} \rangle / \langle A_{\mathrm{b}} \rangle (R)$	~0.4%
$\langle A_{\mathrm{w}} \rangle / \langle A_{\mathrm{b}} \rangle (D)$	~1.8%
$\langle A_{\mathrm{w}} \rangle / \langle A_{\mathrm{n}} \rangle (D)$	~5.9
$\langle A_{\mathrm{n}} \rangle / \langle A_{\mathrm{b}} \rangle (D)$	~0.3%

intensity $\langle A_{\mathrm{w}} \rangle / \langle A_{\mathrm{b}} \rangle$. The amplitude is defined as the root mean square (R.M.S.),

$$\langle A_\alpha \rangle = < A_\alpha(s_m, t_k) > = \sqrt{\sum_{m=1}^{m=N_s} \sum_{k=1}^{k=N_t} \frac{A_\alpha^2(s_m, t_k)}{N_s N_t}}, \qquad (4.1)$$

where α is w, n or b for the wave, noise and background amplitude, respectively. s_m and t_k are the indices along the s and t axes, respectively. N_s and N_t are the total numbers of pixels along the axes. $N_s = 41$ or 20 for R_1 (D_1) and R_2 (D_2), respectively, and $N_t = 150$ for both of them. The array A_w is defined as $A_w(s_m, t_k) = X(s_m, t_k)$, and $A_n(s_m, t_k) = \sigma(X(s_m, t_k))$ is the data noise of $X(s_m, t_k)$ and is discussed in Sec. 2.3. $A_b(s_m, t_k) = B(s_m, t_k)$ is the background amplitude. The ratios $\langle A_{\mathrm{w}} \rangle / \langle A_{\mathrm{n}} \rangle$ are 3.3 (4.9) and 3.5 (6.9), and $\langle A_{\mathrm{w}} \rangle / \langle A_{\mathrm{b}} \rangle$ are 0.0145 (0.0169) and 0.0145 (0.0207), for R_1 (D_1) and R_2 (D_2), respectively.

Uncertainties in the enhanced time-distance plot

The time-distance plot was taken by averaging over three pixels across the slit, therefore the data noise as in Eq. (2.11) should be scaled by a factor of $1/\sqrt{3} = 0.58$. The running difference was generated by $R(s_m, t_k) = C(s_m, t_k) - C(s_m, t_{k-9})$. We assumed the images were taken independently, there was no data noise correlation along the time sequence. For a value in the running difference plot, the uncertainty

is estimated as $\sigma(R(s_m, t_k)) = \sqrt{\sigma^2(C(s_m, t_k)) + \sigma^2(C(s_m, t_{k-9}))}$. The noise amplitude in the running difference plot can be estimated with Eq. (4.1). On average, it is ~0.4% of the background intensity and ~30% of the amplitude of the propagating disturbances.

The background is constructed by averaging over $N = 50$ points. The uncertainty in $B(s_m, t_k)$ is $1/\sqrt{50 \times 3}$ of a normal flux value, and hence is neglected. Thus $\sigma(D(s_m, t_k)) = \sigma(C(s_m, t_k))/B(s_m, t_k)$. It is ~0.3% of the background intensity and ~20% of the disturbance amplitude.

4.2.2 Measuring apparent phase speed

In the analysed dataset, propagating disturbances are seen at distances of less than ~20 Mm. Also, the apparent propagation speed appears constant at these distances. It is consistent with previous observations of this phenomenon, which showed that any noticeable speed variation can appear at larger heights only (Robbrecht et al. 2001; Gupta et al. 2010). No other periodicities, except 3-min oscillations, are found in the power spectrum of the time signal. We designed three methods for measuring the apparent speed of propagating disturbances, taking the observed fact that the phase speed in the sample does not change either with time or spatial location along the cut. Accordingly, we approximated the propagating disturbances with a propagating harmonic wave function $A\cos(\omega t - kx + \phi)$, with constant parameters A, ω, k and ϕ, which is the key element in the three methods:

- cross-fitting technique (CFT, Sec. 4.2.2),

- 2D coupled fitting (DCF, Sec. 4.2.2),

- best similarity match (BSM, Sec. 4.2.2).

We describe the methods in detail in the following subsections and apply the methods to the samples R_1 (D_1) and R_2 (D_2).

Cross-fitting technique

We assumed that the enhanced time-distance plot $X(s_m, t_k)$ is well described by $A\cos(\omega t - kx + \phi)$. At each spatial location (pixel), the variation of the pixel flux $X(s_m, *)$[1] is taken as a time series. The errors $\sigma(X(s_m, *))$ are estimated as in Sec. 4.2.1. The time series is then fitted with $A_s \cos(\omega_s t + \phi_s) + \delta_s$ [2]. Thus, the

---

[1] $X(s_m, *)$ means that taking the samples in the array $X(s_m, t_k)$ at indices $(s_m, 1)$, $(s_m, 2)$, $\cdots$, (s_m, N_t), while $X(*, t_k)$ means sampling at $(t_k, 1)$, $(t_k, 2)$, $\cdots$, (t_k, N_s) as in the following text.

[2] The subscript s denotes that this parameter varies with the spatial location s, an extra term δ_s allows for weak fluctuations between the pixels.

value of ω_s and its uncertainty[3] are obtained for each pixel. This is repeated for every pixel. The weighted mean and its uncertainty are calculated from abundant measurements (see top right panels of Fig. 4.1 (a), (c), (b) and (d)). For each time sample, the spatial pixel flux variation $X(*, t_k)$ along the direction of propagating disturbances is fitted with $A_t \cos(k_t x + \phi_t) + \delta_t$ to obtain the wave number. By repeating this operation for each pixel, we are able to get a weighted mean of k (see bottom left panels of Fig. 4.1 (a), (c), (b) and (d)). Finally, the parameters ω and k, with their weighted means, are combined to calculate the phase speed (see bottom right panels of Fig. 4.1 (a), (c), (b) and (d)).

We performed the Levenberg-Marquardt least-squares minimisation using the function *mpfitfun.pro* provided by Markwardt (2009). We applied constraints on the amplitude in the fitting, the $A_{t,s}$ are bounded between A_w and $\sqrt{2}A_w$, based on the fact that the root mean square of the wave $A \cos(\omega t - kx + \phi)$ is $A/\sqrt{2}$. The results are displayed in Fig. 4.1 and summarised in Sec. 4.2.3.

2D coupled fitting

Similarly to CFT, we assumed that the signal is of a harmonic form. Instead of performing independent non-linear fitting in both axes, we performed global 2D fitting with the function $A \cos(\omega t - kx + \phi) + \delta$.

We applied the same non-linear fitting algorithm: the Levenberg-Marquardt least-squares minimisation, using the 2D fitting function *mpfit2dfun.pro* provided by Markwardt (2009). Similarly to CFT, we constrained the amplitude between A_w and $\sqrt{2}A_w$. The results are illustrated in Fig. 4.2 and described in Sec. 4.2.3.

Best similarity match

The enhanced time-distance plot can be regarded as an image with tilted ridges, which can be roughly described by the harmonic propagating function $A \cos(\omega t - kx + \phi)$. We are able to measure the propagating speed and period by shape matching between the enhanced time-distance plot and a model image $M(s_m, t_k) = A \cos(\omega t_k - ks_m + \phi)$. The shape matching is quantified by a similarity measure, which is mostly based on the Minkowski distance

$$L_p(M, R) = \left(\sum_{m=1}^{m=N_s} \sum_{k=1}^{k=N_t} |M(s_m, t_k) - X(s_m, t_k)|^p \right)^{1/p}, \qquad (4.2)$$

---

[3]We take 4σ as the uncertainty at 99.99% confidence level throughout the paper, unless otherwise specified.

where p is a positive number whose values range from 1 to ∞ depending on a specific definition. We calculated the Euclidean distance ($p = 2$) to find the similarity measure. If images M and R match exactly, $L_p = 0$, otherwise, the best similarity measure is found by minimising L_p.

In our case, let $X = X(s_m, t_k)$ be R_1 (D_1) or R_2 (D_2) (and is referred to as the reference image hereafter), and construct the model image M with the model function of the same size as X. The amplitude of M was scaled by a factor $\langle X \rangle / \langle M \rangle$, where $\langle \cdots \rangle$ means R.M.S., so that M and X have approximately the same amplitude.

The model image $M = M_{p,V_p,\phi}(s_m, t_k)$ is parametrised by the period $p = 2\pi/\omega$, apparent phase speed $V_p = \omega/k$ and phase ϕ. We set $p \in [150, 200]$ s in 1 s step, $V_p \in [20, 120]$ km/s in 1 km/s step, and $\phi \in [0, 2\pi]$ in 5 degree step. For every combination of p, V_p and ϕ, a model image is constructed and the associated Minkowski distance $L_p(R, M_{p,V_p,\phi})$ is calculated. By locating $L_p^{\min}$ in the parametric space, we are able to find the best combination of p, V_p and ϕ, these are the parameters that we need to measure R. We accepted 1% above the $L_p^{\min}$, and took a set of p, V_p and ϕ, with the means and standard deviations as the observed value and their uncertainties. The application of BSM to R_1 (D_1) and R_2 (D_2) is shown in Fig. 4.3.

The shape matching can generally be improved by the image regularisation (smoothing). For an image $I(x, y)$, the regularised image can be obtained by its convolution with a normalised Gaussian kernel, $I_{\sigma_x, \sigma_y} = I(x, y) \star G(\sigma_x, \sigma_y)$. In our case, neither R_1 (D_1) nor R_2 (D_2) have enough pixels to perform smoothing without severely subjecting to the edge effect, therefore we only regularised the image with a three-point discrete Gaussian kernel along the time axis. The resulting images R_1^σ (D_1^σ) and R_2^σ (D_2^σ) are displayed in Fig. 4.4. The ridge pattern looks clearer than in Fig. 4.3. The effect of regularisation on the measurement of BSM will be discussed in Sec. 4.2.3.

4.2.3   Results

We applied CFT to the sample R_1 (Fig. 4.1(a)). The fits of ω have a relative error lower than 1% and are distributed in a very narrow band. The weighted mean gives $\omega = 0.0347 \pm 0.00002$ rad/s, which corresponds to a period of $p = 181.2 \pm 0.1$ s. Fits to k have a relative error of $\lesssim 10\%$. The weighted mean $k = 0.738 \pm 0.002$ Mm^{-1} has a relative error of less than 1%, and the values scatter about $\pm 50\%$ of the mean. Thus the apparent phase speed is calculated as $V_p = 47.0 \pm 0.1$ km/s. The resulting propagating features are overlaid with R_1 as the white dashed line in the top left panel of Fig. 4.1(a). The spacing (p) matches very well, implying good fits to ω, the

slope V_p of the dashed lines deviates slightly from the well recognised ridges, while remaining in the acceptable range.

We shortened the spatial length of the sample and applied CFT to R_2. The spatial length of R_2 is a half of R_1, but it includes the most prominent part of the ridges that represents the propagating disturbances. The results are shown in Fig. 4.1(c). The rise of the relative error in k to above 10% is due to the decrease in the number of data points in the spatial direction, therefore the constraint on k is loosed. As seen in Fig. 4.1(c), the best-fitting values of k are distributed in a broader range than those obtained for R_1. The weighted mean of k is about $k = 0.727 \pm 0.005\,\mathrm{Mm^{-1}}$. The measure of ω retains a good accuracy ($\omega = 0.0350 \pm 0.00003\,\mathrm{rad/s}$, $p = 179.7 \pm 0.2\,\mathrm{s}$), which is slightly worsened because of the decrease in the number of samples. The phase speed is calculated as $V_p = 48.1 \pm 0.3\,\mathrm{km/s}$. The spacing remains consistent with the running difference as illustrated in the top left panel of Fig. 4.1(c), the alignment is also very good.

Applying CFT to D_1 and D_2 with a higher signal-to-noise ratio (S/N) gives $V_p = 45.8 \pm 0.2\,\mathrm{km/s}$ and $p = 180.0 \pm 0.1\,\mathrm{s}$ and $V_p = 48.6 \pm 0.4\,\mathrm{km/s}$ and $p = 180.0 \pm 0.2\,\mathrm{s}$, respectively. Both fits are acceptable, and consistent with those obtained for R_1 and R_2.

The application of DCF to R_1 (D_1) and R_2 (D_2) is displayed in Fig. 4.2(a), (b) and Fig. 4.2(c), (d). The fit values are listed in Table 4.2. The DCF is very sensitive to the initial guess for the fit parameters. Since 2D fitting is coupled in both axes, the optimised fit can be reached only for one of the parameters. In our case, we optimised the fit of V_p, by changing the initial guess. It can be optimised for p as well. A fully automatic fit is not feasible because of the dependence on the initial guess.

The BSM works well for all variants of the sample: R_1 (D_1), R_2 (D_2), and the regularised samples R_1^σ (D_1^σ), R_2^σ (D_2^σ), as illustrated in Fig. 4.3 and Fig. 4.4. The measurements are summarised in Table 4.2. The measurement of p and V_p are persistently good in all samples. It appears that BSM is very robust and not sensitive to any pre-processing of the sample.

The effect of lag time

The choice of the lag time ($T_{\mathrm{lag}} = l \times \mathrm{cadence}$) determines the quality of the running difference plot. Our choice of $l = 9$ applied above is just a specific case that appears to be in a good range of selection. To illustrate the effect of the lag time constructing the running-difference data set on the method performance, we plot the measurements of CFT, BSM and BSM(σ) as a function of the lag time in the left columns of

Table 4.2: Comparison of the measured results of the CFT, DCF and BSM methods

		CFT	DCF	BSM
R_1	p (s)	181.2 ± 0.1	240.7 ± 0.7	180.0 ± 1.8
	V_p (km/s)	47.0 ± 0.1	48.8 ± 0.2	47.0 ± 2.6
R_2	p (s)	179.7 ± 0.2	177.2 ± 0.9	178.0 ± 2.0
	V_p km/s	48.1 ± 0.3	65.8 ± 0.3	49.0 ± 4.5
R_1^σ	p (s)	$\ldots$	$\ldots$	180.0 ± 1.0
	V_p km/s	$\ldots$	$\ldots$	48.0 ± 1.3
R_2^σ	p (s)	$\ldots$	$\ldots$	180.0 ± 1.0
	V_p (km/s)	$\ldots$	$\ldots$	50.0 ± 2.6
D_1	p (s)	180.0 ± 0.1	198.9 ± 0.7	180.0 ± 1.0
	V_p (km/s)	45.8 ± 0.2	44.5 ± 0.2	47.0 ± 1.4
D_2	p (s)	180.0 ± 0.2	250.5 ± 2.2	178.0 ± 1.0
	V_p km/s	48.6 ± 0.4	51.4 ± 0.5	49.0 ± 2.8
D_1^σ	p (s)	$\ldots$	$\ldots$	180.0 ± 1.0
	V_p km/s	$\ldots$	$\ldots$	48.0 ± 1.3
D_2^σ	p (s)	$\ldots$	$\ldots$	180.0 ± 0.9
	V_p (km/s)	$\ldots$	$\ldots$	50.0 ± 2.3

Fig. 4.6(a)[4] (R_1) and Fig. 4.6(b)[4] (R_2). The results of DCF are omitted due to its sensitivity to the initial guess. Clearly, for R_1, the measurements of V_p and p are consistently good with the lag time ranging from 12 s to 156 s. However, for the shorter sample R_2, the selection of the lag time is more constrained within 84 s and 132 s, within which the quality of ridges is optimised. This means that for samples with a larger spatial length the choice of the lag time is less limited than for shorter ones.

The effect of detrending time

For the time-distance plot with the background removal and normalisation, the detrending time ($T_{\mathrm{detr}} = N \times$ cadence) affects the results as well. We plot the measurements of CFT, BSM and BSM(σ) as a function of the detrending time in the right columns of Fig. 4.6(a)[4] (D_1) and Fig. 4.6(b)[4] (D_2). For D_1, the measurements are consistently good for all choices of the detrending time. It appears that the detrending time affects the results very little, while for those of D_2, the period p is measured very well with CFT, BSM and BSM (σ) in the whole range. For V_p, the measurements obtained with CFT are systematically lower than those of BSM and BSM(σ). The error bars of the BSM and BSM(σ) measurements are larger than

---

[4]A complete set of figures displaying the quality of the measurements is available at http://www2.warwick.ac.uk/fac/sci/physics/research/cfsa/people/yuan

those in D_1.

4.2.4 Conclusion

We designed three methods, CFT, DFC and BSM, to measure the average apparent phase speed of propagating EUV disturbances. The applications to R_1 (D_1) , R_2 (D_2), R_1^σ (D_1^σ), R_2^σ (D_2^σ) are summarised in Table 4.2 and illustrated in Fig. 4.5. Fig. 4.6 shows the effect of the lag time and detrending time on the measurements.

From the computational aspect, the CPU time consumption descends as BSM, CFT, DCF. Applying these methods to $R_1(R_2)$ in a GNU/linux x86_64 computer, it takes $321(158)\,$s, $4.9(2.5)\,$s and $2.5(0.7)\,$s for BSM, CFT and DCF, respectively. The CPU time consumption for D_1 and D_2 is very similar. In addition, CFT and DCF require estimating the data noise, but provide better accuracy. Also, the DCF is very sensitive to the initial guess for the parameters in the fitting function, therefore it is not suitable for automatic measurements (see, e.g. Sych et al. 2010; Martens et al. 2012). The BSM is more tolerant to the data noise and pre-operations that do not affect the image morphology.

The valid measurements of the apparent phase speed V_p in the analysed event range from 48 to 52 km/s, with an average value of $47.6\pm0.6\,$km/s and $49.0\pm0.7\,$km/s for $R_1(R_2)$ and D_1 (D_2), respectively (see Table 4.2 and Fig. 4.5, top panel).

For all three methods, it appears that the measurements made for R_1 and D_1 are on average better than those for R_2 and D_2. Accordingly, spatially-longer cuts, even if the amplitude of the disturbance is continuously declining, are preferable for the analysis. Longer samples are more tolerant to the choice of the lag time and detrending time, while shorter ones restrict the choice. We also showed that the measurements in D_1 (D_2) generally outperform those made in R_1 (R_2), therefore the background-removal method seems to be superior than running difference, at least in our applications.

The measurements of the oscillating period are consistent in CFT and BSM and agree well with the measurements based upon spectral methods (e.g. Fourier transform or periodogram). Therefore, the methods described in the paper provide also an alternative tool for the estimation of the period.

The systematic error in the apparent phase speed estimation mainly originates from the traits of the propagating disturbance. In particular, the apparent phase speed may change along the propagating direction because of the geometry, projection or (and) physics, so that the diagonal ridges may be bent. But in the analysed case, the spatial scale of the detection of the propagating disturbances does not reach ~20 Mm, above which a noticeable change of propagating speed was reported

(e.g. Robbrecht et al. 2001; Gupta et al. 2010). It may also be a variant of time, so different ridges do not have the same slope. In the analysed data we did not find this effect. Another deviation may originate from the inconsistency with the harmonic wave feature in our assumption. The good agreement in the measurement with the propagating harmonic wave form also implies that the propagating disturbances are slow magnetoacoustic waves rather than recurring upflows. The designed methods are not likely to work on samples taken during transient, e.g. flaring activity.

The amplitude A of the disturbance decreases during its travelling. The methods can be improved by accounting for the spatial variation of the amplitude $A = A(s_x)$. However, this will add an extra dimension to these methods, which means higher complexity. Another way of coping with this feature is to normalise the amplitude in each pixel along the cut to the highest amplitude of the narrowband signal measured at this pixel, before applying the methods.

Moreover, it is known that the amplitude of 3-min oscillations in sunspots is modulated by long-period oscillations (e.g. Sych et al. 2012). Therefore, it is natural to expect the same effect in their coronal counterpart observed in EUV. This effect can be studied with the methods designed in this paper, by applying them to a sliding window in time, imposed on a longer dataset. Likewise, the window can be applied in the spatial domain. This will reveal any possible speed variations in time and at different locations.

The three methods were shown to work well on the AIA data in EUV bandpasses. These methods can also be applied to other imaging data-cubes, obtained with other instruments and in other bands, e.g. UV, visible light and microwave.
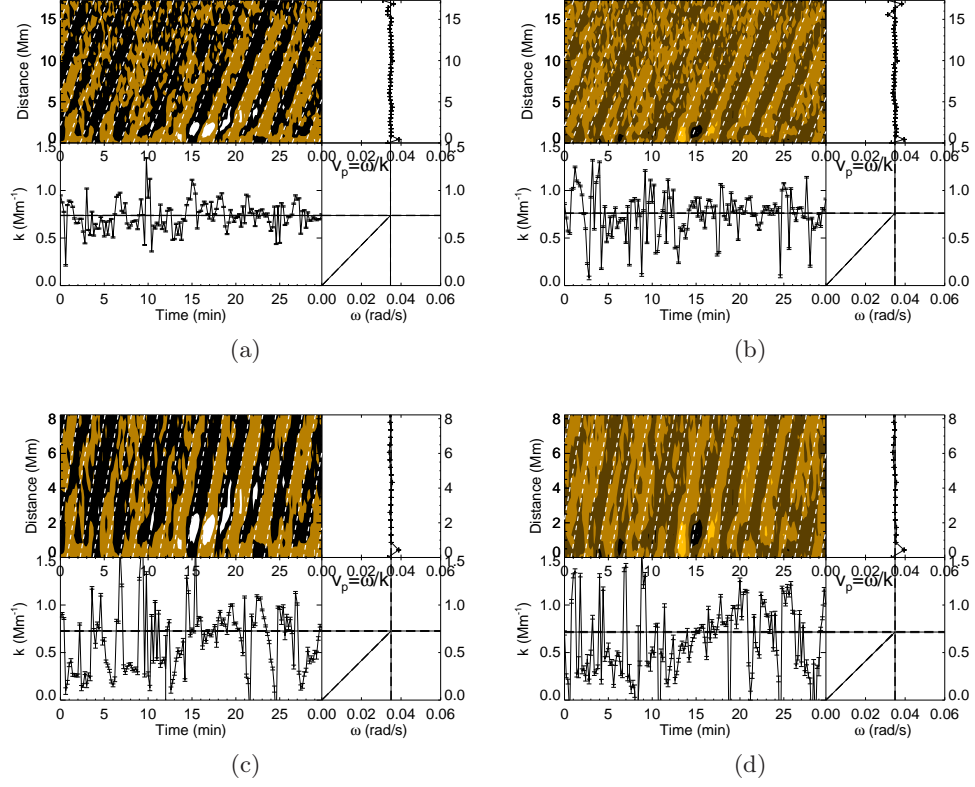
Figure 4.1: Application of CFT to R_1(a), R_2(c), D_1(b), and D_2(d). In each panel, top left: the running difference of the time-distance plot, overlaid with the contour (white dashed line) of the model function $A\cos(\omega t - kx + \phi)$ with the best-fitted parameters. Top right: the fitting result of ω as a function of the spatial location. The thick solid line is the weighted mean, the dashed lines indicate its uncertainties. Bottom left: the fitting result of k as a function of time. The thick solid line is the weighted mean, and the dashed lines indicate its uncertainties. Bottom right: The ω-k dispersion diagram and the calculation of phase speed V_p and its uncertainties. The fitted parameters are as follows: (a) for R_1, $\omega = 0.0347 \pm 0.00002\,\mathrm{rad/s}$, $k = 0.738 \pm 0.002\,\mathrm{Mm^{-1}}$, $p = 181.2 \pm 0.1\,\mathrm{s}$, $V_p = 47.0 \pm 0.1\,\mathrm{km/s}$; (c) for R_2 $\omega = 0.0350 \pm 0.00003\,\mathrm{rad/s}$, $k = 0.727 \pm 0.005\,\mathrm{Mm^{-1}}$, $p = 179.7 \pm 0.2\,\mathrm{s}$, $V_p = 48.1 \pm 0.3\,\mathrm{km/s}$; (b) for D_1 $\omega = 0.0349 \pm 0.00003\,\mathrm{rad/s}$, $k = 0.762 \pm 0.003\,\mathrm{Mm^{-1}}$, $p = 180.0 \pm 0.1\,\mathrm{s}$, $V_p = 45.8 \pm 0.2\,\mathrm{km/s}$; (d) for D_2 $\omega = 0.0349 \pm 0.00003\,\mathrm{rad/s}$, $k = 0.716 \pm 0.006\,\mathrm{Mm^{-1}}$, $p = 180.0 \pm 0.2\,\mathrm{s}$, $V_p = 48.6 \pm 0.4\,\mathrm{km/s}$.
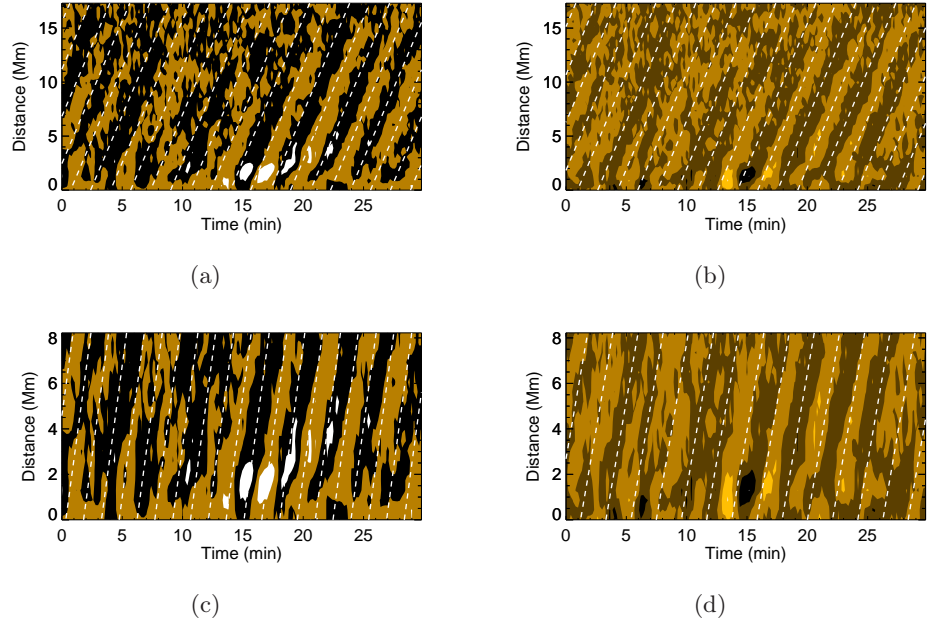
Figure 4.2: Application of DCF to R_1(a), R_2(c), D_1(b), and D_2 (d). In each panel, the running difference of the time-distance plot is overlaid with the contour (white dashed line) of the model function $A\cos(\omega t - kx + \phi)$ with the best-fitted parameters. The best-fitted parameters are: (a) for R_1, $p = 240.7 \pm 0.7$ s, $V_p = 48.8 \pm 0.2$ km/s; (c) for R_2, $p = 177.2 \pm 0.9$ s, $V_p = 65.8 \pm 0.3$ km/s; (b) for D_1, $p = 198.9 \pm 0.7$ s, $V_p = 44.5 \pm 0.2$ km/s; (d) for D_2, $p = 250.5 \pm 2.2$ s, $V_p = 51.4 \pm 0.5$ km/s.
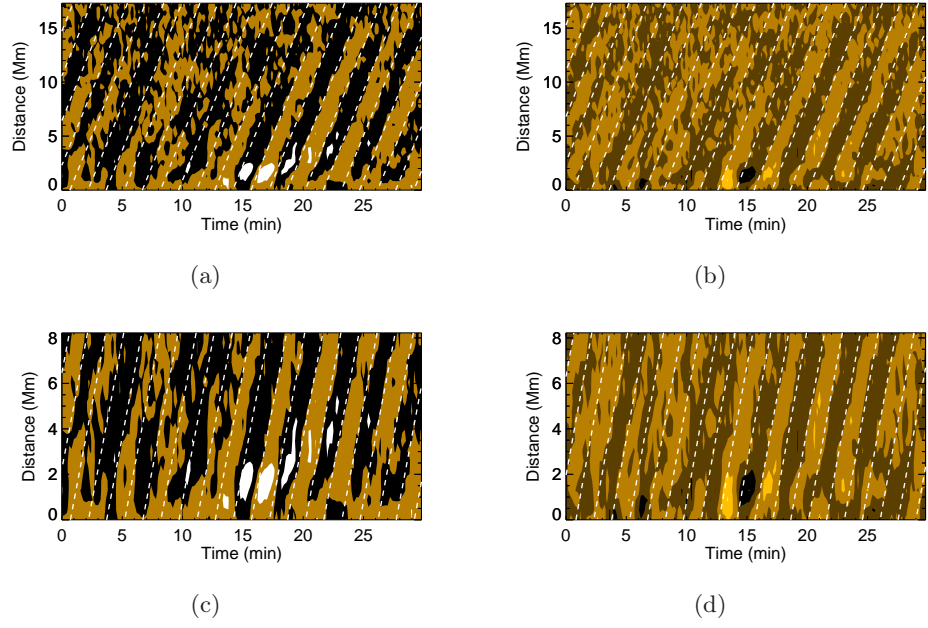
Figure 4.3: Application of BSM to R_1(a), R_2(c), D_1(b), and D_2 (d). In each panel, the running difference of the time-distance plot is overlaid with the contour (white dashed line) of the model function $A\cos(\omega t - kx + \phi)$ with the fitted parameters. The fitted parameters are as follows: (a) for R_1, $p = 180.0 \pm 1.8\,\text{s}$, $V_p = 47.0 \pm 2.6\,\text{km/s}$; (c) for R_2, $p = 178.0 \pm 2.0\,\text{s}$, $V_p = 49.0 \pm 4.5\,\text{km/s}$; (b) for D_1, $p = 180.0 \pm 1.0\,\text{s}$, $V_p = 47.0 \pm 1.4\,\text{km/s}$; (d) for D_2, $p = 178.0 \pm 1.0\,\text{s}$, $V_p = 49.0 \pm 2.8\,\text{km/s}$.

(a)   (b)

(c)   (d)
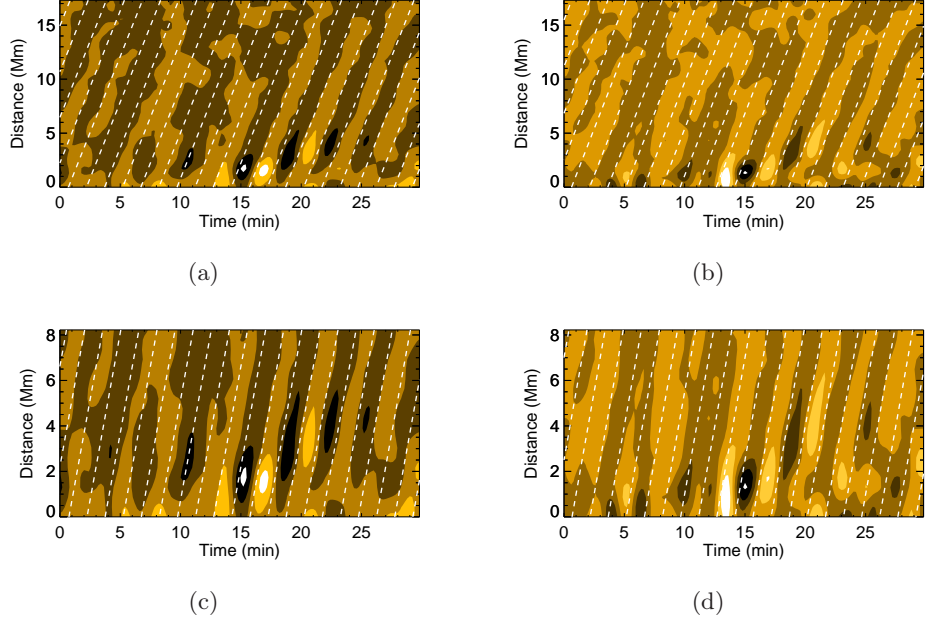
Figure 4.4: Application of BSM to R_1^σ(a), R_2^σ(c), D_1^σ(b), and D_2^σ (d). In each panel, the running difference of the time-distance plot is overlaid with the contour (white dashed line) of the model function $A\cos(\omega t - kx + \phi)$ with the best-fitted parameters. The best-fitted parameters are follows: (a) for R_1^σ, $p = 180.0 \pm 1.0\,\mathrm{s}$, $V_p = 48.0 \pm 1.3\,\mathrm{km/s}$; (c) for R_2^σ, $p = 180.0 \pm 1.0\,\mathrm{s}$, $V_p = 50.0 \pm 2.6\,\mathrm{km/s}$; (b) for D_1^σ, $p = 180.0 \pm 1.0\,\mathrm{s}$, $V_p = 48.0 \pm 1.3\,\mathrm{km/s}$; (d) for D_2^σ, $p = 180.0 \pm 0.9\,\mathrm{s}$, $V_p = 50.0 \pm 2.3\,\mathrm{km/s}$.
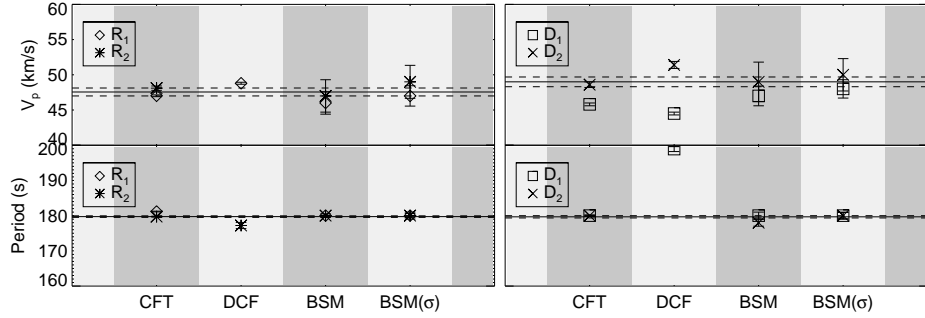
Figure 4.5: Comparison of the measurements obtained with CFT, DCF, BSM and BSM(σ). V_p and p are plotted in the upper and lower panels, respectively. The solid line is the corresponding average value and the dashed lines enclose the uncertainty of 1σ range in each panel. For R_1 (diamond) and R_2 (convolution), $\bar{V}_p = 47.6 \pm 0.6\,\mathrm{km/s}$ and $\bar{p} = 179.7 \pm 0.2\,\mathrm{s}$. For D_1 (square) and D_2 (cross), $\bar{V}_p = 49.0 \pm 0.7\,\mathrm{km/s}$ and $\bar{p} = 179.7 \pm 0.3\,\mathrm{s}$.

107
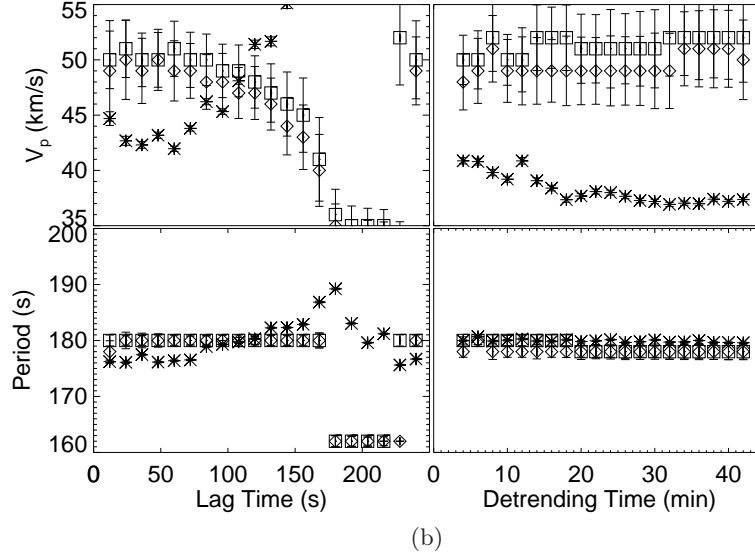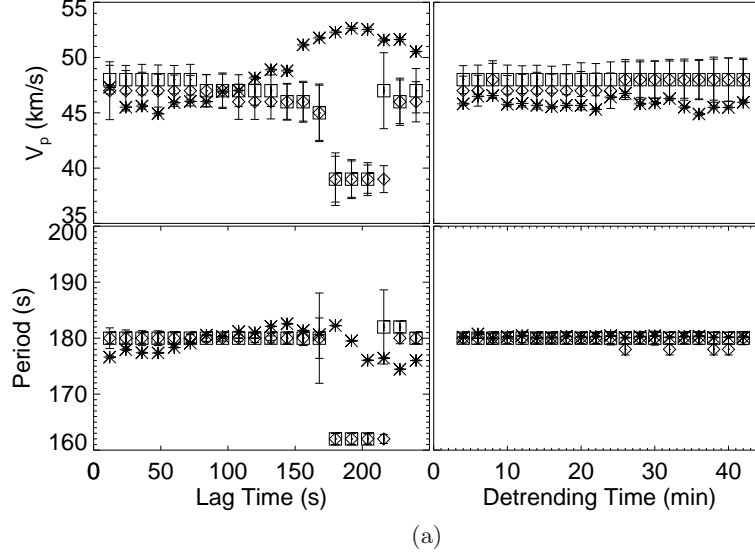
Figure 4.6: (a)Measurement of the phase speed and period in R_1 as a function of the lag time, and those in D_1 as a function of the smoothing time. (b) the corresponding measurement in R_2 and D_2. In (a) and (b), the upper panel is the measurement of V_p and the bottom one is of p. The measurements obtained with CFT, BSM and BSM (σ) are shown in convolution, diamond and square, respectively.

Chapter 5

Characteristics of propagating fast magnetoacoustic waves

5.1 Introduction

The theory of magnetohydrodynamic (MHD) waves in structured plasma was developed in the 1970s and 1980s (e.g. Zajtsev & Stepanov 1975; Roberts 1981b,a; Edwin & Roberts 1982, 1983b). During the past decades, various MHD wave modes were confidently detected with modern instruments, and were exploited for seismological applications (see reviews by, e.g., Nakariakov et al. 2005; De Moortel & Nakariakov 2012). Standing fast kink waves were detected in the closed coronal loops (e.g. Nakariakov et al. 1999; Aschwanden et al. 1999; White et al. 2012) and in post-flare arcades (Verwichte et al. 2005). The global (fundamental) kink mode was implemented to estimate the magnetic field strength (so called MHD seismology, e.g. Nakariakov & Ofman 2001). Propagating fast kink waves were found in the coronal loops (Williams et al. 2002; Tomczyk et al. 2007; Van Doorsselaere et al. 2008). Trapped fast sausage modes, due to the existence of the cut-off wavenumber (Nakariakov et al. 2003), are only supported by sufficiently thick and dense loops. Some spatially-resolved radio imaging observations were consistent with the features of fast sausage waves (e.g. Asai et al. 2001; Melnikov et al. 2005). Standing slow mode waves were detected as intensity and Doppler-velocity oscillations in the post-flare loops using spectrometric data (Wang et al. 2003). Propagating slow mode waves were confidently detected near the footpoints of active region loops (e.g. De Moortel et al. 2000; Marsh et al. 2009; Wang et al. 2009a; Verwichte et al. 2010; Yuan & Nakariakov 2012, and Chapter 4).

In the SDO/AIA era (Lemen et al. 2012; Boerner et al. 2012, and Chapter 1),

the full solar disk is recorded with high temporal and fine spatial resolution. It allows for confident detection of sporadically occurring coronal fast magneto-acoustic waves (Liu et al. 2011; Shen & Liu 2012). It was found that quasi-periodic propagating fast waves exhibit similar periodicities (with the most prominent peak at about 3-min) with the quasi-periodic pulsations (QPP) in X-ray emission (Liu et al. 2011; Ofman et al. 2011). This result is consistent with previous studies, where 3-min oscillations are sourced to the chromospheric level in sunspot umbrae and found to modulate QPP in the form of slow mode MHD waves (Sych et al. 2009). Also, flares are known to generate non-thermal electrons that are responsible for microwave and X-ray emissions. Moreover, flares can excite MHD oscillations. The relationship of QPP in microwave and X-ray emission and coronal MHD waves was intensively investigated (see review by, e.g. Nakariakov & Melnikov 2009).

It was demonstrated that, if an impulsively-generated fast magntoacoustic wave is guided by a region of low Alfvén speed (i.e. coronal loop, current sheet), the wave at a distance away from the source develops into a quasi-periodic wave train with pronounced frequency and amplitude modulation owing to the dispersion properties of guided fast waves (Roberts et al. 1984; Murawski & Roberts 1994). The time signature shows a very typical tadpole wavelet spectrum: a narrow-spectrum long-period head is followed by a broad-spectrum short-period tail (Nakariakov et al. 2004). However, such tadpole wavelet spectrum is only prominent if the initial spectrum is sufficiently broad and situates mostly above the cut-off wavenumber (Nakariakov et al. 2005). Also, the radio emissions associated with solar flares were found to be modulated by propagating fast waves and exhibit evident tadpole wavelet spectra (Mészárosová et al. 2009a,b).

In this chapter, we report the observation of distinct quasi-periodic propagating fast magneto-acoustic wave trains (QPF). The QPF processes was described in Sec. 5.2. The analysis and results are presented in Sec. 5.3. The discussion and conclusion are given in Sec. 5.4.

5.2   Observations

We report an observational study of a QPF wave event on 30 May 2011. A GOES C2.8 flare occurred at 10:48 UT in active region AR11227. Propagating fast magneto-acoustic wave trains were observed as intensity perturbations at a distance about 110 Mm from the flare epicentre at 10:50:12 UT. They are only detected in the AIA 171 Å bandpass. The lag time between the flare occurring and the first wavefront appearing is about 2.2 min. The average energy transit speed is estimated at about

833 km/s, well in the Alfvén (fast) wave speed range under the coronal conditions. The data preparation and initial analysis were presented in Shen & Liu (2012). A shorter data set for about 26 min was used starting from 10:45 UT. The data cube is a set of images in size of 834×834 pixels. The images were normalised with their exposure times, and were interpolated into a uniform time grid with a 12 s cadence.

It was shown that the GOES and RHESSI light curves exhibit a very steady increase in the particle counts during the flare, no fine structure of flare emission was significantly detected in the soft and hard X-ray bands (Shen & Liu 2012). To show the fine structure of the flare pulsations, we obtained the radio observation in the same time interval (10:45 - 11:11 UT) in 173.2 MHz and 228.0 MHz provided by the Nançay Radioheliograph (NRH, cf. Fig. 5.2, top panel). It reflects the radio emission of the flare-accelerated non-thermal electrons.

5.3   Analysis and results

We identify three distinct wave trains in this QPF event, they exhibit different properties: (we denote the wave trains as Train-1 or T1, Train-2 or T2 and Train-3 or T3, cf. Fig. 5.1):

1. There are obvious gaps in space (time) between the leading and trailing trains, about 40.7 Mm (72 s) between T1 and T2, and about 35.0 Mm (90 s) between T2 and T3.

2. The wavelengths (periods) are quite different, 33.7 ± 0.6 Mm (58 ± 1 s), 24.4 ± 0.1 Mm (40 ± 0.5 s) and 25.7 ± 0.3 Mm (38 ± 1 s) for T1, T2 and T3, respectively.

3. The wave trains exhibit different initial phase speeds: 735 ± 58 km/s (T1), 845 ± 42 km/s (T2) and 820 ± 90 km/s (T3)

4. The wave trains agree in arising time with radio bursts generated by the non-thermal electrons (cf. Fig. 5.2, top panel).

Therefore, we divide the QPF into three wave trains and measure their parameters separately.

We first look at how the wave trains are correlated with the flaring radio bursts. It was found that the frequency of radio emission in the magnetic reconnection site and energy releasing region are in the range of 400-1000 MHz (Bastian et al. 1998). The radio emission at 173.2 MHz is sourced at lower height than 228.0 MHz, but both above the magnetic reconnection site and energy release region (Bastian et al. 1998). This explains the time lag between the NRH radio bursts and the

flare start time. The flare started at 10:48 UT. The first radio burst arose at about 10:49:12 UT in 228.0 MHz band. Train-1 started at about 110 Mm from the flare epicenter at about 10:50:12 UT. The radio emissions in 173.2 MHz peaked at about 10:50:30 UT, slightly lagged behind Train-1. The second radio burst appeared between 10:53 and 10:55 UT, first appearing in 228.0 MHz, then in 173.2 MHz. Train-2 started at 10:54:24 UT about 1 min after the burst in 228.0 MHz. The third radio burst appeared between 10:57 and 11:00 UT, only in 173.2 MHz, no significant burst is detected in 228.0 MHz. The start time of Train-3 was at 10:58:12 UT during the third radio burst. We infer that at least three flaring energy pulses were released during the flare. The energy releases apparently triggered both fast wave trains, and accelerated non-thermal electrons that were transported to higher atmosphere and generated radio bursts. Therefore the fast wave trains and radio bursts exhibit a steady correlation in their start times.

The dispersive evolution of impulsively-generated fast wave trains is determined by the density profile of the waveguide. The time signature of the wave train displays a characteristic tadpole wavelet spectrum, exhibiting a gradually decreasing period and hence a streching wavelength (Nakariakov et al. 2004).

In Fig. 5.3, we display the spatial variation of the wavelengths of the wave trains along L3. It is shown that the wavelengths stretch along the open coronal loops. It is another indicator, besides a decreasing period, of dispersive evolution of the fast wave trains. The time signature and wavelength of QPF indicates that the fast magneto-acoustic wave is likely to be triggered by an impulsive energy source. To diagnose the loop density profile as suggested by Nakariakov et al. (2004) is not possible at the current stage, due to limited temporal resolution.

Fig. 5.4 (top panel) illustrates that the wave amplitudes increase with distance, peak and then decay gradually. This effect is very prominent in Train-2: it reaches a maximum amplitude at about 180 Mm, about the 21% larger than the value at about 130 Mm.

The amplitude profile normal to the wave vector is resolved with SDO/AIA as well. A wave front evolution of Train-2 is displayed in Fig. 5.5. The transverse distribution of the wave amplitude was approximated with a Gaussian profile. It shows that the wave front extends gradually along the waveguiding structure. It was found that the density perturbations of a kink (sausage) wave inside and outside a coronal loop exhibit in-phase (out-of-phase) motion (Cooper et al. 2003b). The wave propagation observed as intensity perturbations inside and outside the coronal loop are in-phase in our case. Such a spatial structure is more consistent with the kink mode polarised along the line-of-sight. In such case, the kink mode can be observed

as emission intensity variations because of its modulation to the line-of-sight column depth of the oscillating plasma structure (Cooper et al. 2003a).

We used the Best Similarity Measure method (BSM, Yuan & Nakariakov 2012, and Chapter 4) to obtain the phase speed and estimate its error (Fig. 5.2, bottom panel). Fig. 5.4 (bottom panel) shows that the wave trains started with slightly different initial phase speeds: 735 ± 58 km/s (T1), 845 ± 42 km/s (T2) and 820 ± 90 km/s (T3). However they appears to end up with the same projected phase speed at about 600 km/s. The deceleration was found to be 1.35 ± 0.67 km/s^2, 2.27 ± 0.39 km/s^2 and 1.31 ± 0.56 km/s^2 for T1, T2 and T3, respectively.

5.4   Discussion and conclusion

We observed a QPF event with distinct fast wave trains. The wave trains are found to correlate in start time with the radio bursts observed with NRH. The wave fronts appeared not in the flare epicenter but a distance of about 70-110 Mm away, no significant intensity perturbation was detected in-between. Such a behaviour is consistent with the interpretation in terms of the kink mode, provided the waveguide is of a loop shape. In this case, the kink mode can become visible only in the segment of the loop that has a preferable angle to the line-of-sight (Cooper et al. 2003a).

The wave trains are found to correlate well in start time with radio bursts observed with NRH (Fig. 5.2, top panel). The wave trains and the non-thermal electrons (radio burst) apparently originate from the same energy release. The observed fast wave trains have wavelength modulation: components with longer-wavelength propagate faster. Such a behaviour is consistent with the dispersion of fast magneto-acoustic waves in field-aligned plasma waveguides (Nakariakov et al. 2004).

The QPF wave amplitudes were found to amplify during its passage, then started to decay since the midway (Fig. 5.4, top panel). The wave amplitude is determined by both the wave energy and the properties of the waveguide, e.g. the density stratification. As the wave propagates along the open coronal structure, the wave energy spreads to a broader extent, therefore, the wave amplitude tends to decrease. The density stratification along the loops are prone to amplify the wave amplitude. These two factors can lead to the appearance of a maximum amplitude in the midway.

The amplitude distribution normal to the wave vector follows a Gaussian profile. Such a spatial structure is prescribed by the kink eigenmode of the waveguide. Moreover, the wave propagation inside and outside the loop exhibit in-phase collective motions. This feature is more consistent with fast kink wave.

Table 5.1: Observables and physical parameters of the QPF wave trains

Parameters	Train-1	Train-2	Train-3
Start time	10:50:12 UT	10:54:24 UT	10:58:12 UT
End time	10:56:12 UT	10:59:12 UT	11:02:36 UT
Start position	~110 Mm	~80 Mm	~70 Mm
Spatial lag	$\cdots$	~40.7 Mm	~35.0 Mm
Time lag	$\cdots$	~72 s	~90 s
Number of wavefronts	3 (+ 1 diffraction)	5	~5
Wavelength	33.7 ± 0.5 Mm	24.4 ± 0.1 Mm	25.7 ± 0.3 Mm
Period	58 ± 1 s	40 ± 0.5 s	38 ± 1 s
Deceleration	$1.35 \pm 0.67\,\mathrm{km^2/s}$	$2.27 \pm 0.39\,\mathrm{km^2/s}$	$1.31 \pm 0.56\,\mathrm{km^2/s}$

The projected propagating phase speed was found to be in the Alfvén speed range (about $735 - 845$ km/s). The speed difference reaches about 15% for different wave trains at the start position, but the wave trains end up with the same phase speed at about 600 km/s. The deceleration was found to be 1.35 ± 0.67 km/s^2, 2.27 ± 0.39 km/s^2, 1.31 ± 0.56 km/s^2 for T1, T2 and T3, respectively. The deceleration may be caused by the decrease in the Alfvén speed (a joint effect of the magnetic flux tube divergence and stratified density along the loops). However, it may also be a contribution of projection effect.

The observation of fast magneto-acoustic waves provide useful information on the connectivity with flare pulsations. The fine measurements of its wave parameters reflects the details of the plasma and magnetic field. It is potential tool to probe the physical parameters. However, numerical simulations are required to fully understand the wave generation, propagation and decay.
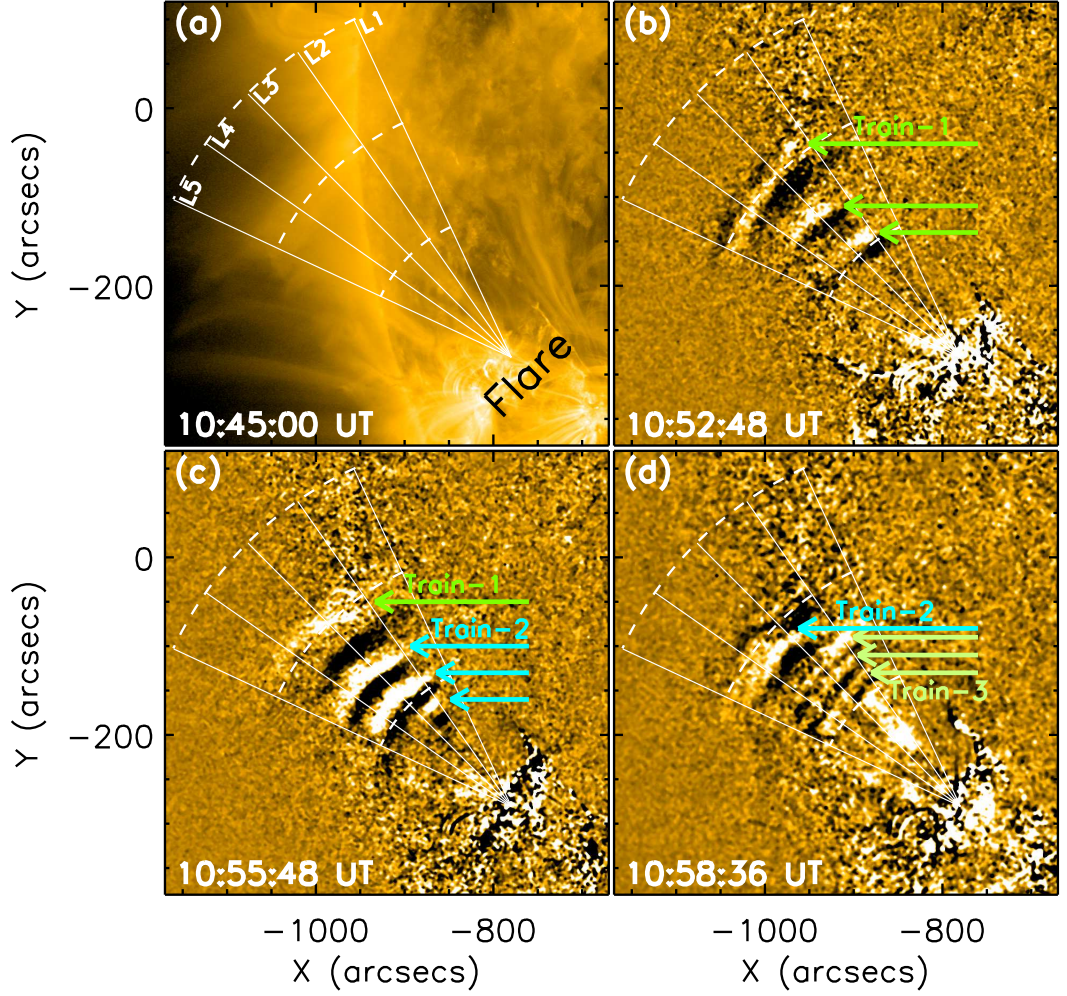
Figure 5.1: (a) The AIA field-of-view in 171 Å displaying the active region AR11227 and the flare epicenter. (b)-(d) Running difference images illustrating the QPF wave trains. The wavefronts of three distinct wave trains are marked by arrow groups in varied color. The solid lines (L1-L5) forming a fan geometry are the cuts used in making time-distance arrays. The dashed arcs are equally spaced as 100 Mm-scale in the radial direction of the fan for reference purpose.
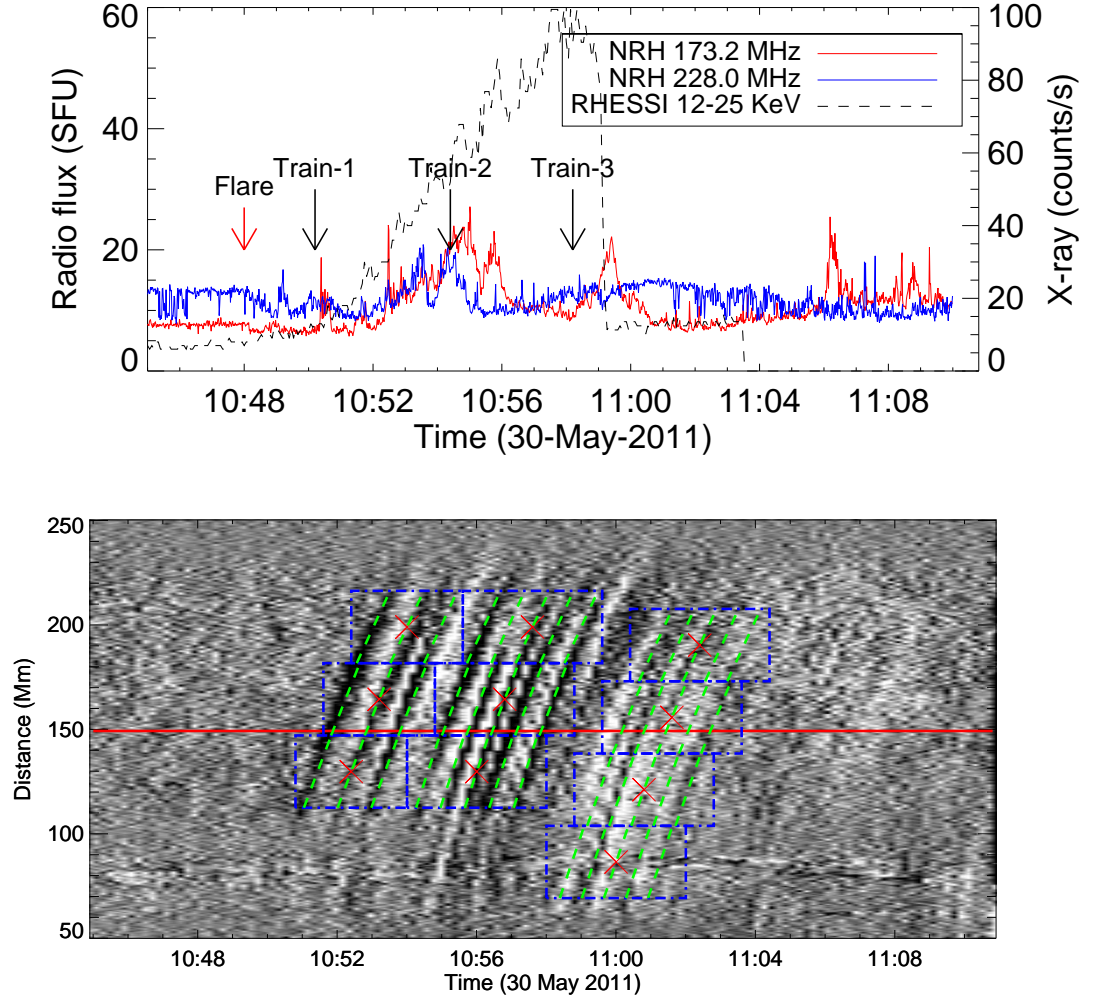
Figure 5.2: Top panel: The radio emission of AR11227 in NRH 173.2 MHz and 228.0 MHz band and the RHESSI hard X-ray count rate in 12-25 KeV. The start time of the flare, Train-1, Train-2 and Train-3 are labeled at the time axis. Bottom panel: The time-distance plot for L3. The samples used to measure the phase speed are enclosed in blue rectangles, the centers are labeled in red cross. The measured results are over-plotted within each rectangle as dashed curves.
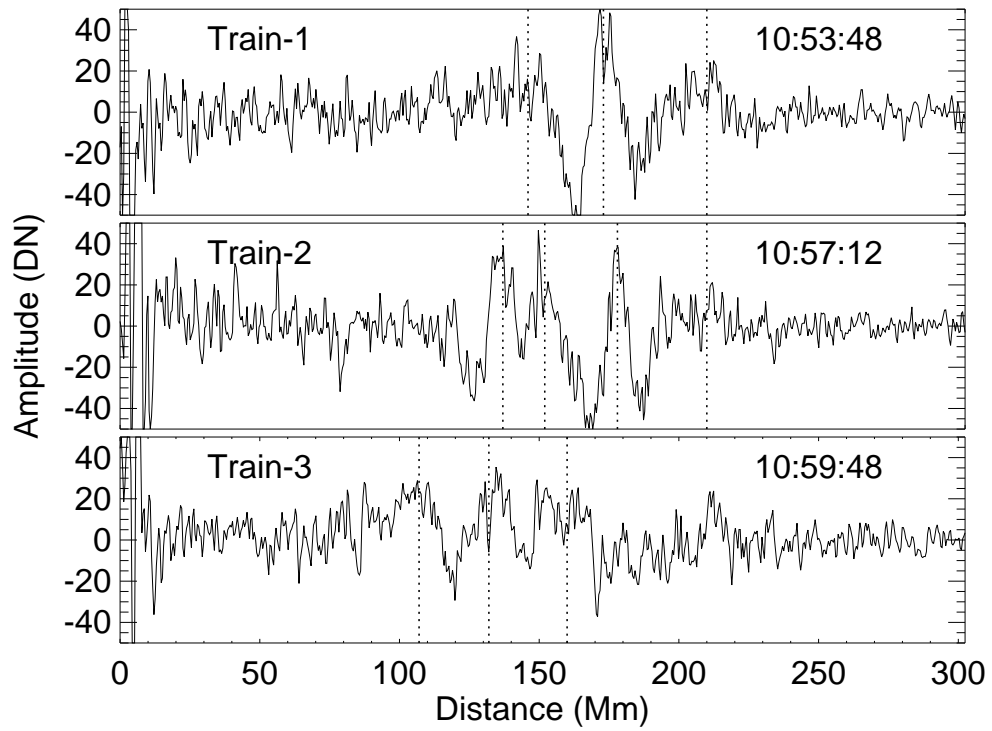
Figure 5.3: The instant cuts along L3 at specific times displaying the wavelength during the wave train evolutions. The horizontal axis denotes the distance along the wave path. The observation times for each snapshot are shown in the panels. The vertical dotted lines mark the approximate positions of the wave fronts.
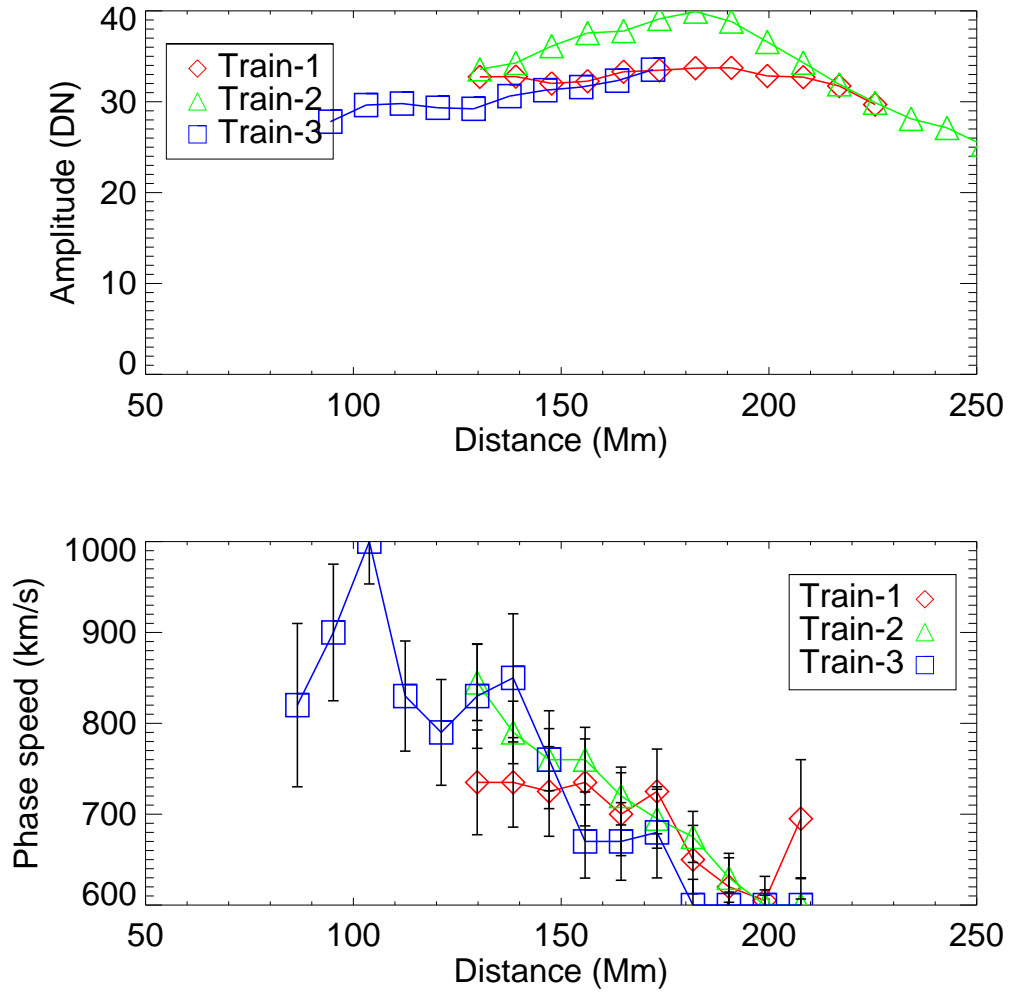
Figure 5.4: The wave amplitude (top) and projected phased speed (bottom) are plotted as a function of the distance to the flare epicenter for the wave trains
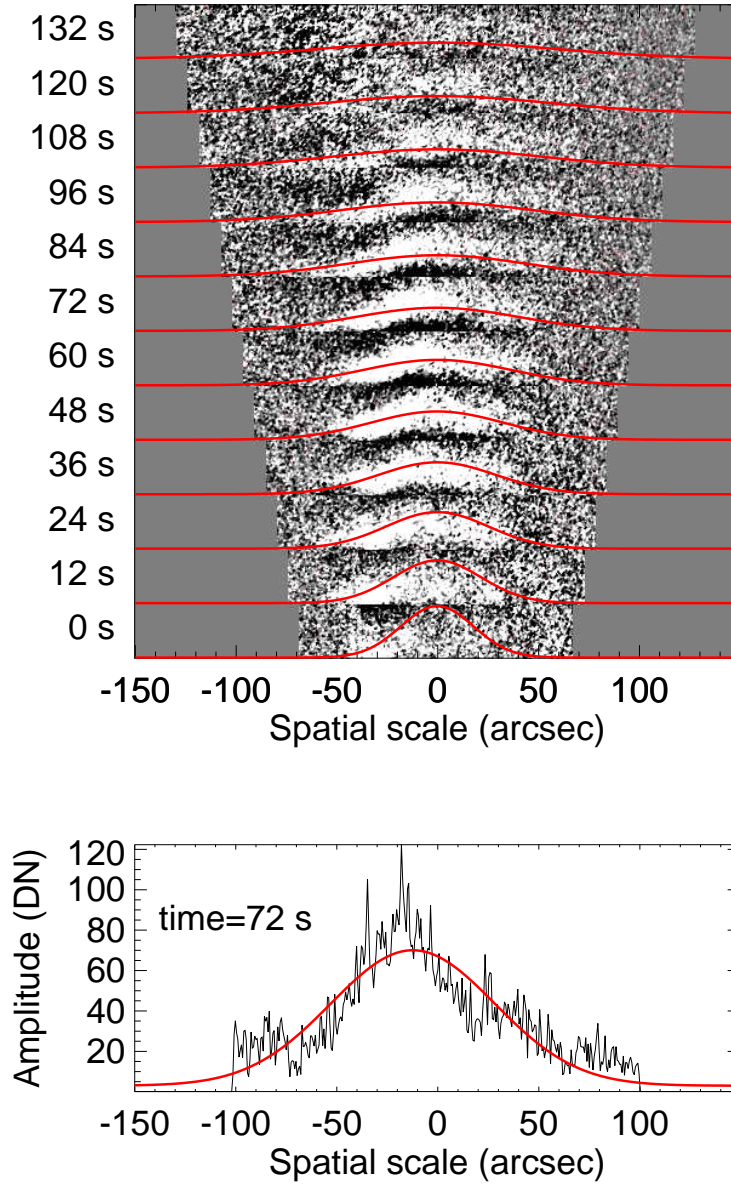
Figure 5.5: Top panel: wave front evolution of Train-2 as a function of time. The red curves are gaussian profiles, the linearly increasing widths are adjusted manually. Bottom panel: an example (72 s) of cross-sectional distribution of amplitude and the gaussian fit (red curve)

Chapter 6

Leakage of long-period oscillations to the corona

6.1 Introduction

Propagating EUV disturbances with periods of the order of several minutes or less are discussed in Chapters 4 and 5. Longer period oscillations are detected in sunspot chromosphere and transition region as well (Nagovitsyna & Nagovitsyn 2001, 2002). The oscillations of tens up to hundreds of minutes were observed as modulations of the radio emission (Gelfreikh et al. 2006). The line-of-sight velocity oscillations with periods ranging from 60 to 80 min were found in the analysis of the Doppler shift of spectral lines in sunspots (Efremov et al. 2009). Long-period oscillations (16–88 min) of the radio emission intensity over sunspots were recently studied with the Nobeyama Radioheliograph (NoRH) (Chorley et al. 2010, 2011).

Theoretical studies argue that these long-period (low frequency) oscillations are well below the cut-off frequency (e.g. Bel & Leroy 1977, and Sec. 1.2.3), thus cannot appear in the corona. However, in the corona, long-period oscillations have been detected in the EUV emission with multiple instruments and in different bandpasses. For example, propagating waves with long periods (10–15 min) were observed in coronal loops with EIT (Berghmans & Clette 1999), TRACE (McIntosh et al. 2008) and STEREO/EUVI (Marsh et al. 2009). Wang et al. (2009b) reported two significant periodicities of 12 and 25 min in the intensity and Doppler shift variations over a coronal diffuse structure with Hinode/EIS. Prominence oscillations with periods ranging from 20 min up to several hours were reported as well (Foullon et al. 2004, 2009; Tripathi et al. 2009; Hershaw et al. 2011).

Likewise, long-period oscillations have been observed in the upper corona and

the solar wind. In particular, Ofman et al. (2000b) detected an oscillation of the polarised white-light brightness with a 30 min period at $1.9R_\odot$ in a polar coronal hole. Similar periodicities in the low-energy charged particle flux were found to be modulated by the variation of the interplanetary magnetic field, which may be of solar origin (Thomson et al. 1995). Moreover, Kepko & Spence (2003) established a high correlation of solar wind density variations and the ultra low frequency (ULF) oscillations of the Earth's magnetosphere, with the power spectrum peaks being located at 0.1, 0.2 and 0.6 mHz.

Thus, there appear questions as to whether the long-period oscillatory phenomena, observed in different parts of the solar atmosphere, are connected with one another, and how this connectivity is carried out. For example, for 3-min chromospheric oscillations in sunspots (see Chapter 3), the possibility of the acoustic wave leakage into the corona has recently been demonstrated numerically (Botha et al. 2011), but for longer periods a similar mechanism has not been developed. Also, a related question is whether the atmospheric long-period oscillations are anyhow connected with the long-period gravity-driven oscillations of the solar interior. Indeed, the solar g-mode periods are estimated in the range of 16 min to 28 h (e.g. Appourchaux et al. 2010), these are similar to the periods of the atmospheric oscillations. The aim of this paper is to contribute to our understanding of this connectivity.

Here, we analyse long-duration observations of active region AR8253 in the 171 and 195 bandpasses of TRACE, for five days. We aim to fully take advantage of the long dataset and search for the long-period oscillations and its originality in combination with NoRH 17 GHz radio data. The dataset and its pre-processing are described in Section 6.2; the orbital effects are discussed in Section 2.1; the power spectrum analysis and the elimination of the orbital artifacts are presented in Section 6.4, and final conclusions are given in Section 6.5.

6.2 Dataset

6.2.1 Observations

TRACE targeted AR8253 almost continuously for about 5 days, from 30 Jun to 4 Jul 1998. The images were taken with the half field-of-view (FOV), 512×512 pixels, at the full resolution of 0.5 arcsec/pixel in 171 and 195 bandpasses. The typical cadence time was either ~ 41 or ~ 30 s. The imaging interval between consecutive images in the 171 and 195 bandpasses was normally 11 s. The data contained several gaps, lasting from ~ 20 min to ~ 4 hours, but the total observation time covered about $\sim 70\%$ of the time span in both EUV bandpasses. Radio observations

at 17 GHz were provided by NoRH. It operates daily from 22 : 45 to 6 : 30 UT of the next day, providing data at 10 s cadence with spatial resolution of 10 arcsec/pixel.

6.2.2 Pre-processing

The TRACE datacubes were prepared with the standard routine TRACE_PREP in Solar Software with standard pre-processing keywords. The EUV images were calibrated with white-light pointing; the spikes and streaks from radiation belts and cosmic rays, plus the readout noise, were removed; the flux intensities were normalised to the exposure time. The image coordinates were co-aligned at the origin of the solar disk in Heliocentric-Cartesian Coordinates to correct the spacecraft re-targeting. The fan-like structure (Fig. 2.1(a)) was tracked with the co-moving frame following the solar surface differential rotation. The spacecraft pointing drifts (Handy et al. 1999), plus the uncertainties of the solar rotational model, were minimised by cross-correlation offsets. Two co-aligned sub-datasets (128×128 pixels) were taken for further analysis (Fig. 2.1(b)).

The NoRH 17 GHz radio data was synthesised with the *Koshix* algorithm. The sunspot was located in the full-disk image and followed with a solar co-rotating box of size (36×36 pixels) (see details in Chorley et al. 2010). The FOV was chosen to coincide with the EUV observations. The position of the region of the microwave emission intensity is contoured in the dashed line in the EUV image in Fig.2.1(c). The strong gyro-resonant emission is situated in the sunspot chromosphere. Above it, the fan-like diffuse structure in the corona is a magnetic field extension from the sunspot (Fig.2.1(a)).

6.2.3 Co-alignment and dejittering

As the TRACE observation spans over 100 hours, the images had to be co-aligned and have jitter removed. Four images were selected for each day as the reference for cross-correlation and were co-aligned by overlapping the footpoint within an accuracy of less than 1.5 pixels. The rest of the images were smoothed with a boxcar of 10×10 pixels, then aligned by the offset calculated by cross-correlating to the corresponding reference image. The offsets were treated as time series and smoothed by running averaging to suppress the noise. This approach is more efficient than any smoothing in the images. However it becomes very unstable to the outliers introduced by disruption(s) to the image topology.

There are three types of outliers (Gounder et al. 2007) in the offsets: 1) Additive outliers (AO) are single exotic values, normally due to CCD saturation

bleeds that ruin part(s) of an image. AOs are easily detected by thresholding and replaced with neighbouring values; 2) Innovational outliers (IO) appear as an abrupt step of the average, during which part of the region of interest is out of the FOV; IOs are corrected by restoring the mean; 3) Transitory change outliers (TCO) are spikes in the time series that disappear gradually. A flare or a bright point normally induces TCO. TCOs are replaced by linearly interpolated values between the points before and after the event (about 0.5 –1 hour).

The global accuracy of the co-alignment over 5 days is less than 1.5 pixels, the local relative accuracies (over several hours) are normally as good as 0.5 pixel. The appearances of TCOs deteriorate the co-alignment accuracy to $\sim$ 2 or 3 pixels for about 0.5 – 1 hour, these parts are deliberately avoided in later analysis.

6.3   Spectral analysis

In the selected time interval, the active region AR8253 was observed for a sufficiently long time to detect long-period oscillations, with least disruptions. In the selection of a suitable time interval, we opted to minimise the presence of large data gaps, as a time series containing them lacks a significant portion of information, and the power spectrum may be totally erroneous irrespective of the spectral analysis technique. The analysed series of the EUV images were not uniformly sampled, and the data has to be re-sampled into uniform time grid by interpolation. Even though, as the data contained some gaps, its power spectrum was obtained with the Lomb-Scargle periodogram technique (Scargle 1982; Horne & Baliunas 1986, also see Sec. 1.3.2). This technique is specifically applicable to the analysis of unevenly sampled data. It overcomes the difficulty posed by unevenness, reduces side-lobe effects and can focus on a certain range of frequencies.

De-trending is applied to the time series by removing the running average before spectral analysis. This process removes the ultra-long period trend, it is normally comparable to the range of the time series and contains the large portion of the total power. De-trending relatively suppresses the low-frequency bandpass and highlights the high-frequency part. We remove 30 min running average in the time series in studying the orbital effect (Fig.2.3), a different averaging time only results in changes in the relative power of the peaks. In obtaining Fig.6.1, we subtracted 60-min running average from the time series.

In order to distinguish the peaks out of orbital artifacts (see Sec.2.1), we applied temporal filtering to the time series. The orbital harmonics are removed by subtracting sinusoidal functions from the time series iteratively with date-compensated

discrete Fourier transform (DCDFT),

$$\hat{y}(t) = y(t) - [d_0 + d_1 \sin(2\pi f t) + d_2 \cos(2\pi f t)] \tag{6.1}$$

where f is a orbital harmonic frequency, the coefficients d_0, d_1, d_2 are estimated according to Ferraz-Mello (1981). Spectral filtering was also attempted, an abrupt window would bring in edge effects to the spectrum, while a smooth one may not completely remove the peak (see Inglis & Nakariakov 2009). DCDFT can be done without tackling the spectral domain, it calculates the accurate magnitude of the frequencies, but sometimes residual peaks may appear around the removed component (see Fig.6.1(e) and (f) and discussions in Sec.2.1).

Referring to the significance level of the detected peaks, no scheme is well accepted by the community, as the distribution of random noise is unknown, a certain assumption of noise distribution has to be made. Moreover, the processing of the data, e.g. de-trending, filtering, destroys the independence of the measurements and coherence of the time series (Hernandez 1999), while these steps are normally unavoidable.

We estimated the false alarm probability (FAP) at 0.01 to the spectrum, assuming Gaussian noise distribution based on Horne & Baliunas (1986). FAP is the probability to reject a detected peak, it only applies to the highest peak in the spectrum, thus, we subtract the highest peak from the time series using equation Eq. (6.1) and repeat this process to the rest of the peaks until all whole spectrum is below the significant level. All peaks quoted in the following text are lower than the 0.01 significance level by default, unless specified such as the bracketed numbers in Table.6.1, they are illustrated in iteration order in Fig. 6.2 (171Å), Fig. 6.3 (195Å) and Fig. 6.4 (17 GHz radio). We also perform Fisher's randomisation test (Linnell Nemec & Nemec 1985b; O'Shea et al. 2001; Yuan et al. 2011, and Sec. 1.3.6) to all the detected peaks in the power spectrum (cf. Sec. 1.3.6). We run 1000 permutations in our studies, the maximum uncertainty is $\sigma(p) = 0.5M^{-0.5} = 0.016$. If $p = 0.0$ is obtained, we quote as $p < 0.01$ by considering the error bar. It is done by iteratively removing the highest peak in the spectrum as described by equation Eq. (6.1). We use the time series analysis package PERIOD developed by the Starlink Project (Dhillon et al. 2001). All results are included in Table.6.1.

6.4 Results

We selected a time series (1998-07-03 00:47-09:00 UT) of a de-rotated macro-pixel (3×3 pixels) situated along the mid-way of the slit (Fig. 2.1(b)) in the image in

171 Å. A time interval affected by a C1.3 GOES-class flare (11:19-11:33 UT) was cropped. There are several images corrupted by CCD saturation bleeding between 09:00 - 10:00 UT, and we simply crop this part. We attempted removing the bad images manually, and included one more hour to the time series, but it resulted in a tiny difference compared to Fig.6.1. The power spectrum of the signal is shown in Fig. 6.1(a). It contains a mixture of peaks, including the orbital artifacts.

We did the same spectral analysis to macro-pixels out of the fan structure, only the orbital artifacts and/or other random peaks due to noise or unknown sources were found. It suggests that the peaks possibly of solar origin are only localised to the diffuse structure. We enlarged the macro-pixel size from 3×3 pixels to 20×20 pixels, the corresponding power spectrum is shown in Fig. 6.1(c). Since the orbital artifact exist in all pixels, it is seen that the rest of the peaks are smoothed out and buried in the relatively enhanced orbital harmonics. In order to identify the disappearing peaks and distinguish signals of solar origin from the noise within the data and artifacts due to spectral leakage of the orbital harmonics, we also performed filtering to the signal, as specified in Sect.6.3. The spectrum (see Fig. 6.1(e)) after filtering out the orbital harmonics, shows significant peaks. The result is confirmed by the 195 Å data, displayed in Fig.6.1(b), (d) and (f). The results are summarised in Table 6.1.

Outside the orbital periodicity and its higher harmonics, we detected significant spectral peaks at 0.123, 0.222, 0.262, 0.302, 0.382, 0.421 and 0.579 mHz in the TRACE EUV 171 Å emission from a fan-like coronal structure in the active region. These peaks are detected with FAP ($p < 0.01$) in both Horne & Baliunas (1986) and Fisher randomisation test (see Fig.6.2 and Table.6.1). In the EUV 195Å data, we only detected 0.262 and 0.559 mHz with $FAP < 0.01$ in both two significance tests. In the Horne & Baliunas (1986) test, the peaks at 0.202 and 0.320 mHz were found to have $FAP > 0.01$, while in the Fisher randomisation test, the former peak was found significant ($p < 0.01$) and the latter was detected with poor confidence ($p = 0.20$). The FAPs of 0.440 and 0.500 mHz are both < 0.01 in the Horne & Baliunas test and estimated at $p = 0.018$ and $p = 0.025$ in randomisation test respectively. (see Fig.6.3 and Table.6.1)

Similar analysis was performed to the 17 GHz radio intensity data obtained with NoRH, which is ground-based and free of the orbital effects. The available time series was 1998-07-03 02:55 - 06:30 UT. The power spectrum indicates the existence of long-period oscillations (Fig. 6.1(g)). We found spectral peaks in 0.220, 0.314, 0.467 and 0.582 mHz with very good confidence ($p < 0.01$) in both Horne & Baliunas (1986) and Fisher randomisation tests (see Fig.6.4 and Table.6.1).
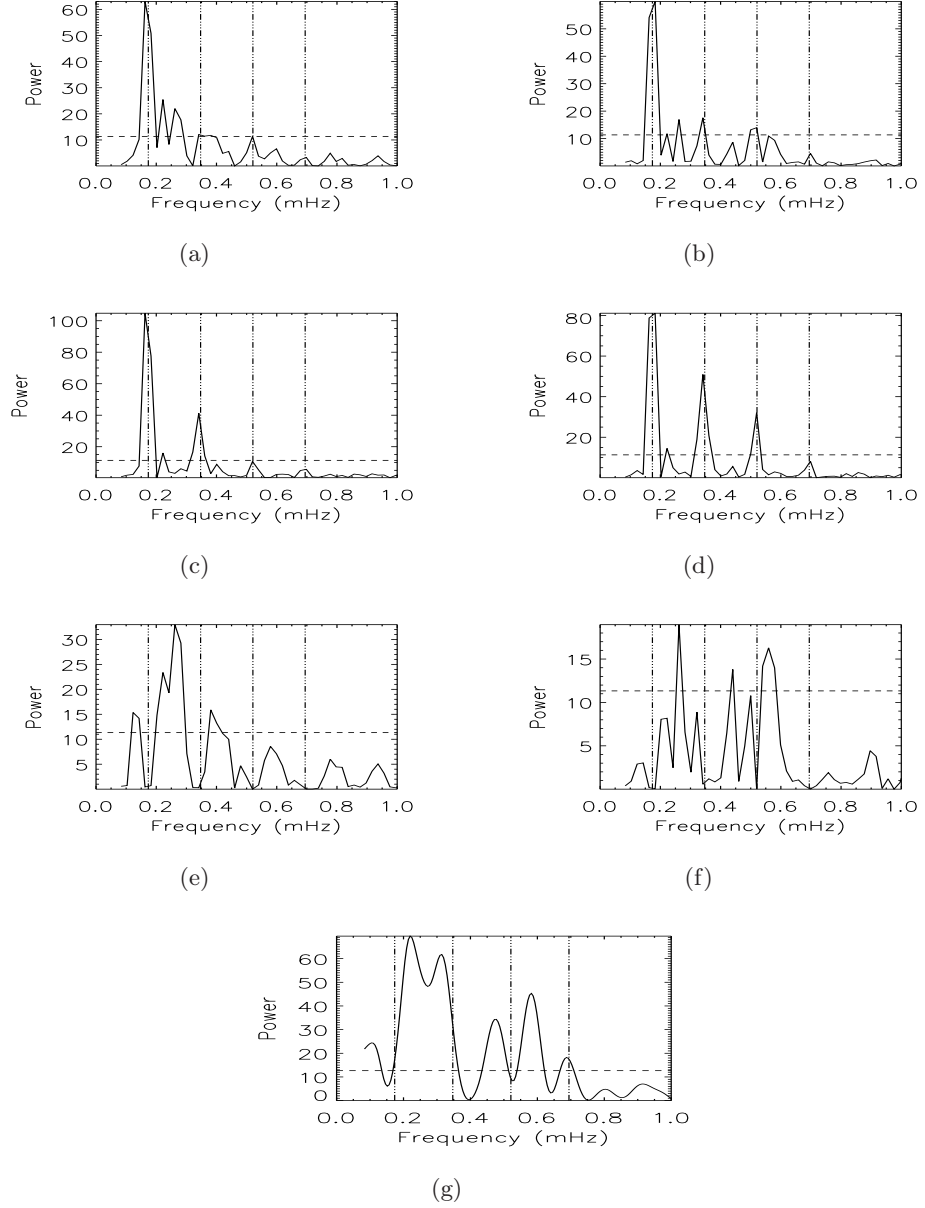
Figure 6.1: (a) and (b) Power spectra of the time series (1998-07-03 00:47 - 09:00 UT) of a macro-pixel (3×3 pixels) situated along the mid-way of the slit (Fig.2.1(b) in EUV 171 Å (left) and 195 Å (right). (c) and (d) The corresponding spectra of an enlarged macro-pixel(20×20 pixels). (e) and (f) The power spectra after filtering out the orbital frequencies. (g) The power spectrum of NoRH 17 GHz radio emission, (1998-07-03 02:55 - 06:30 UT). The vertical dot-dot-dashed lines are the orbital frequency and its higher harmonics. A horizontal dashed line indicates the 99% confidence level in all the panels (see Subsection 6.3). The detected peaks in all the bandpasses are summarised in Table 6.1

126
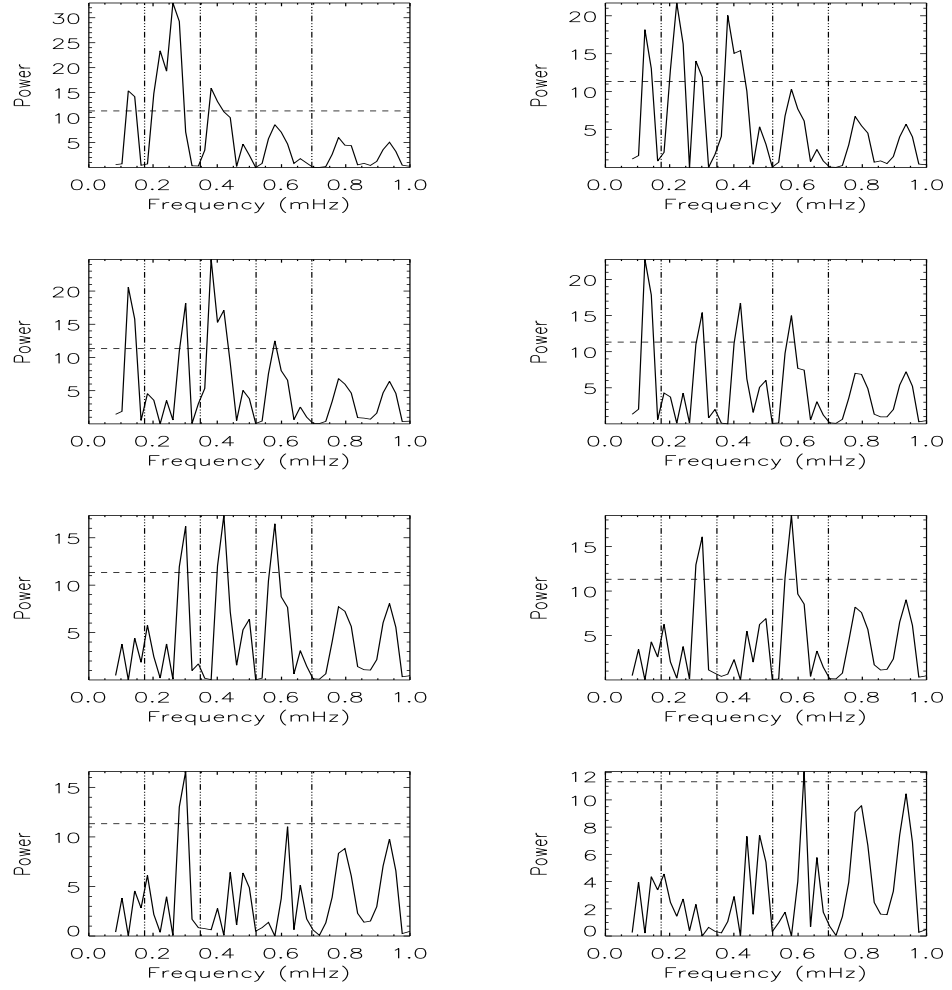
Figure 6.2: Lomb-Scargle periodograms of 171 Å data shown after iteratively subtracting the highest peak in the spectrum with power above 1% of FAP (dashed line). The iteration is displayed in order from left to right, top to bottom.
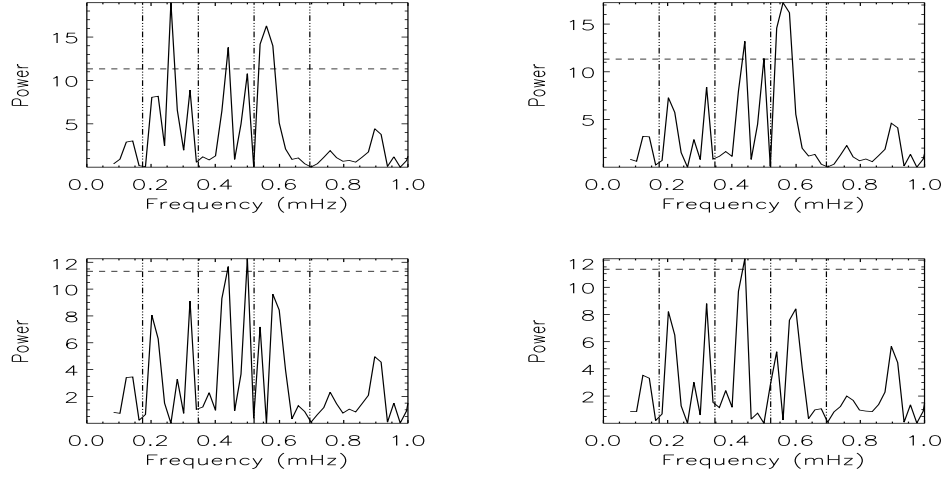
Figure 6.3: The same analysis to 195 Å data as in Fig.6.2. The iteration stops earlier than those for 171 Å data, but we note peaks with power below 99% confidence level, near 0.202 and 0.320 mHz, that may be of relevance.
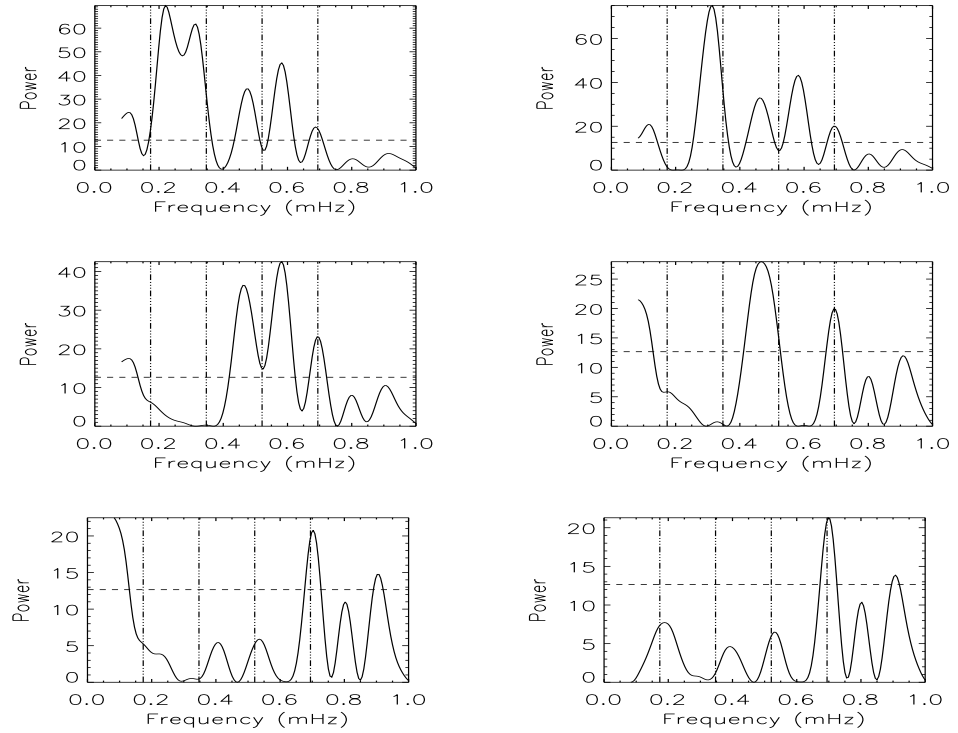
Figure 6.4: The same analysis to NoRH 17 GHz data as in Fig.6.2

Table 6.1: Summary of the detected peaks and significance

Bandpass		0.17 $\sim$ 0.35 mHz			0.35 $\sim$ 0.52 mHz		0.52 $\sim$ 0.69 mHz
TRACE 171Å	f (mHz)	0.222 ± 0.008	0.262 ± 0.008	0.302 ± 0.008	0.382 ± 0.008	0.421 ± 0.008	0.579 ± 0.008
	P (min)	75 ± 2.7	64 ± 1.9	55 ± 1.4	44 ± 0.9	39 ± 0.8	29 ± 0.4
	p-value	< 0.01	< 0.01	< 0.01	< 0.01	< 0.01	< 0.01
TRACE 195Å	f (mHz)	$[0.202 \pm 0.008]$	0.262 ± 0.008	$[0.320 \pm 0.008]$	0.440 ± 0.009	0.500 ± 0.008	0.559 ± 0.009
	P (min)	$[83 \pm 3.3]$	64 ± 1.9	$[52 \pm 1.3]$	37 ± 0.8	33 ± 0.5	30 ± 0.5
	p-value	< 0.01	< 0.01	0.20	0.018	0.025	< 0.01
NoRH 17 GHz	f (mHz)	0.220 ± 0.020	$\ldots$	0.314 ± 0.019	0.467 ± 0.020	$\ldots$	0.582 ± 0.019
	P (min)	75 ± 6.9	$\ldots$	53 ± 3.2	36 ± 1.5	$\ldots$	29 ± 0.93
	p-value	< 0.01	$\ldots$	< 0.01	< 0.01	$\ldots$	< 0.01
Average frequency (mHz)		0.221 ± 0.020	$\ldots$	0.312 ± 0.020	$\ldots$	$\ldots$	0.573 ± 0.020

All listed frequencies and corresponding periods have $FAP < 0.01$ according to the Horne & Baliunas (1986) test, except for the values indicated between square brackets (found in the 195 Å time series and of potential relevance given their closeness to significant values found in other bandpasses). The p-value indicates the false alarm probability from the Fisher randomisation test.

6.5   Conclusions

In this study, we selected time sequences of a five day sample of TRACE observations over AR8253 to study the long period coronal oscillations. We noted that 0.221, 0.312, 0.573 mHz oscillations (see Table 6.1) were present both in EUV emissions in the corona and radio signal in the chromosphere, they were found with hight confidence both in the Horne & Baliunas and Fisher randomisation tests. We conclude that the 0.221, 0.312, 0.573 mHz spectral peaks are of solar origin and are present both in the chromosphere and the corona. Since the diffuse structure in the corona is the magnetic field extension of the sunspot, propagating EUV disturbance (slow magnetoacoustic wave, see introduction in Sec. 6.1) was seen persistent for days. They were found to leak from the sunspot (Shibasaki 2001; Sych et al. 2009). It strongly implies as well the connectivity of the long period oscillations in the chromosphere and corona.

The nature of the long-period oscillations has not been understood yet. It can have several interpretations. For example, the 0.312 mHz oscillation was also well detected in 17 GHz radio emission in sunspot oscillations (Chorley et al. 2010, 2011). The 0.221 mHz oscillations are very close to the $l = 2, n = -3$ or $l = 3, n = -5$ g-mode (note: the same $2l + s$ combinations pronounce the same frequency, see Turck-Chièze et al. 2004), while the 0.583mHz could be associated with the $l = 1$ g-mode (see García et al. 2007). The slight discrepancy can be attributed to observational uncertainties, unresolved multiplet splitting at azimuthal order m due to solar interior rotation or other dynamical processes. In this case, one can speculate that the energy of g-modes, which cannot reach the solar surface, can be channelled by the magnetic field from the deeper layers of the solar interior, especially the less efficiently trapped low-l modes, and hence be seen in the regions of the magnetic concentrations such as the sunspots. The variations of the parameters of the plasma surrounding a magnetic flux tube in the convection zone by a g-mode could excite trapped MHD waves propagating along the tube to the solar surface. Thus, the magnetic flux tubes forming the sunspot could act as a waveguide with little attenuation of the g-mode signal. However, rigorous analysis of this mechanism remains to be performed. Another possibility is the global oscillations of the sunspot, proposed in terms of the shallow sunspot model (Solov'ev & Kirichek 2008).

Another puzzle is the presence of long-period oscillations in the corona, found in this study. Waves with the periods much longer than the acoustic cut-off period (normally 200-300 s in the chromospheric plasma) (Bel & Leroy 1977) are believed to be stopped at the chromosphere. One possibility is that the wave is indeed evanescent

above the chromosphere, but its penetration depth is sufficiently large to be detected in the corona. Another option could be some kind of wave-guiding by the magnetic field, while its nature needs to be revealed. However, it could not be ruled out that the detected long-period oscillations in the chromosphere and in the corona have the same period by pure coincidence.

In any case, the detection of long-period oscillations in the lower corona is a promising signal to help the understanding of the magnetic connectivity of the different layers of the Sun and beyond.

Chapter 7

Summary and discussion

In this thesis, I have engaged in detailed observational studies of compressive MHD waves in various plasma structures in the solar atmosphere and explore their diagnostic potential.

Chapter 1 is divided into three introductory sections. In Sec. 1.1, I introduced the structure and activity of the Sun, the solar emission and instrumentation. The basic physics of MHD wave theory in various structured media was detailed in Sec. 1.2. I also summarised in Sec. 1.3 the methods of time series analysis used throughout this work.

In Chapter 2, I addressed the instrumental artifacts and noise analysis confronted during this study. These results were based on the contents published in Yuan et al. (2011) (Sec. 2.1), Yuan & Nakariakov (2012) (Sec. 2.3) and un-published notes (Sec. 2.2).

By taking the spatially-averaged intensity of an active region and a rather quiet region in a TRACE EUV image cube, the power spectra show a set of harmonic frequenies (96 min, 48 min, 32 min and 24 min). This was found as the non-linear harmonics of the CCD temperature variation, which follows the TRACE orbital period (96 min, Yuan et al. 2011). The orbital periodicity and its harmonics have to be removed from the light curve obtained in the image cubes, then further analysis of other long-period oscillations can be done without wrong interpretation.

In analysing AIA images, I found that discretely cropping the AIA images introduces an artificial periodicity (about several min) into the light curves, especially in the regions with high intensity contrast (see Sec. 2.2). This periodicity is not a constant, but varies with the solar latitude due to the solar differential rotation and the longitude projection. It is very close to the 5-min p-mode signal, it may be mistakenly interpreted as a physical signal (for example by Shen & Liu 2012).

I performed noise analysis to the AIA image flux, and formulated the components that contribute significantly to the image flux noise (Yuan & Nakariakov 2012). It was found that, for the image flux lower than about 100 DN, the significant noise arise from the image pre-processings. While for those between about 100 DN and 10000 DN, the photon noise is the main part in the flux noise. The despike noise may become significant during flares or CMEs.

Chapter 3 presented the study on sunspot waves and oscillations. This chapter comprises an introductory Sec. 3.1, Sec. 3.2 and Sec. 3.3 based on Yuan et al. (2013a) and Yuan et al. (2012), respectively.

Sec. 3.2 discussed the detection of high-order azimuthal MHD body modes in sunspot (Yuan et al. 2013a). The 5–min oscillation was found to form a ring structure enclosing the sunspot umbra (see e.g. Yuan et al. 2012). I designed 5–min mask by locating the pixels within which the dominant oscillating period ranges from 4.5 to 5.5. This is performed for sunspot AR 11131 with AIA data in the 1700 Å, 1600 Å and 304 Å bandpasses. Within the 5–min mask I obtained the power maps (Sych & Nakariakov 2008; Yuan et al. 2012), correlation maps and phase maps in 5–min band. Within the mask, the 5–min oscillation exhibit nodal structures in the azimuthal direction, which can be described by $\cos m\theta$, where m is the mode number, θ is the polar angle with the origin coincident with the sunspot centre.

The phase and cross-correlation coefficient distributions of 5–min oscillation in sunspot AR 11131 (08 Dec 2010) along the azimuthal direction were studied with non-linear fitting and periodogram (Yuan et al. 2013a). Mode numbers with $m = 2, 3$ were obtained in the oscilation phase distribution observed in the 1700 Å, 1600Å data, while only $m = 3$ was detected in the correlation distribution in both bandpasses. An extra mode $m = 5$ was found to be significant in the 1600 Å data. In the 304 Å data, higher modes were detected at $m = 7, 8$ in the phase and correlation distribution, respectively. Non-linear fit to azimuthal phase and correlation distributions in 1700 Å gave $m = 3.17 \pm 0.06$ and 6.76 ± 0.63, respectively, the doubling in mode number is intrinsic in the methods, given the good quality of nodal pattern in this channel. The non-linear fits in other channels normally reproduced the most prominent peaks in the spectra, $m = 5.06 \pm 0.06/5.84 \pm 0.06$ and $3.30 \pm 0.39/7.05 \pm 0.57$ were obtained in the phase and correlation distribution of 1600 Å/ 304 Å, respectively.

Multiple modes in the sunspot lower atmosphere were detected in the phase and correlation distribution of the 5–min oscillation in sunspot AR 11330 with SDO/AIA data. One possible explanation is the modulation on the phase speed of 5-minute oscillation by slow body mode with $m > 1$ in sunspot (Zhugzhda et al.

2000).

Sec. 3.3 focused on the multi-level observation of the magnetoacoustic cut-off frequency and its diagnostic capabilities (Yuan et al. 2012). I used the Pixelised Wavelet Filtering (PWF) method (Sych & Nakariakov 2008) to compute narrow-band power maps of SDO/AIA imaging datasets in the 1700 Å, 1600 Å and 304 Å bandpasses that correspond to different heights. The cut-off frequency was defined as contours where the spectral power dropped to the median level. It was measured as a function of the spatial location. I inferred the magnetic field inclination according to the magnetoacoustic-gravity wave theory in the low-β limit (Bel & Leroy 1977) and compared it with the potential field extrapolation. I analysed intensity oscillations in a symmetric sunspot AR 11131 (08 Dec 2010) and an asymmetric sunspot AR 11330 (27 Oct 2011). I reconstructed the magnetic field inclination in the radial direction for the symmetric sunspot and in both radial and azimuthal directions for the asymmetric sunspot. I observed 3D variation of the main oscillation periods in sunspots. It was found that low-period oscillations were mostly constrained in the sunspot umbra, while longer-period oscillations formed an annular shape enclosing the sunspot umbra. Longer periods are found to be distributed further away from the sunspot centre. Our results indicate that the 3–min oscillation are generated in the chromosphere, possibly by the acoustic resonator model, while 5–min and longer-period oscillations seemed to originate in a level under the photosphere. The reconstructed field inclinations are normally larger than the value obtained by the potential field extrapolation, the inclined magnetic field line can account only for about 60-80% of cut-off frequency lowering.

Chapter 4 was based on Yuan & Nakariakov (2012), the characteristics of propagating EUV disturbances were discussed. The methods are proposed to measure the phase speed and validated with parametric studies. To measure the apparent phase speed of the propagating disturbances, I designed the cross-fitting technique (CFT), 2D coupled fitting (DCF) and best similarity measure (BSM). The CFT, DCF and BSM methods are found to be reliable techniques to measure the apparent (projected) phase speed (Yuan & Nakariakov 2012). The samples of larger effective spatial length are more suitable for these methods. Time-distance plots with background removal and normalisation allow for more robust measurements, with little effect of the choice of the detrending time. The cross-fitting technique provides reliable measurements on good samples (e.g. samples with large effective detection length and recurring features). 2D coupled-fitting is found to be sensitive to the initial guess for parameters of the 2D fitting function. Thus DCF is only optimised in measuring one of the parameters (the phase speed in our application),

while the period is poorly measured. The best similarity measure is robust for all types of samples and very tolerant to image pre-processing and regularisation (Yuan & Nakariakov 2012).

Chapter 5 was based on Yuan et al. (2013b). I aim to probe the link between the propagating fast wave trains and quasi-periodic pulsations in flaring energy releases. By measuring the wave parameters, I investigate the potential of propagating fast wave trains in the diagnostics of their energy source and wave guides. The wave amplitude and propagating speed are measured to probe the characteristics of its energy source and coronal condition. The correlation of fast wave trains with flare-generated radio bursts is investigated. The wavelet spectrum of the difference intensity variation shows a typical tadpole structure. It implies that the fast magneto-acoustic waves were generated impulsively. The correlation of the fast wave trains with radio bursts indicates that during the flare several energy pulses were released. The wave amplitude reaches maximum in the midway of its course. This can be the combined effect of wave energy diffusing across the coronal loops and density stratification. The cross-sectional amplitude distribution perpendicular to the wave vector follows well a Gaussian profile. This feature is more close to a kink mode. The propagating speed displays significant deceleration, from $\sim735 - 845\,\mathrm{km/s}$ to $\sim600\,\mathrm{km/s}$. This can be caused by the decrease of the Alfvén speed and/or projection effect.

Chapter 6 is adapted from Yuan et al. (2011). I discussed the connectivity of different levels of the solar atmosphere. Long-period oscillations in a coronal diffuse structure are detected with the Transition Region And Coronal Explorer (TRACE). The EUV images of the NOAA active region 8253 are available in 171 Å and 195 Å bandpasses from 30 June to 4 July 1998. After the exclusion of the orbital effects, I identified several long-period oscillations in the diffuse fan-like structure of the active region. Similar periodicities were detected in the radio emission from the chromospheric part of that active region, observed with the ground-based Nobeyama Radioheliograph (NoRH) in the 17 GHz channel. It was found that 0.221, 0.312 and 0.573 mHz oscillations were present in both EUV emission lines in the corona and the radio signal from the sunspot in the chromosphere, just beneath the active region. From the frequency values, the 0.221 and 0.573 mHz oscillations could be associated with the $l = 2, n = -3$ or $l = 3, n = -5$ and $l = 1$ gravity-driven solar interior modes, respectively. The appearance of these oscillations in the coronal part of the active region can be connected with the wave leakage or the evanescence of chromospheric oscillations.

In this work, I advanced our understanding of the compressive MHD waves

in the solar atmosphere.This study can be developed in a number of ways. Joint observations with both imagers and spectrometers would solidly identify the MHD wave modes. Another direction of fine observation is ground-based telescopes, which can provide simultaneously density, velocity and magnetic field maps in much better temporal and spatial resolution. The phase relations between these quantities and multi-level observation would significantly facilitate the understanding of wave modes and energy transportation.

Another stage to extend the current work is to observe the wave modes in other structures in the solar atmosphere. The successful detection of MHD waves in large sunspots (cf. Yuan et al. 2012) demonstrated the potential to diagnose the magnetic field inclinations at different height of the sunspot atmosphere. Other structures also exhibit wave motions, e.g. magnetic pore, spicules, surges, prominences, the MHD seismology can be expand significantly in these plasma structures.

Notably the compressive MHD waves are only a part of the MHD dispersion diagram. Other wave modes, e.g. Alfvén waves and weakly compressive kink wave, also retains a wealth of information for MHD seismology and coronal heating. The study of these wave modes would be a hot topic with the launch of next-generation missions, e.g. Solar-C, Solar Orbiter.

In summary, the following study will be stretched in three main directions: a) new instruments with better temporal and spatial resolution, joint observations with both imagers and spectrometers. b) MHD wave detections in other plasma structures of the solar atmosphere. c) use of other wave modes.

Bibliography

Abdelatif, T. E., Lites, B. W., & Thomas, J. H. 1986, ApJ, 311, 1015

Appourchaux, T., Belkacem, K., Broomhall, A. M., et al. 2010, A&A Rev., 18, 197

Asai, A., Shimojo, M., Isobe, H., et al. 2001, ApJ, 562, L103

Aschwanden, M. J. 2005, Physics of the Solar Corona. An Introduction with Problems and Solutions (2nd edition)

Aschwanden, M. J. & Boerner, P. 2011, ApJ, 732, 81

Aschwanden, M. J., Fletcher, L., Schrijver, C. J., & Alexander, D. 1999, ApJ, 520, 880

Aschwanden, M. J., Nightingale, R. W., Tarbell, T. D., & Wolfson, C. J. 2000, ApJ, 535, 1027

Banerjee, D., Gupta, G. R., & Teriaca, L. 2011, Space Sci. Rev., 158, 267

Bastian, T. S., Benz, A. O., & Gary, D. E. 1998, ARA&A, 36, 131

Bel, N. & Leroy, B. 1977, A&A, 55, 239

Bel, N. & Mein, P. 1971, A&A, 11, 234

Benz, A. O. 2008, Living Reviews in Solar Physics, 5

Berghmans, D. & Clette, F. 1999, Sol. Phys., 186, 207

Bloomfield, D. S., Lagg, A., & Solanki, S. K. 2007, ApJ, 671, 1005

Boerner, P. 2011, Private communication

Boerner, P., Edwards, C., Lemen, J., et al. 2012, Sol. Phys., 275, 41

Bogdan, T. J. 2000, Sol. Phys., 192, 373

Bogdan, T. J. & Judge, P. G. 2006, Royal Society of London Philosophical Transactions Series A, 364, 313

Borrero, J. M. & Ichimoto, K. 2011, Living Reviews in Solar Physics, 8

Botha, G. J. J., Arber, T. D., Nakariakov, V. M., & Zhugzhda, Y. D. 2011, ApJ, 728, 84

Broomhall, A.-M., Chaplin, W. J., Elsworth, Y., Fletcher, S. T., & New, R. 2009, ApJ, 700, L162

Broomhall, A.-M., Chaplin, W. J., Elsworth, Y., & Simoniello, R. 2012, MNRAS, 420, 1405

Cally, P. S. 2005, MNRAS, 358, 353

Cally, P. S. & Bogdan, T. J. 1997, ApJ, 486, L67

Cally, P. S., Crouch, A. D., & Braun, D. C. 2003, MNRAS, 346, 381

Centeno, R., Collados, M., & Trujillo Bueno, J. 2006, ApJ, 640, 1153

Centeno, R., Collados, M., & Trujillo Bueno, J. 2009, ApJ, 692, 1211

Chatfield, C. 2003, The Analysis of Time Series: An Introduction, Sixth Edition, Texts in Statistical Science (Taylor & Francis)

Chen, P. F. 2011, Living Reviews in Solar Physics, 8

Chorley, N., Foullon, C., Hnat, B., Nakariakov, V. M., & Shibasaki, K. 2011, A&A, 529, A123

Chorley, N., Hnat, B., Nakariakov, V. M., Inglis, A. R., & Bakunina, I. A. 2010, A&A, 513, A27+

Cooper, F. C., Nakariakov, V. M., & Tsiklauri, D. 2003a, A&A, 397, 765

Cooper, F. C., Nakariakov, V. M., & Williams, D. R. 2003b, A&A, 409, 325

Daubechies, I. 1990, IEEE Transactions on Information Theory, 36, 961

De Moortel, I. 2006, Royal Society of London Philosophical Transactions Series A, 364, 461

De Moortel, I. 2009, Space Science Reviews, 149, 65

De Moortel, I. & Hood, A. W. 2000, A&A, 363, 269

De Moortel, I. & Hood, A. W. 2003, A&A, 408, 755

De Moortel, I., Hood, A. W., Ireland, J., & Walsh, R. W. 2002a, Sol. Phys., 209, 89

De Moortel, I., Ireland, J., Hood, A. W., & Walsh, R. W. 2002b, A&A, 387, L13

De Moortel, I., Ireland, J., & Walsh, R. W. 2000, A&A, 355, L23

De Moortel, I., Ireland, J., Walsh, R. W., & Hood, A. W. 2002c, Sol. Phys., 209, 61

De Moortel, I. & Nakariakov, V. M. 2012, Royal Society of London Philosophical Transactions Series A, 370, 3193

De Pontieu, B., Erdélyi, R., & De Moortel, I. 2005, ApJ, 624, L61

De Pontieu, B., Erdélyi, R., & James, S. P. 2004, Nature, 430, 536

De Pontieu, B. & McIntosh, S. W. 2010, ApJ, 722, 1013

de Wijn, A. G., McIntosh, S. W., & De Pontieu, B. 2009, ApJ, 702, L168

Deforest, C. E. & Gurman, J. B. 1998, ApJ, 501, L217+

Del Zanna, G. 2008, A&A, 481, L49

Dere, K. P., Landi, E., Mason, H. E., Monsignori Fossi, B. C., & Young, P. R. 1997, A&AS, 125, 149

Dhillon, V. S., Privett, G. J., & Duffey, K. P. 2001, PERIOD, A Time-Series Analysis Package Version 5.0 User's Manual

Doschek, G. A., Mariska, J. T., Warren, H. P., et al. 2007, ApJ, 667, L109

Doschek, G. A., Warren, H. P., Mariska, J. T., et al. 2008, ApJ, 686, 1362

Edwin, P. M. & Roberts, B. 1982, Sol. Phys., 76, 239

Edwin, P. M. & Roberts, B. 1983a, Sol. Phys., 88, 179

Edwin, P. M. & Roberts, B. 1983b, Sol. Phys., 88, 179

Efremov, V. I., Parfinenko, L. D., & Soloviev, A. A. 2009, Cosmic Research, 47, 279

Farge, M. 1992, Annual Review of Fluid Mechanics, 24, 395

Felipe, T., Khomenko, E., Collados, M., & Beck, C. 2010, ApJ, 722, 131

Ferraz-Mello, S. 1981, AJ, 86, 619

Fisher, R. A., Genetiker, S., Fisher, R. A., et al. 1970, Statistical methods for research workers, Vol. 14 (Oliver and Boyd Edinburgh)

Fla, T., Skumanich, A., & Osherovich, V. A. 1982, ApJ, 261, 700

Fontenla, J. M., Avrett, E. H., & Loeser, R. 1993, ApJ, 406, 319

Forbes, T. G. 2000, J. Geophys. Res., 105, 23153

Foster, G. 1995, AJ, 109, 1889

Foullon, C., Verwichte, E., & Nakariakov, V. M. 2004, A&A, 427, L5

Foullon, C., Verwichte, E., & Nakariakov, V. M. 2009, ApJ, 700, 1658

García, R. A., Turck-Chièze, S., Jiménez-Reyes, S. J., et al. 2007, Science, 316, 1591

Gelfreikh, G. B., Nagovitsyn, Y. A., & Nagovitsyna, E. Y. 2006, PASJ, 58, 29

Gilman, D. L., Fuglister, F. J., & Mitchell, J. M. 1963, J. Atmos. Sci., 20, 182

Gopalswamy, N., Mikić, Z., Maia, D., et al. 2006, Space Sci. Rev., 123, 303

Gordovskyy, M. & Jain, R. 2008, ApJ, 681, 664

Gounder, M. K., Shitan, M., & Imon, R. A. 2007, in Festschrift in honor of Distinguished Professor Mir Masoom Ali On the occasion of his retirement, 213–224

Gruszecki, M., Nakariakov, V. M., & Van Doorsselaere, T. 2012, A&A, 543, A12

Gupta, G. R., Banerjee, D., Teriaca, L., Imada, S., & Solanki, S. 2010, ApJ, 718, 11

Handy, B. N., Acton, L. W., Kankelborg, C. C., et al. 1999, Sol. Phys., 187, 229

Hannah, I. G. & Kontar, E. P. 2012, A&A, 539, A146

Hara, H., Watanabe, T., Harra, L. K., et al. 2008, ApJ, 678, L67

Harra, L. K., Sakao, T., Mandrini, C. H., et al. 2008, ApJ, 676, L147

Harris, F. 1978, Proceedings of the IEEE, 66, 51

Hathaway, D. H. 2010, Living Reviews in Solar Physics, 7

Hernandez, G. 1999, J. Geophys. Res., 104, 10355

Hershaw, J., Foullon, C., Nakariakov, V. M., & Verwichte, E. 2011, A&A, 531, A53

Horne, J. H. & Baliunas, S. L. 1986, ApJ, 302, 757

Howard, R. F., Harvey, J. W., & Forgach, S. 1990, Sol. Phys., 130, 295

Hurlburt, N., Cheung, M., Schrijver, C., et al. 2012, Sol. Phys., 275, 67

Inglis, A. R. & Nakariakov, V. M. 2009, A&A, 493, 259

Jefferies, S. M., McIntosh, S. W., Armstrong, J. D., et al. 2006, ApJ, 648, L151

Jenkins, G. & Watts, D. 1969, Spectral analysis and its applications, Holden-Day series in time series analysis (Holden-Day)

Jess, D. B., De Moortel, I., Mathioudakis, M., et al. 2012, ApJ, 757, 160

Kepko, L. & Spence, H. E. 2003, Journal of Geophysical Research (Space Physics), 108, 1257

Khomenko, E. 2009, in Astronomical Society of the Pacific Conference Series, Vol. 416, Solar-Stellar Dynamos as Revealed by Helio- and Asteroseismology: GONG 2008/SOHO 21, ed. M. Dikpati, T. Arentoft, I. González Hernández, C. Lindsey, & F. Hill, 31

Khomenko, E. & Collados, M. 2006, ApJ, 653, 739

Kiddie, G., De Moortel, I., Del Zanna, G., McIntosh, S. W., & Whittaker, I. 2012, Sol. Phys., 279, 427

King, D. B., Nakariakov, V. M., Deluca, E. E., Golub, L., & McClements, K. G. 2003, A&A, 404, L1

Klimchuk, J. A., Tanner, S. E. M., & De Moortel, I. 2004, ApJ, 616, 1232

Kobanov, N. I., Kolobov, D. Y., Chupin, S. A., & Nakariakov, V. M. 2011, A&A, 525, A41

Krishna Prasad, S., Banerjee, D., & Gupta, G. R. 2011, A&A, 528, L4

Lemen, J. R., Title, A. M., Akin, D. J., et al. 2012, Sol. Phys., 275, 17

Linnell Nemec, A. F. & Nemec, J. M. 1985a, AJ, 90, 2317

Linnell Nemec, A. F. & Nemec, J. M. 1985b, AJ, 90, 2317

Lites, B. W., Dunn, R. B., Elmore, D. F., et al. 1992, in Bulletin of the American Astronomical Society, Vol. 24, American Astronomical Society Meeting Abstracts #180, 747

Liu, W., Ofman, L., Nitta, N. V., et al. 2012, ApJ, 753, 52

Liu, W., Title, A. M., Zhao, J., et al. 2011, ApJ, 736, L13

Loughhead, R. E. & Bray, R. J. 1958, Australian Journal of Physics, 11, 177

Mariska, J. T. & Muglach, K. 2010, ApJ, 713, 573

Markwardt, C. B. 2009, in Astronomical Society of the Pacific Conference Series, Vol. 411, Astronomical Society of the Pacific Conference Series, ed. D. A. Bohlender, D. Durand, & P. Dowler, 251–+

Marsch, E. 2006, Living Reviews in Solar Physics, 3

Marsh, M. S., Walsh, R. W., De Moortel, I., & Ireland, J. 2003, A&A, 404, L37

Marsh, M. S., Walsh, R. W., & Plunkett, S. 2009, ApJ, 697, 1674

Martens, P. C. H., Attrill, G. D. R., Davey, A. R., et al. 2012, Sol. Phys., 275, 79

Martínez-Sykora, J., De Pontieu, B., Hansteen, V., & McIntosh, S. W. 2011, ApJ, 732, 84

McComas, D. J., Elliott, H. A., Schwadron, N. A., et al. 2003, Geophys. Res. Lett., 30, 100000

McIntosh, S. W., de Pontieu, B., & Tomczyk, S. 2008, Sol. Phys., 252, 321

McIntosh, S. W. & Jefferies, S. M. 2006, ApJ, 647, L77

Melnikov, V. F., Reznikova, V. E., Shibasaki, K., & Nakariakov, V. M. 2005, A&A, 439, 727

Mészárosová, H., Karlický, M., Rybák, J., & Jiřička, K. 2009a, A&A, 502, L13

Mészárosová, H., Karlický, M., Rybák, J., & Jiřička, K. 2009b, ApJ, 697, L108

Metcalf, T. R., Leka, K. D., Barnes, G., et al. 2006, Sol. Phys., 237, 267

Mierla, M., Inhester, B., Antunes, A., et al. 2010, Ann. Geophys., 28, 203

Murawski, K. & Roberts, B. 1994, Sol. Phys., 151, 305

Nagashima, K., Sekii, T., Kosovichev, A. G., et al. 2007, PASJ, 59, 631

Nagovitsyna, E. Y. & Nagovitsyn, Y. A. 2001, Astronomy Letters, 27, 118

Nagovitsyna, E. Y. & Nagovitsyn, Y. A. 2002, Astronomy Letters, 28, 121

Nakajima, H., Nishio, M., Enome, S., et al. 1994, IEEE Proceedings, 82, 705

Nakariakov, V. M. 2006, Royal Society of London Philosophical Transactions Series
    A, 364, 473

Nakariakov, V. M., Arber, T. D., Ault, C. E., et al. 2004, MNRAS, 349, 705

Nakariakov, V. M. & Melnikov, V. F. 2009, Space Sci. Rev., 149, 119

Nakariakov, V. M., Melnikov, V. F., & Reznikova, V. E. 2003, A&A, 412, L7

Nakariakov, V. M. & Ofman, L. 2001, A&A, 372, L53

Nakariakov, V. M., Ofman, L., Deluca, E. E., Roberts, B., & Davila, J. M. 1999,
    Science, 285, 862

Nakariakov, V. M., Pascoe, D. J., & Arber, T. D. 2005, Space Sci. Rev., 121, 115

Nakariakov, V. M. & Verwichte, E. 2005, Living Reviews in Solar Physics, 2, 3

Nakariakov, V. M., Verwichte, E., Berghmans, D., & Robbrecht, E. 2000, A&A, 362,
    1151

Nindos, A., Alissandrakis, C. E., Gelfreikh, G. B., Bogod, V. M., & Gontikakis, C.
    2002, A&A, 386, 658

Nuttall, A. 1981, Acoustics, Speech and Signal Processing, IEEE Transactions on,
    29, 84

Ofman, L. 2010, Living Reviews in Solar Physics, 7

Ofman, L., Liu, W., Title, A., & Aschwanden, M. 2011, ApJ, 740, L33

Ofman, L., Nakariakov, V. M., & Deforest, C. E. 1999, ApJ, 514, 441

Ofman, L., Nakariakov, V. M., & Sehgal, N. 2000a, ApJ, 533, 1071

Ofman, L., Romoli, M., Poletto, G., Noci, G., & Kohl, J. L. 2000b, ApJ, 529, 592

Ofman, L. & Wang, T. 2002, ApJ, 580, L85

O'Shea, E., Banerjee, D., Doyle, J. G., Fleck, B., & Murtagh, F. 2001, A&A, 368, 1095

Osherovich, V. A. 1982, Sol. Phys., 77, 63

Pesnell, W. D., Thompson, B. J., & Chamberlin, P. C. 2012, Sol. Phys., 275, 3

Rempel, M., Schüssler, M., Cameron, R. H., & Knölker, M. 2009, Science, 325, 171

Reznikova, V. E. & Shibasaki, K. 2012, ApJ, 756, 35

Reznikova, V. E., Shibasaki, K., Sych, R. A., & Nakariakov, V. M. 2012, ApJ, 746, 119

Rice, R. & Plaunt, J. 1971, Communication Technology, IEEE Transactions on, 19, 889

Robbrecht, E., Verwichte, E., Berghmans, D., et al. 2001, A&A, 370, 591

Roberts, B. 1981a, Sol. Phys., 69, 39

Roberts, B. 1981b, Sol. Phys., 69, 27

Roberts, B., Edwin, P. M., & Benz, A. O. 1984, ApJ, 279, 857

Roberts, B. & Webb, A. R. 1978, Sol. Phys., 56, 5

Sakao, T., Kano, R., Narukage, N., et al. 2007, Science, 318, 1585

Sakurai, T. 1982, Sol. Phys., 76, 301

Sakurai, T., Goossens, M., & Hollweg, J. V. 1991, Sol. Phys., 133, 227

Scargle, J. D. 1982, ApJ, 263, 835

Scherrer, P. H., Bogart, R. S., Bush, R. I., et al. 1995, Sol. Phys., 162, 129

Schou, J., Scherrer, P. H., Bush, R. I., et al. 2012, Sol. Phys., 275, 229

Schunker, H. & Cally, P. S. 2006, MNRAS, 372, 551

Schwabe, H. 1844, Astron. Nachr., 21, 233

Shen, Y. & Liu, Y. 2012, ApJ, 753, 53

Shibasaki, K. 2001, ApJ, 550, 1113

Shibata, K. & Magara, T. 2011, Living Reviews in Solar Physics, 8

Solanki, S. K. 2003, A&A Rev., 11, 153

Solov'ev, A. A. & Kirichek, E. A. 2008, Astrophysical Bulletin, 63, 169

Staude, J. 2002, Astronomische Nachrichten, 323, 317

Stepanov, A. V., Zaitsev, V. V., & Nakariakov, V. M. 2012, Physics Uspekhi, 55, A260000

Suematsu, Y., Shibata, K., Neshikawa, T., & Kitai, R. 1982, Sol. Phys., 75, 99

Sych, R., Nakariakov, V. M., Karlicky, M., & Anfinogentov, S. 2009, A&A, 505, 791

Sych, R., Zaqarashvili, T. V., Nakariakov, V. M., et al. 2012, A&A, 539, A23

Sych, R. A. & Nakariakov, V. M. 2008, Sol. Phys., 248, 395

Sych, R. A., Nakariakov, V. M., Anfinogentov, S. A., & Ofman, L. 2010, Sol. Phys., 266, 349

Thomson, D. J., Maclennan, C. G., & Lanzerotti, L. J. 1995, Nature, 376, 139

Tian, H., McIntosh, S. W., & De Pontieu, B. 2011a, ApJ, 727, L37

Tian, H., McIntosh, S. W., De Pontieu, B., et al. 2011b, ApJ, 738, 18

Tomczyk, S., McIntosh, S. W., Keil, S. L., et al. 2007, Science, 317, 1192

Torrence, C. & Compo, G. P. 1998, Bulletin of the American Meteorological Society, 79, 61

Tripathi, D., Isobe, H., & Jain, R. 2009, Space Sci. Rev., 149, 283

Tsiklauri, D. & Nakariakov, V. M. 2001, A&A, 379, 1106

Turck-Chièze, S., García, R. A., Couvidat, S., et al. 2004, ApJ, 604, 455

Tziotziou, K., Tsiropoula, G., Mein, N., & Mein, P. 2006, A&A, 456, 689

Van Doorsselaere, T., Nakariakov, V. M., & Verwichte, E. 2008, ApJ, 676, L73

Verwichte, E., Marsh, M., Foullon, C., et al. 2010, ApJ, 724, L194

Verwichte, E., Nakariakov, V. M., & Cooper, F. C. 2005, A&A, 430, L65

Vourlidas, A., Buzasi, D., Howard, R., & Esfandiari, E. 2002, in ESA Conference Proceedings, Vol. SP-506, Solar Variability: From Core to Outer Frontiers, ed. A. Wilson (Noordwijk: ESA), 91–94

145

Wang, T. J., Ofman, L., & Davila, J. M. 2009a, ApJ, 696, 1448

Wang, T. J., Ofman, L., Davila, J. M., & Mariska, J. T. 2009b, A&A, 503, L25

Wang, T. J., Ofman, L., Davila, J. M., & Mariska, J. T. 2009c, A&A, 503, L25

Wang, T. J., Solanki, S. K., Innes, D. E., Curdt, W., & Marsch, E. 2003, A&A, 402, L17

Webb, D. F. & Howard, T. A. 2012, Living Reviews in Solar Physics, 9

White, R. S., Verwichte, E., & Foullon, C. 2012, A&A, 545, A129

Williams, D. R., Mathioudakis, M., Gallagher, P. T., et al. 2002, MNRAS, 336, 747

Williams, M. J., Bureau, M., & Cappellari, M. 2010, MNRAS, 409, 1330

Wöhl, H., Brajša, R., Hanslmeier, A., & Gissot, S. F. 2010, A&A, 520, A29

Yashiro, S., Gopalswamy, N., Michalek, G., et al. 2004, J. Geophys. Res., 109

Yuan, D. & Nakariakov, V. M. 2012, A&A, 543, A9

Yuan, D., Nakariakov, V. M., Chorley, N., & Foullon, C. 2011, A&A, 533, A116

Yuan, D., Nakariakov, V. M., & Sych, R. 2013a, A&A letter (submitted)

Yuan, D., Shen, Y. D., Liu, Y., et al. 2013b, A&A letter (submitted)

Yuan, D., Sych, R., Reznikova, V. E., & Nakariakov, V. M. 2012, ArXiv e-prints

Zajtsev, V. V. & Stepanov, A. V. 1975, Issledovaniia Geomagnetizmu Aeronomii i Fizike Solntsa, 37, 3

Zhugzhda, I. D. & Dzhalilov, N. S. 1984, A&A, 132, 45

Zhugzhda, I. D., Locans, V., & Staude, J. 1983, Sol. Phys., 82, 369

Zhugzhda, Y. D. 2008, Sol. Phys., 251, 501

Zhugzhda, Y. D., Balthasar, H., & Staude, J. 2000, A&A, 355, 347